Title

Experimental investigations at high temperatures and pressures on melting and mineral solubility in systems of feldspars with water, with special reference to the origin of granite

Author

Makhluf, Adam Rafiq

Publication Date

2015

Peer reviewed|Thesis/dissertation

UNIVERSITY OF CALIFORNIA

Los Angeles

Experimental investigations at high temperatures and pressures on melting and mineral solubility in systems of feldspars with water, with special reference to the origin of granite

A dissertation submitted in partial satisfaction of the

requirements for the degree of

Doctor of Philosophy in Chemistry

by

Adam Rafiq Makhluf

2015

ABSTRACT OF THE DISSERTATION

Experimental investigations at high temperatures and pressures
on melting and mineral solubility in systems of feldspars with water,
with special reference to the origin of granite

by

Adam Rafiq Makhluf
Doctor of Philosophy in Chemistry
University of California, Los Angeles, 2015
Professor William M. Gelbart, Chair

Supercritical fluids in rock-H_2O systems have been proposed to be important agents of mass transfer in high-pressure environments such as subduction zones. For the first study, experiments were conducted on the model system $NaAlSi_3O_8$ (Ab)-H_2O to investigate phase relations at pressure (P) and temperature (T) in the vicinity of critical mixing between aqueous fluid and silicate melt. Isobaric equilibrium phase relations were determined at 1.0-1.7 GPa, 600-1060 °C, and H_2O mole fractions (x_{H_2O}) of 0.035-0.99. A subregular solution model was used to describe the solvus curves. P- and T-dependent Margules coefficients, W_{Ab} and W_{H_2O}, and activities of H_2O and Ab were formulated using compositions at the solidus and critical point at each pressure as input. The results provide a comprehensive account of the solution properties of subcritical and supercritical fluids in the Ab-H_2O system at temperatures and pressures

corresponding to the deep-crust regions of granite magma generation. This work may have considerable bearing on element transport, extractability of partial melt, and ultimate level of melt emplacement in the middle and upper crust.

The second study is an experimental determination at deep-crustal conditions of liquidus-H_2O contents of more complex granitic systems containing albite, potassium feldspar and quartz. The liquidus water content of a granitic melt at high-P and T is important because it constrains the volume of granite that could be produced by dehydration melting of the deep crust and it strongly influences physical properties that control the ability of granitic liquids to accumulate and ascend. The high liquidus-H_2O contents determined in this study present a challenge for producing voluminous amounts of metaluminous granites from lower crustal biotite-amphibole gneisses by dehydration melting. Additionally, rapid undercooling of granitic melts may lead to granophyric textures described in volcanic and impactitie surge deposits and the formation of a solid solution of coesite and feldspar.

The dissertation of Adam Rafiq Makhluf is approved.

Craig E. Manning

Daniel Neuhauser

William M. Gelbart, Committee Chair

University of California, Los Angeles

2015

Table of Contents

List of Tables

Chapter 1

Chapter 2

List of Figures

Chapter 1

Chapter 2

Acknowledgements

First and foremost, I would like to thank the generosity of the UCLA Department of Chemistry, and in particular Dr. Gelbart, who allowed me complete my studies as a joint collaboration with the Department of Earth, Planetary and Space Sciences under the direction of Dr. Craig E. Manning in the PTX Lab. Without your willingness to chair my committee and agreement of my plan to study geochemistry, none of this would be possible. You are an amazing person that UCLA is luck to have.

Craig, I want to thank you for your incredible support and encouragement over the last four years. You graciously accepted me into your lab as a young Ph.D. student that knew very little about geology or geochemistry at the time, and you took a gamble on me. You allowed me to grow and mature as a scientist in a field that combines my love for chemistry with that of the Earth. It's been an amazing time, and I look forward to continuing our work together. Thank you for your belief in me and all of the opportunities that you have provided.

To Bob Newton, where do I begin? You took me under your wing shorty after arriving in Craig's lab. In a short time, we would become partners and friends, feeding off of our endless enthusiasm for what we do. You taught me what it takes to be an experimentalist, and to selflessly dedicate oneself to our "karma". Thank you for all of your help along the way. Your boundless energy, curiosity, knowledge and kindness are an inspiration to us all.

To my dad, thank you for all the time we spent together in my early years as a student, developing a love for mathematics. This would not be possible without you. And thank you to my mom, grandma and rest of my family that supported me though this long, 31 year, journey.

To my amazing wife, Kate, thank you for being by my side these last four years and for all of your love. I couldn't have done it without you. Let the journey begin!

VITA

2008	CARE Fellow
2008	Whitcome Fellow
2008	SMART Grant
2008	Award for Outstand Achievement, UCLA
2010	B.S. Chemistry, cum laude
	Physical Chemistry emphasis
	University of California, Los Angeles
2011	M.S. Chemistry
	University of California, Los Angeles
2012	Teaching Associate, UCLA
2013	Geocheminar, invited talk
	University of California, Los Angeles
2013	Limpopo Belt Conference, invited talk
	University of Johannesburg
2013	Distinguished Teaching Assistant Award, nominee
2013	American Geophysical Union Fall Conference, poster
	San Francisco, California
2014	Teaching Fellow, UCLA
2014	American Geophysical Union Fall Conference, poster
	San Francisco, California
2015	Geocheminar, invited talk
	University of California, Los Angeles

PUBLICATIONS

Aranovich, L. Y., Makhluf, A. R., Manning, C. E., & Newton, R. C. (2014). Dehydration melting and the relationship between granites and granulites. *Precambrian Research*, ***253***, 26-37.

Bux, S. K., Rodriguez M., Yeung, M.T., Yang, C., Makhluf, A.R., Blair, R.G., Fleurial, J.P., Kaner, R.B. Rapid Solid-State Synthesis of Nanostructured Silicon. *Chemistry of Materials* **2010**, *22* (8), 2534-2540.

CHAPTER 1

Experimental investigation of phase relations in the system $NaAlSi_3O_8$-H_2O at high H_2O concentrations: liquidus relations, liquid-vapor mixing, and critical phenomena at deep crust-upper mantle conditions.

Abstract

Supercritical fluids in rock-H_2O systems have been proposed to be important agents of mass transfer in high-pressure environments such as subduction zones. New experimental studies were conducted on the model system $NaAlSi_3O_8$ (Ab)-H_2O to investigate phase relations at pressure (P) and temperature (T) in the vicinity of critical mixing between aqueous fluid and silicate melt. Isobaric equilibrium phase relations were determined at 1.0, 1.25, 1.4, 1.6 and 1.7 GPa, 600-1060 °C, and H_2O mole fractions (X_{H_2O}) of 0.035 to 0.99.

All experiments were conducted in a piston cylinder apparatus. Compositions of hydrous $NaAlSi_3O_8$ liquid (L) and H_2O-rich fluid (V) were bracketed by textural analysis of quenched run products. We determined the fluid-absent liquidus curves at each pressure by the same method. Solubility measurements on natural albite and intersections of the liquidus curves with the solidi defined the melt and fluid compositions of the isobaric three-phase assemblages. Critical temperatures of melt-fluid mixing are 1050±15 °C at 1.0 GPa, 940±20 °C at 1.25 GPa, 835±28 °C at 1.4 GPa and ≤ 700 °C at 1.6 GPa. The bulk composition at critical mixing of L and V is ~ 45 wt% H_2O at all pressures investigated. Our results indicate a stable critical end point on the hydrous melting curve of albite at 1.65 ± 0.08 GPa and 665±15 °C. Low albite is stable in

the presence of supercritical fluid at 650-675 ^{o}C and 1.7 GPa, a pressure near the breakdown of albite to jadeite plus quartz.

A subregular solution model can be used to describe the solvus curves. Pressure- and temperature-dependent Margules coefficients, W_{Ab} and W_{H_2O}, and activities of H_2O and Ab were formulated using compositions at the solidus and the critical point at each pressure as input.

The results provide a comprehensive account of the solution properties of subcritical and supercritical fluids in the Ab-H_2O system at temperatures and pressures corresponding to the deep-crust regions of granite magma generation. Textures of quenched charges indicate that near-critical melts are extremely fluid, consistent with previous work. This may have considerable bearing on element transport, extractability of partial melt, and ultimate level of melt emplacement in the middle and upper crust.

1.1 Introduction

The variation in the H_2O content of granitic magmas plays a key role in controlling the extent of crustal melting, H_2O transport by magmas, the deep H_2O cycle and H_2O stored in the crust. Water also influences physical properties such as density and viscosity of granitic magmas, which determine how magmas can infiltrate and assimilate country rocks, ascend, and accumulate into larger bodies (Johannes and Holtz, 1991). While many investigations have focused on the H_2O content of granitic magmas at low to moderate pressure (< 0.5 GPa), relatively few have focused on the role H_2O on the phase relations of silicic magmas at higher pressures. This hinders better understanding of how H_2O influences crustal melting, fluid and magma evolution in subduction zones.

At high pressures, the phase relations in silicic magma-H_2O systems are complicated by the tendency of H_2O and silicate magma to mix completely (Boettcher and Wyllie, 1969; Stalder et al. 2000, Shen and Keppler, 1997; Hunt and Manning, 2012; Paillat et al., 1992). The significance of this behavior remains poorly understood. While the onset of complete mixing has been characterized for a few simple systems (Kennedy et al., 1962; Shen and Keppler, 1997; Bureau and Keppler, 1999; Newton and Manning, 2008), the detailed $\mathrm{P}-\mathrm{T}-X_{\mathrm{H_2O}}$ phase relations of a complex system approaching a granite have not previously been reported.

1.1.1 The model system $NaAlSi_3O_8$-H_2O

The compositions of simple granites are dominated by the oxide components SiO_2, Al_2O_3, Na_2O and K_2O. Other rock forming components occur (e.g., CaO, MgO, FeO, etc), but at concentrations that tend to have only minimal influence on physical and chemical properties. Accordingly, a useful simplification of the granite-H_2O system is the model chemical system $NaAlSi_3O_8$-H_2O. Alkali feldspar is the major mineralogical component of granites, and experimental studies have shown that hydrous melting of albite is closely analogous to that of the simple granite system with K-feldspar and quartz as well as sodic plagioclase. The $NaAlSi_3O_8$-H_2O system is also of special value in that a theoretical treatment of rock melting may be made on the basis of many existing physicochemical data, including calorimetric and $\mathrm{P}-\mathrm{T}-\mathrm{V}$ equation of state data for albite and H_2O. The extensive treatment of Burnham and Davis (1974) based on measured compressibility data of $NaAlSi_3O_8$-H_2O melts has outlined many of the most fundamental thermodynamic properties of the binary system, including partial molal entropy and free energy.

1.1.2 Previous work and outstanding problems

The experimental work of Goranson (1938) on the melting of albite in the presence of water laid the groundwork for all of the many subsequent studies. Goranson showed that H_2O at elevated pressures greatly lowers the melting point, from temperatures above 1100 °C to temperatures below 800 °C. His work, with extension to higher pressures by numerous investigators (Burnham and Jahns, 1962; Eggler and Kadik, 1979; Bohlen et al., 1982; Goldsmith and Jenkins, 1985(b); Hamilton and Oxtoby, 1986) resulted in a substantial understanding of melting relations in the binary system in the lower pressure range.

The experimental problem of determining the compositions of albite-H_2O melts at P and T ranges pertinent to the formation of granitic magmas (600-1200 °C and 0.2 to at least 1.5 GPa, corresponding to the deep-crust depth range) has proven difficult. Experimentally melted charges have had to be, until the recent development of the heated diamond cell apparatus, quenched from high P and T and studied by various microscopic and spectroscopic techniques. Even for very fast quench rates, changes occur in the solid quench products, usually glass and other amorphous materials, which compromise determination of the amount of H_2O dissolved in the melt and also of the partitioning of H_2O between hydrous melt and a coexisting H_2O-rich phase ("vapor"), if present. (Key terms, such as vapor, are defined in Table 1.1 as they used in the context of this study. Figures 1.1 and 1.2 use some of these terms the context of $T - X_{H_2O}$ and $P - T$ phase diagrams pertinent to this study)

The most successful determinations of the H_2O contents of $NaAlSi_3O_8$-H_2O melts at high P and T have been along the vapor-saturated melting curve, loosely termed the "solidus". The most effective method is chemographic, by adding H_2O to successive experiments until a

minimum melting temperature is obtained. This is usually accompanied by textural evidence of precipitation of silicate products from the quenched vapor phase, termed "globules" (Paillat et al., 1992) or "fish roe" (Boettcher and Wyllie, 1969). At supersolidus temperatures, where crystalline albite is not present, the problem becomes worse because vapor saturation must be recognized by textural interpretation of quenched charges, and identification becomes increasingly problematic as silicate solubility rises.

Determination of the composition of a vapor phase in equilibrium with a hydrous albite melt has been equally difficult. At low temperatures and pressures, where a quenched vapor phase can be extracted and analyzed independently, albite dissolves incongruently, with Si enrichment in the aqueous fluid and depletion of Na and Al relative to albite (Currie, 1968; MacMillan and Holloway, 1987). At higher T and P the most successful method for determining the composition of the vapor phase has been chemographic analysis (Anderson and Burnham, 1967; 1983). They concluded, as have subsequent investigators (Paillat et al., 1992; Stalder et al., 2000), that at temperatures above 700 °C and pressures of 1.0 GPa and higher, albite dissolution in H_2O is essentially congruent; that is, the system is truly binary at elevated P – T conditions.

The most serious problem in determining H_2O solubility in albite melts is exsolution of H_2O during the quench, which results in bubbles in the quenched glass for initial H_2O contents greater than 7 to 10 wt%, depending on the run conditions, the quench rate and the decompression P – T path. Consequently, estimates of H_2O solubility in the pressure range above about 0.5 GPa have relied on various methods of extrapolation from lower pressure measurements on bubble-free glass, guided by estimates of volumetric behavior in hydrous silicate melts (Holloway and MacMillan, 1986) and/or theoretical models of H_2O speciation,

whether in the form of H_2O molecules (Wasserburg, 1957), H_2O molecules and OH^- ions (Silver and Stolper, 1985), or H_2O interactions with Na^+ (Burnham, 1975).

All of these extrapolation models account for the great increase of H_2O solubility with pressure, but that increasing temperature at constant pressure causes a decrease in H_2O solubility. As noted by Paillat et al, if this "retrograde solubility" is everywhere applicable, it rules out the possibility of critical mixing between melt and fluid, such as is observed in the system SiO_2-H_2O (Kennedy et al., 1962; Newton and Manning, 2008). However, there are hints in the older experimental work that retrograde H_2O solubility may not be obtained at high pressures. Burnham and Jahns (1962) found, based on textural evidence of quenched charges, that H_2O solubility in albite melts starts to increase rather dramatically on the vapor-saturated melting curve at pressures above 0.7 GPa. Their measurement of nearly 18 wt% H_2O at 1.0 GPa and 690 °C is much higher than can be accounted for in the thermodynamic models of H_2O-albite mixing. Goldsmith and Jenkins (1985, b) made the most definitive measurements of the solidus temperature to pressures around 1.7 GPa, where it intersects albite breakdown to jadeite and quartz. Though they did not measure H_2O contents, they observed major textural changes in the quenched liquid in this pressure range, from bubbly glass at lower pressures to a frothy, friable substance near 1.7 GPa that must have been so H_2O-rich at run conditions that they pointedly refrained from calling it a glass, but used the term "fluid" instead.

Paillat et al.'s (1992) experiments challenged in a fundamental way the earlier model extrapolations. They made ion microprobe measurements of H_2O in vapor-saturated albite glasses quenched from pressures of 0.5 to 1.3 GPa and supersolidus temperatures above 900 °C. The H_2O contents were restricted to the range below 10 wt% and mostly bubble-free. The measurements clearly showed that, above about 0.5 GPa, the solubility is "prograde"; that is, it

increases with increasing temperature at constant pressure. They realized the profound implication of this observation: coupled with the large increase of solubility in H_2O with increasing temperature, as well as with pressure, the liquid and vapor phases must approach each other in composition and physical properties to produce, at some elevated P-T conditions, a critical $NaAlSi_3O_8$-H_2O mixture. They envisioned a critical $P - T$ curve bounding the two-fluid region. Based on the presence or absence of small silicate "globules" in quenched charges, which they interpreted as evidence for the existence of a separate H_2O-rich phase coexisting with melt, they suggested a critical temperature near 1200 °C at 1.3 GPa.

Paillat et al.'s (1992) proposed schematic $P - T - X_{H_2O}$ phase relations of $NaAlSi_3O_8$-H_2O changed the paradigm for future investigations. They predicted a critical end point on the hydrous melting curve of albite near 1.5 GPa and 665 °C, with > 40 wt% H_2O in the supercritical fluid (see Hack et al., 2007 for a full discussion of the critical end point in binary and more complex systems). The "singular point" of Boettcher and Wyllie (1969) near these P – T conditions, where albite was presumed to begin to melt incongruently to jadeite + liquid was reinterpreted as the critical end point, where the intersection of the melting curve with the critical curve annihilates both curves.

The prediction of critical phenomena in the system $NaAlSi_3O_8$-H_2O was dramatically confirmed by Shen and Keppler (1997) in one of the first applications radiographic imaging in the externally heated diamond-anvil pressure cell. Their results on $NaAlSi_3O_8$-H_2O mixtures in the supersolidus ranges of 1.0-2.0 GPa and 600-900 °C clearly indicated progressive disappearance with increasing P and T of a two-fluid-phase interface, resulting in an optically homogeneous one-phase (supercritical) fluid. Although pressures have high uncertainty in this device, and cannot be independently manipulated, the projection of the Shen and Keppler (1997)

critical $P-T$ curve would intersect the albite hydrous melting curve in the range 1.5-2.0 GPa, in accord with the prediction of Paillat et al. (1992).

Further investigation of critical phenomena in the albite-H_2O system by Stalder et al. (2000) made use of the diamond-trap method, in which a layer of fine-grained diamonds immersed in an encapsulated albite-water charge retains void spaces even at high pressures and temperatures, so that liquid and fluid phases produced during a melting experiment may infiltrate and be retained by the diamond layer. The quenched compacts were analyzed by laser-ablation mass spectrometry. Despite scattered data, Stalder et al. (2000) confirmed the very high H_2O contents of albite melts at pressures near 1.7 GPa and temperatures near 670 °C, supporting the concept of critical mixing near the H_2O-saturated melting curve.

1.1.3 Scope of the present work

Although the existence of critical mixing in the system $NaAlSi_3O_8$-H_2O has been established beyond reasonable doubt by previous investigations, the $P-T-X_{H_2O}$ topology of the system remains to be determined. There are two goals of the present work. The first is to map the isobaric two-fluid-phase loops at pressures approaching the postulated upper critical end point near 1.5-2.0 GPa and 650-700 °C, and to develop a quantitative thermodynamic model for the $P-T-X_{H_2O}$ phase relations. A second goal is to define the family of vapor-absent liquidus curves in the same $P-T$ ranges. H_2O contents of incipiently crystallizing feldspathic magmas have not yet been determined accurately at high pressures, in spite of the potential importance to the granite problem. The low-temperature terminus of the isobaric liquidus curves is a vital check on the H_2O content of the first-melting (solidus) temperature and a fiducial point on the two-fluid-phase loop (solvus). For this study, we adapted the method of textural analysis of

quenched charges of Burnham and Jahns (1962), updated with (1) modern petrographic tools such as scanning electron microscopy and (2) use of solubility measurements below the solidus. The results lead to a detailed characterization of the $P - T - X_{H_2O}$ phase relations of the albite-H_2O system near the critical end point on the melting curve, the most precise determination of the albite-H_2O liquidus surface yet obtained, and the first thermodynamic model of $NaAlSi_3O_8$-H_2O mixing for application to the problem of critical behavior.

1.2 Experimental Methods

1.2.1 Starting materials and capsule loading

Starting materials were a well-characterized natural low albite from Amelia County Court House, Virginia, USA, and ultrapure water of ~18 MΩ cm^2/cm. This albite was used by Newton and Smith (1967) to determine the stability relative to jadeite plus quartz. The largest impurity is < 0.11 wt% K_2O (Ribbe and Smith, 1966). Unit cell constants confirm low albite structural state (Newton and Smith, 1967). The albite was ground under acetone in an agate mortar for ~60 minutes until complete evaporation and then dried in an oven at 400 °C for ~30 minutes to volatilize the organic compounds. The grinding process was repeated in a second cycle.

Platinum tubing segments of ~1.25-1.75 cm length and 2 mm or 3.5 mm diameter were cleaned with acetone. The longer capsules of larger diameter were used in experiments that had very small mole fractions of water, as well as for solubility experiments where large amounts of both albite and water were needed. One side of the tubing was sealed in an oxy-acetylene flame and then the whole capsule was annealed with this flame. Weighed amounts of albite and water were sealed into the capsule by arc welding. Water mole fractions ranged from 0.035-0.99.

Amounts of total charge were 10-40 mg. Weighing was carried out on a Mettler Toledo UMX2 ultra-microbalance with a stated precision of 2×10^{-4} mg. The dry charge was weighed into a capsule, and then the H_2O was added with a microliter syringe. A volume of H_2O slightly larger than the target value was added and allowed to evaporate on the balance until the desired weight was reached. The capsule was then sealed by arc-welding. Weight loss on sealing was often less than 50 μg, all of which is attributable to platinum evaporation. Capsules were weighed before and after all runs. No detectable weight loss occurred during an experiment.

1.2.2 Piston-cylinder methods

Experiments were conducted in a piston-cylinder apparatus of either 2.54 or 1.91 cm diameter. Pressure measurements were made using a Heise Co. bourdon tube gauge. Pressure uncertainties were ±0.03 GPa. Graphite sleeves were used to heat the samples and temperature was digitally measured and controlled using S-type thermocouples. Temperature uncertainties were ± 3 °C. An all-NaCl pressure medium was used at $T \leq 950$ °C (Manning and Boettcher, 1994), but higher-temperature experiments required the use of small BN discs to prevent melting of the pressure medium in the vicinity of the capsule at the hot spot of the furnace assembly. The BN discs were 0.15 cm in length and placed immediately above and below the capsule. In addition, BN powder was packed around capsules in these high-temperature runs. The BN-NaCl pressure medium required a pressure correction of -0.6 GPa relative to the NaCl pressure medium. This was determined using quartz solubility experiments previously performed in our lab (Manning, 1994) in all-NaCl assemblies, and comparing the solubility at 1.0 GPa using the all-NaCl assembly with that found using the BN-NaCl assembly at 950 °C.

Experiments were held at desired P and T for varying times, depending on the temperature and H_2O content. Run products were rapidly quenched to below ~100 °C in ~20 s. Repeat experiments were made to assure time-independence of the measurements at several P, T conditions. Experimental times were generally < 24 hours at T > 1000 °C, and up to two weeks for temperatures near the H_2O-saturated solidus (~700 °C).

1.2.3 Solubility measurements

Solubility measurements on albite were made to determine the isobaric-invariant composition of the H_2O-rich limb of the solvus at the solidus. Following the same methods presented in the study of quartz solubility in aqueous fluids by Newton and Manning (2008), measurements were made at P – T conditions immediately below the solidus temperatures at each pressure. The results of Goldsmith and Jenkins (1985, b) on low albite melting at low pressure were used as a guide. The solubility of albite is reported on a weight percent basis as the amount of albite dissolved in solution divided by the total mass of the solution (i.e. dissolved albite plus water).

Two types of solubility experiment were carried out: Ab_1 experiments nominally give a direct solubility determination, whereas Ab_2 experiments bracket solubility between upper and lower bounds. The Ab_1 experiments were single-crystal weight-loss solubility runs conducted on polished albite crystals. Amelia albite crystals were hand picked so as to fit loosely into a 1.6 mm diameter platinum inner capsule. The crystals were smoothed with a diamond file to remove edges and then polished by rolling them between two pieces of silicon carbide grinding paper. Successively finer grit grinding paper was used, starting with 400, 600 then 800 grit paper to achieve a subspherical shape. The crystals were then rinsed with ethanol, sonicated to remove

any fragments of albite and/or sandpaper attached to the single crystal, and dried at 600 °C to remove any organic material. A single crystal was then loaded in the inner capsule and pinched lightly in order allow H_2O fluid flow through the inner capsule. After the experiment was run at the desired P and (subsolidus) T, the inner capsule was removed, rinsed with water, sonicated and dried at 100 °C. The weight loss of the inner capsule after the experiment corresponds to the amount of albite dissolved in the solution. Because of the possibility of very small fragments of albite crystals that may be lost in the weighing process, only a maximum on the solubility measurement can be reported using this method.

Experiments of type Ab_2 bracket the solubility by determining the composition range between which albite disappears from the charges. The presence or absence of crystals after the run was determined using a petrographic microscope. Complete dissolution of the albite gives a minimum solubility measurement, and charges that were saturated with albite give a maximum solubility. The minimum, maximum and average solubility are reported using this alternative method. Ab_2 experiments are preferred at higher pressures because of the deep solution channels along fractures or cleavage planes that arise from the high solubility of albite, which in turn can cause the crystal to fragment into many small pieces and render Ab_1 experiments inaccurate.

1.2.4 Interpretation of run products

Interpretation of the run products was carried out with reference to the schematic isobaric $T - X_{H_2O}$ section (Fig. 1.1) of a binary system with large depression of the liquidus (bounding curve of liquid + albite field) with H_2O content, and an aqueous fluid-silicate melt immiscibility field that decreases in area with increasing pressure until a critical end point pressure may be reached. The critical end point occurs at elevated pressure and temperature and is sometimes

called the second or upper critical end point to distinguish it from a lower P – T such point near the critical point of pure H_2O (Fig. 1.2). The only other binary mineral-H_2O system showing critical end points that has been investigated in detail is quartz-H_2O (Kennedy et al., Newton and Manning, 2008, Hunt and Manning, 2012).

Phase relations involving hydrous albite liquid (L) and H_2O-rich fluid (V) were determined from textural analysis of run products by binocular, petrographic and scanning electron microscopy. At each pressure the experiments bracketed the liquidus curve, the topology of the L + V miscibility gap, and the temperature of critical mixing (T_C). Criteria for assigning the results to a particular field are given below with specific examples. The schematic diagram (Fig. 1.3) shows the textural criteria used to distinguish the different phases observed after quenching the run products. While some charges were easily interpretable under a binocular microscope and/or in immersion oil using a petrographic microscope, others required characterization by scanning electron microscope (SEM), particularly in experiments in which the systems was supercritical or nearly so prior to quenching. All samples were carbon coated and analyzed using a Tescan Vega-3 XMU SEM, with secondary electrons.

1.2.4.1 Liquid field

Quenched run products assigned to the liquid field were characterized by the presence of a single homogenous glassy phase. Water exsolution during quenching gives rise to bubbles in the glass, for initial H_2O contents of more than about 8 wt% (Fig. 1.4A). Bubble density and size in quenched glass increased as H_2O content increased across the liquid field at a fixed P and T, up to H_2O saturation. The correlation of bubble density and size with H_2O content was evident

from observations made on the SEM by comparing the quenched glasses at nearly identical magnification levels (Figs. 1.4C-D).

1.2.4.2 Liquid plus vapor field

In this field, evidence for two phases is observed: a silicate-rich phase (the liquid), and a second is the water-rich phase (the vapor). Inside the miscibility gap, on the low water side of the solvus, quenching forms clear glass balls (the quenched vapor phase seen in Fig. 1.4B), inside vapor pockets formed near the pinched ends of the capsule during the run. This is a modification of the textural criteria used by Burnham and Jahns (1962) to infer the existence of a separate aqueous fluid phase coexisting with a silicate. The solute component of the H_2O-rich vapor phase precipitates as clear glass spheroids during the quenching process.

A large porcelaneous spheroid of hydrous glass coexisting with myriad small spherules is observed in charges quenched from inside the miscibility gap at high H_2O contents (Fig. 1.5A). The high density of tiny bubbles in the spheroid causes strong light scattering, giving it a milky white appearance that is clearly evident under the binocular microscope. The smaller clear spheroidal balls are interpreted as having quenched from the coexisting H_2O-rich phase.

With increasing temperature at a given pressure, the two fluids approach each other in composition and physical properties, so that the quenched charges become harder to interpret texturally. At temperatures just below T_C, pieces of quenched glass commonly display two distinct regions of different bubble size. These are interpreted to correspond to the quenched hydrous liquid and the quenched solute-rich vapor phase (Fig. 1.5B). The liquid, which would have quenched to a bubbly porcelaneous glass spheroid at a lower temperature, is at higher temperature the highly bubbly portion of the glass pieces that show an interface. Bubbles in the

more bubble-poor region are larger, and the material often appears to be a welded masses of clear spherules. This is interpreted to represent the quenched vapor. Two additional observations support this interpretation. First, the clear glass balls forming from the bubble-free portion of the glass (Fig. 1.5B) are prima facie evidence that the glass with fewer bubbles is in fact the quenched fluid phase. Second, at higher H_2O contents, the amount of highly bubbly glass decreases, and is replaced by clear glass balls that are quenched from the aqueous vapor phase.

On the water-rich limb of the solvus, experiments that are interpreted to have been inside the miscibility gap show mostly clear glass balls, with only a few small chunks of porcelaneous glass, the former liquid. The location of the boundary between the L + V and V field is constrained by the most H_2O-rich run containing milky glass and the most H_2O-poor run in which no glass is observed.

1.2.4.3 Vapor field

Experiments quenched from the vapor field contain myriad clear glass balls, sometimes welded together (Figs. 1.5C-D). The vapor balls are ~5-200 μm in diameter, are often welded together, and contain tiny exsolution bubbles on the order of one to a few microns in diameter. Some experiments show paragonite that forms during quenching (Fig. 1.5C) and is interpreted to be unstable at the run conditions, consistent with Boettcher and Wyllie (1969).

1.2.4.4 Supercritical fluid field

The supercritical fluid phase appears at the point in $P - T - X_{H_2O}$ space where the distinction between coexisting quenched phases vanishes (Fig. 1.6). For each $T - X_{H_2O}$ binary, experiments were conducted at different temperatures while holding the H_2O content fixed in the range of ~40-60 wt% H_2O. Supercritical fluids in this composition range quenched to opaque,

white, bubble-rich glass. The size distribution, shape and bubble integrity in glass quenched from supercritical fluid varied with P and T. Although charges can contain numerous clear glass balls as well, an interface of the type seen in Figure 1.5B is notably absent. Only charges quenched at sub-critical temperatures (~0-50 °C) can display this type of texture. Quenched supercritical fluid in experiments carried out at P greater than the critical end point coexists with albite.

1.3 Results of Experiments

Experimental results are tabulated in Table 1.2. Below I describe results in terms of the $T - X_{H_2O}$ phase relations at five pressures: 1.0, 1.25, 1.4, 1.6 (Fig. 1.7A-D) and 1.7 GPa (Fig. 1.8). In each isobaric $T - X_{H_2O}$ section, the dry melting temperature of albite was taken from Boyd and England (1963). For experiments at subcritical conditions, the results constrain the three main near-solidus and supersolidus aspects of a $T - X_{H_2O}$ section: the liquidus, the location and shape of the miscibility gap between liquid and vapor, and the solubility of albite in the vapor.

1.3.1 1.0 GPa

At 1.0 GPa (Fig. 1.7A), the experimental data constrain the solidus to be at 693 ±10 °C. The liquidus was bracketed between the dry melting temperature and the solidus at 50 °C intervals between 700-950 °C. The liquidus bracket and the low water solvus bracket at 700 °C constrain the vapor-saturated solidus at 21.02 ± 1.54 wt% H_2O. Just below the solidus at 685 ± 3 °C, the composition of albite-saturated vapor was constrained to be 90.65 ± 2.85 wt% H_2O. The topology of the L + V field is tightly constrained by experiments at T < 900 °C and ≥

1000 °C. The L + V envelope constrained by these experiments agrees with the independently determined intersection of the liquidus and solidus and the near-solidus composition of albite-saturated vapor. The critical composition and temperature are ~ 45 wt% H_2O and 1048 ± 13 °C, respectively. Our critical temperature is ~150 °C higher than estimated by Hayden and Manning (2011) at the same pressure.

Some experiments in the range of 900-1010 °C and 25-30 wt% H_2O are plotted to the left of the model solvus. These charges, interpreted as two-phase assemblages, had very few (1-5) and miniscule clear glass balls comprising << 1% of the total volume of the charges. By the criteria set forth, these points were required to be classified as having a vapor phase present prior to quenching.

On the water-rich limb of the solvus, particularly between 900-950 °C and within a few weight percent of the modeled solvus, the L and V were nearly indistinguishable due to the limitations of the textural method. As a result, some inconsistencies arose as is seen by the overlap of some of the data points in the L + V and V only region of the diagram (Fig. 1.7A).

1.3.2 1.25 GPa

At 1.25 GPa (Fig. 1.7B), the experimental data constrain the solidus to be at 683 ±13 °C. The liquidus was bracketed between the dry melting temperature and the solidus at 100 °C intervals between 700-900 °C. The bracket separating the L + albite field from the L + V field at 700 °C constrain the vapor-saturated solidus at 22.85 ± 2.65 wt% H_2O. Just below the solidus at 675 ± 3 °C, the composition of albite-saturated vapor was constrained to be 77.57 ± 0.15 wt% H_2O. Extrapolation of the water-rich limb of the solvus to the solidus is largely in agreement with the subsolidus solubility measurements, constraining it at 74.19 ± 3.54 wt% H_2O. Due to

the strong enhancement of the solubility of albite at subsolidus temperatures nearing the solidus, it is likely that the albite-saturated vapor value is nearer the low end of this bracket at ~ 71 wt% H_2O. The L + V miscibility gap is well constrained from 25.39-70.72 wt %H_2O and between temperatures between 700 and 960 °C. The critical temperature has come down with increasing pressure to 940 ± 23 °C, yet still occurs at ~45 wt% H_2O. All of these changes result in substantial shrinking of the miscibility gap.

1.3.3 1.4 GPa

At 1.4 GPa (Fig. 1.7C), the experimental data constrain the solidus at 679 ± 17 °C. Extrapolation of the liquidus from the dry melting T through the brackets at 700-900 °C to the solidus together with extrapolation of the brackets defining the water-poor limb of the solvus to the solidus brackets the vapor-saturated solidus at 30.88 ± 1.25 wt% H_2O. Solubility measurements gave a value of 70.61 wt% H_2O at 665 ± 3 °C. Extrapolation of the water-rich limb of the solvus to the solidus constrained the lower bound at ~ 61.5 wt% H_2O. Combining the solubility data with the extrapolation of the water-rich solvus limb constrains the albite-saturated vapor value at 66.05 ± 4.56 wt% H_2O. The critical temperature has come down significantly to 835 ± 28 °C, yet still occurs at ~45 wt% H_2O.

The uncertainty in the composition of the near-solidus albite-saturated vapor becomes more pronounced at pressures near the critical end point pressure (i.e. 70.61 wt% H_2O vs. ~ 61.5 wt% H_2O). It is likely that the value for the albite-saturated vapor is closer to ~ 61.5 wt% H_2O (i.e. the value predicted by extrapolating the brackets constraining the water-rich limb of the solvus to the solidus).

1.3.4 1.6 GPa

At 1.6 GPa (Fig. 1.7D), the experimental data constrain the solidus at 668 ± 6 °C. Extrapolation of the liquidus from the dry melting T through the brackets at 670-900 °C to the solidus places the vapor-saturated solidus at ~ 42 wt% H_2O. The composition of albite-saturated vapor was constrained to be at a maximum value of 57.89 ± 2.58 wt% H_2O at 665 ± 3 °C. Experiments conducted at supersolidus temperatures show a critical point near 50 wt% water and ~700°C. The experiment at 690 °C and 49.9 wt% water (AB140) shows a highly bubbly phase fused with a non-bubbly glass phase, indicating that a miscibility gap, albeit it a very small one, likely exists at these conditions.

1.3.5 1.7 GPa

The only criterion used at 1.7 GPa to map out the phase boundary is the presence or absence of crystals in the quenched charges (Fig. 1.8). The curve at this pressure is in essence a solubility curve of the type Ab_2. At 1.7 GPa, we could find no evidence of two phases coexisting over a large range of compositions and temperatures ranging from 4-80 wt% water and 630-1050 °C. We therefore place a critical end point on the fluid-saturated melting curve of albite between 1.6 and 1.7 GPa at 1.65 ± 0.08 GPa, 665 ±10 °C, and ~ 45 wt% water in accordance with the nearly constant critical composition observed at lower pressures. In addition, albite continues to be a stable crystalline phase that coexists with a supercritical fluid at temperatures above 650°C. Geometrical crystals up to half a millimeter were grown from this supercritical fluid. X-ray diffraction yielded a value of $2\theta_{131} - 2\theta_{1\bar{3}1}$ of 1.06 for Cu Kα radiation, indicating a maximally low structural state (Goldsmith and Jenkins, 1985(a)). Repeated experiments

conducted at 650 °C and 50 wt% water at 1.7 GPa reproduced the equilibrium low albite-supercritical fluid.

1.4 Discussion

1.4.1 Liquidus

Liquidus composition measurements were made at 1.0, 1.25, 1.4, 1.6 and 1.7 GPa. With increasing pressure, the liquidi move to higher temperatures. The full liquidus curves are presented in the in the Figures 1.7 and 1.8. Extrapolation of the solvus to slightly lower temperatures at the solidus serves as independent confirmation of the location of beginning of melting at the vapor-saturated solidus (Figs. 1.7 and 1.8). A comparison of the five liquidus curves plotted up to 12 wt% H_2O is shown in Figure 1.9 in order to focus on compositions of interest for fertility calculations. For example, albite in the deep crust with 4 wt% H_2O available at 1.0 GPa and 900 °C would be able to produce ~ 57.1 wt% melt, whereas that same system at 1.6 GPa and 900 °C would only be able to produce ~ 48.5 wt% melt.

1.4.2 Solidus

The solidus was bracketed by the solubility experiments conducted at temperatures below 700 °C (Table 1.3) as well as by supersolidus experiments conducted at temperatures slightly above those of the solubility measurements.

The curve of the vapor-saturated solidus determined here between 1.0 and 1.7 GPa (Fig. 1.10) extrapolates smoothly from the lower pressure determinations made by Burnham and Jahns (1962). It is seen to be a smooth continuation of the accelerating trend to 1.0 GPa observed by

Burnham and Jahns (1962), using essentially the same methods. The slope of the $T - X_{H_2O}$ projection of the vapor-saturated solidus approaches infinity at the critical composition, ~45 wt% H_2O at all pressures investigated. Our results deviate from the theoretical determinations made by Silver and Stolper (1985), which do not incorporate the possible onset of critical phenomena.

1.4.3 Albite solubility

Albite was found to congruently dissolve in H_2O over the pressures and temperatures investigated: 1.0 GPa and 685 °C, 1.25 GPa and 675 °C, 1.4 GPa and 665 °C, and 1.6 GPa and 665 °C. Incongruent solubility of albite to paragonite was observed in Run AB74 at 1.25 GPa and 650 °C. This charge was a felted mass of paragonite, whereas other experiments in this low temperature range at 1.7GPa had hydromica or paragonite as a quench product, but not a stable phase. The solubility experiments listed in Table 1.3 were checked for possible breakdown to jadeite and liquid with a petrographic microscope, placing the ground charge in immersion oil of index 1.596 to differentiate between the different refraction indices of albite and jadeite. Jadeite was not found in any of these experimental charges.

The solubility of albite in H_2O strongly increases as a function of pressure in this range as well (Fig. 1.11). This very large increase in solubility moves the vapor-saturated albite value to decreasingly lower water contents and therefore narrows the miscibility gap on the water-rich limb of the solvus at the solidus. For example, the solubility of albite in water at 1.0 GPa and 685 °C was 9.35 ± 2.85 wt%, whereas at 1.6 GPa and 665 °C it was 42.11 ± 2.58 wt%.

At 1.7 GPa (Fig. 1.8) the phase boundary separating supercritical fluid from the albite stability field was constrained to be essentially flat in the middle of the diagram. In this region, measurements are highly sensitive to temperature as the solidus is approached from below. A

small decrease in temperature at fixed pressure (~10 °C or greater below the solidus) can have a large effect on the solubility measurements. This can shift the vapor-saturated albite values to significantly higher water contents, which was likely the case at 1.25 and 1.4 GPa (Figs. 1.7B-C) to since the H_2O-rich limb of the solvus does not extrapolate exactly to the solubility measurement for albite. So, while the solubility measurement does serve as an upper bound where the water rich limb of the solvus intersects the solidus, the temperature sensitivity of the measurement suggests that it is more appropriate to place this point of intersection (as done in this study) nearer to the extrapolated solvus to the solidus. The solubility curves using both methods are presented in Figure 1.11. Inability to make the solubility measurements arbitrarily close to the solidus was a limitation of this method, when in theory the solubility measurements should make an unambiguous determination of the invariant point.

1.4.4 The liquid-vapor solvus and critical mixing

Figure 1.12 is a summary of the pertinent phase relations of the present work and that of others. The new data on the vapor-saturated solidus extrapolates smoothly from the data collected by Burnham and Jahns (1962). The rapid increase of H_2O content at the solidus in the range of pressures investigated here may be considered to be premonitory to an eventual critical end point. Thermodynamic modeling of solidus water contents at lower pressures successfully reproduce the solubility data in this range (Silver and Stolper, 1985), but as they acknowledge, would not be useful for the onset of critical phenomena which might occur in a higher pressure range (Fig. 1.10).

Figure 1.12 also shows the P – T trace of our isobaric solvus crests with uncertainties. It is largely in agreement with critical curve determined by Shen and Keppler (1997) using optical

microcopy in an externally heated diamond-anvil pressure cell. The pressure determination in the piston cylinder apparatus is superior to that of the diamond anvil cell, which has to be calibrated with internal standards.

Hayden and Manning (2011) presented solubility measurements of rutile in Ab-H_2O solvents as a function of pressure that indicate that, at some pressure above 2.0 GPa at 900 °C, a two-fluid phase reappears. The way in which this "anti-critical" curve may intersect the other phase equilibrium relations is not known at present and remains an important problem for future investigation. Boettcher and Wyllie (1969) found that jadeite + quartz + H_2O mixtures on the join Ab-H_2O at pressures above 2 GPa undergo melting in the presence of a vapor phase analogous to that which occurs below 1.5 GPa. This would be consistent with Hayden and Manning's (2011) interpretation.

Our data show the intersection of the vapor-saturated solidus with our determined critical curve in the range of 1.6-1.7 GPa at approximately 665 °C. We thus infer the existence of a stable critical end point on the hydrous melting curve of albite supporting the earlier interpretations of Paillat (1992) and Stalder et al. (2000). Goldsmith and Jenkins (1985, b) showed that there is large difference in the melting temperature of low structural state albite and that of low albite in the pressure range of 0.5-0.75 GPa and temperature range below 750 °C which is the high-low inversion temperature in that pressure range. Figure 1.13 shows that our inferred critical end point falls above the melting point of low albite, which, according to the determinations of Goldsmith and Jenkins (1985, b) would be the stable form of albite at the melting point. This is consistent with our X-ray determination of a low structural state of albite crystallized at P and T near the critical end point (Fig. 1.12).

In addition, Figure 1.13 shows the location of Boettcher and Wyllie's (1969) singular point, S_6, which they interpreted as the onset of incongruent melting of albite + vapor → jadeite + quartz. However, Goldsmith and Jenkins (1985, b) synthesized low structural state albite in P – T range above our critical end did not find the appearance of jadeite at pressures below the breakdown of albite→ jadeite + quartz.

Paillat et al. (1992) reinterpreted Boettcher and Wyllie's singular point, S_6, as a critical end point on the hydrous melting curve of albite, and this was reiterated by Stalder et al. (2000). Our experimental results provide strong support for these earlier conjectures. The existence of a stable critical end point on the hydrous melting curve of albite is somewhat similar to that of quartz melting near 1.0 GPa and 1080 °C (Newton and Manning, 2008). The lower T and higher P as compared to that of quartz presumably is the result of NaAl component which replaces one of the Si of pure silica.

The textures of quenched supercritical fluids with 50 wt% H_2O (Fig. 1.6) change with increasing P (and decreasing T). At 1.0 GPa (Fig. 1.6A), bubbles in the quenched supercritical fluid are nearly spherical, retain their integrity and show relatively small variation in diameter of a few tens of mm. At 1.25 GPa (Fig. 1.6B), bubble integrity is maintained but some bubbles depart from sphericity, perhaps reflecting decreasing viscosity of the fluid, and bubbles show a greater range in size. At 1.40 GPa (Fig. 1.6C), the quenched supercritical fluid shows irregularly shaped cavities instead of spheroidal bubbles, with widely varying sizes. At 1.7 GPa the system is interpreted to be at P greater than the critical end point on the melting curve (Figure 1.8). The quenched supercritical fluid (Fig. 1.6D) coexists with albite and quenched supercritical fluid. It is apparent that high fluidity inhibits bubble formation. The frothy one-phase glass quenched from all points in the mid-composition range at 1.70 GPa shows that this pressure is unambiguously

above P_C. Large albite crystals in runs AB162 and AB163, show that a temperature of 650 °C is at albite saturation at 1.70 GPa (Figure 1.6D). We found no evidence of incongruent melting of albite → jadeite + liquid, as reported by Boettcher and Wyllie (1969).

1.4.5 Thermodynamic model of liquid-vapor mixing

1.4.5.1 Liquid-vapor mixing properties

Following Blencoe (1992), we derive a classical two-parameter Margules expression to model the P- and T-dependent variation in the L-V miscibility gap. The two-fluid envelopes determined in this work are somewhat asymmetric. Thus, it is appropriate to quantify the excess free energy of mixing by the Margules subregular solution model. Although it is possible to use the midpoints of experimental brackets of the solvi to determine purely empirical P and T dependence of the Margules parameters, W_{Ab} and W_{H_2O}, a more general approach is used here to formulate P- and T-dependent expressions of W_{Ab} and W_{H_2O}, which could be applied to other two component systems that exhibit solid-liquid-vapor equilibrium with critical phenomena.

Use of $NaAlSi_3O_8$-H_2O as mixing units on a $T - X_{H_2O}$ plot is awkward because of the great disparity in molecular weight between the components. This problem was mitigated by Silver and Stolper (1985) by choosing the mixing units as *one* oxygen in $NaAlSi_3O_8$ and the oxygen in H_2O. The same approach was used by Knapp and van Vorst (1959) in their study of silicate melt structures and activities. Hunt and Manning (2012) also successfully used this model in their study of the quartz-water system. We used this procedure to evaluate the Margules parameters and derive the activity-concentration relationships. The Ab mixing unit is taken as 1/8($NaAlSi_3O_8$), with a molecular weight of 32.78.

The Margules asymmetric solution model expands the Gibb's excess free energy of mixing as a third order polynomial for a two component system

1.1 $\bar{G}_{excess} = A + B\,X_2 + C\,X_2^2 + D\,X_2^3$

where A, B, C and D are the coefficients for the terms in X_2, the mole fraction of species 2. This method has been used many times throughout the Earth science literature to describe subregular binary solutions. A thorough development is given in Thompson (1967) and Spear (1995).

The Margules parameters at a given P can be linearized as a function of temperature between those at the critical temperature, T_C, and those at the solidus temperature, T_{sol}. The equations that describe the Margules parameters, and the resulting activity and composition relations spanning 1.00-1.60 GPa and 650-1050 °C are:

1.2 $W_{Ab}(T,\ T_C, P, X_{Ab,Tc}, X_{H_2O,Tc}) = W_{Ab}^{Tc}(T_c, X_{Ab,Tc}, X_{H_2O,Tc}) + \frac{T_c(P)-T}{T_c(P)-T_{sol}(P)}\,[W_{Ab}^{sol}(P) - W_{Ab}^{Tc}(P)]$

1.3 $W_{H_2O}(T,\ T_C, P, X_{Ab,Tc}, X_{H_2O,Tc}) = W_{H_2O}^{Tc}(T_c, X_{Ab,Tc}, X_{H_2O,Tc}) + \frac{T_c(P)-T}{T_c(P)-T_{sol}(P)}\,[W_{H_2O}^{sol}(P) - W_{H_2O}^{Tc}(P)]$

where,

1.4 $T_{sol}(P) = -40.586P + 1007$ K

1.5 $T_C(P) = -377.72P^2 + 380.94 + 1321.1$ K

1.6 $W_{Ab}^{sol}(P) = -29624P^3 + 139787P^2 - 222544P + 136944$ J/mol

1.7 $W_{H_2O}^{sol}(P) = 119971P^3 - 507902P^2 + 706645P - 309920$ J/mol

1.8 $W_{Ab}^{Tc}(T_c, X_{Ab,Tc}, X_{H_2O,Tc}) = \frac{RT_C}{6X_{Ab,Tc}X_{H_2O,Tc}}(9X_{Ab,Tc}X_{H_2O,Tc} - X_{Ab,Tc} - 1)$

and

1.9 $W_{H_2O}^{Tc}\left(T_c, X_{Ab,Tc}, X_{H_2O,Tc}\right) = \frac{RT_C}{6X_{Ab,Tc}X_{H_2O,Tc}}(9X_{Ab,Tc}X_{H_2O,Tc} - X_{H_2O,Tc} - 1)$

Equations 1.2-1.9 require P in GPa and T in Kelvins. The last two equations are those required of a critical subregular solution. The average of the critical compositions on a mole fraction basis was X_{H_2O}= 0.60 (corresponding to 45 wt% H_2O) and X_{Ab} = 0.40 (note the mixing units are based on a 1:1 oxygen mixing ratio, thus the molecular weight of albite was divided by 8 for these calculations).

The Margules parameters at the solidus temperature are determined by setting the activity of H_2O equal in coexisting melt and vapor, and likewise for the activity of Ab:

1.10 $a_{Ab,L} = a_{Ab,R}$

1.11 $a_{H_2O,L} = a_{H_2O,R}$

where the activity of each component is given by:

1.12 $ln\, a_{Ab} = ln\, X_{Ab} + (1 - X_{Ab})^2\left[W_{Ab} + 2X_{AB}\left(W_{H_2O} - W_{Ab}\right)\right]$

1.13 $ln\, a_{H_2O} = ln\, X_{H_2O} + (1 - X_{H_2O})^2\left[W_{H_2O} + 2X_{H_2O}\left(W_{Ab} - W_{H_2O}\right)\right]$

A system of equations can then be set up to solve for both W_{Ab}^{sol} and $W_{H_2O}^{sol}$ at each pressure. This procedure is repeated at each P to determine the pressure dependence of both terms outlined in equations 1.6 and 1.7. A minimization program can be set up using Microsoft Solver in Excel that simultaneously satisfies the conditions at the solvus stated in Equations 1.10 and 1.11, which, in turn gives the two solvus points at any temperature. Due to the close proximity of the

two solvus points at a specified T and 1.6 GPa, Solver was unable to find a solution other than the trivial solution. Therefore, the solvus curve at 1.6 GPa was drawn to satisfy the bracketed phase boundaries.

1.4.5.2 Uncertainties in the model

The error in the model was quantified by calculating the difference between the water contents of model prediction and bracket midpoints versus the water content of bracket midpoints (Fig. 1.14). This procedure was done to the three lower pressure solvi at 1.0, 1.25, and 1.4 GPa. The analysis shows that the data points are randomly distributed around zero, with the exception of the error for the solvus at 1.25 GPa, which slightly overestimates the experimentally determined water content of the solvus. The model reproduces 93.8% of the data points to within ± 4 wt% H_2O, 78.1% of the data points to within ± 3 wt% H_2O, and 100% of the data points to within ± 6 wt% H_2O of the model.

1.5 Applications to Petrology

Feldspar-rich liquids are formed in nature by hydrous melting of amphibolites and metasediments in subduction zones and of the tonalite-trondhjemite-granodiorite (TTG) gneisses and metasediments that are believed to make up much of the deep continental interiors. These magmas may, to a close approximation, be modeled in the simple system $NaAlSi_3O_8$ (Ab)-$KAlSi_3O_8$ (Or)-SiO_2 (Qz)-H_2O. Burnham and Jahns (1962) have shown that the four-component system may, in turn, be approximated in many of its phase relations and physical-chemical properties by the two-component subsystem $NaAlSi_3O_8$-H_2O. Inasmuch as the two-component subsystem SiO_2-H_2O also shows critical phenomena, with a critical end-point on the hydrous

melting curve of quartz at 0.97 GPa and 1080 °C, very near to the critical temperature in the Ab-H_2O system at that pressure, it seems likely that the simple hydrous granite system becomes supercritical, or nearly so, in continental margin subduction zones or at the deep-crustal pressures (>1 GPa) and magmatic temperatures (>900 °C) that characterize reactivated cratonal roots (Jayananda et al., 1995). Bureau and Keppler (1999) found evidence of a critical curve in the hydrous simple granite system at 1.30-1.69 GPa and 830-1000 °C by optical observation of phase assemblages in an externally heated diamond anvil pressure cell. Though pressures cannot be manipulated independently and have large uncertainty in this type of apparatus, their critical curve is quite comparable to that determined in the present study for Ab-H_2O. Moreover, the fluid-saturated solidus melt coexisting with feldspar and quartz becomes increasingly sodic and SiO_2 poor at pressures >1 GPa (Luth, 1976), so that granitic liquids formed by partial hydrous melting of quartzofeldspathic rocks would be close to the subsystem $NaAlSi_3O_8$-H_2O in composition. For these reasons, this subsystem is an attractive model for magma generation at deep crust/subcrustal levels.

The salient difference in behavior of quartz-feldspar-H_2O systems at near-critical pressures and temperatures (i.e. where H_2O-rich melts and silicate-rich aqueous solutions approach each other in composition and properties) is that fluids generated by mineral dehydration or other processes may acquire indefinitely large amounts of silicate components without undergoing a discrete phase change such as melting. Moreover, our evidence suggests that very silicate-rich solutions (or very H_2O-rich melts) become largely depolymerized with pressures above about 1 GPa, with attendant great decrease in viscosity, but further studies are required to verify this statement. The mobility, or ease of penetration of deep-crust/upper mantle rocks of low permeability, of ordinary magmas would be greatly enhanced, while chemical

reactions with host rocks would be expected to be quite different from that of either more dilute aqueous fluids or H_2O-poor silicate liquids, and might combine the metasomatic capability of both kinds of fluids, specifically the ability to transport alkali elements and halogens while retaining significant solubility for ferric iron, Ti, and the alkaline earth elements, which are very insoluble in dominantly aqueous fluids. Our experiments have demonstrated the great fluxing power of near-critical $NaAlSi_3O_8$-H_2O fluids for feldspar recrystallization by the growth of large crystals of maximally low albite at temperatures as low as 650 °C.

It may be possible to form very H_2O-rich, silicate-rich fluids of arbitrary compositions at sufficiently high pressures where there is access to large amounts of H_2O, as in relatively cool subduction zones undergoing dehydration reactions, since, lacking the formation of a competing fluid phase (i.e. a silicate melt) that could siphon off H_2O, there is no theoretical limitation on the hydration states of such fluids. Bureau and Keppler (1999) point to fluid-melt inclusions in mafic and ultramafic rocks of mantle origin, which have approximately equal amounts of hydrous fluid and silicates.

Zones of subduction of rapidly buried oceanic sediments and lavas containing the very hydrous, high P/T metamorphic minerals serpentine, phengite and lawsonite are environments where supercritical melt-like fluids of very high H_2O content are likely to form as these minerals reach their dehydration temperatures. Conditions of P >1 .0 GPa and T < 700 °C, estimated for recrystallization of the Catalina (California) Schist (Bebout and Barton, 1993), would, in the presence of an active aqueous fluid, be near-critical. The term “migmatites” applied by these authors to the pervasive quartz-feldspar vein complexes which characterize the Catalina Island subduction terrain may be appropriate in its magmatic context in view of the P – T conditions, described in the present paper, under which magmatic and hydrothermal processes in common

rocks lose their distinction. We find that albite continues to melt (or dissolve) congruently in the presence of H_2O to pressures immediately adjacent to the high-pressure breakdown of albite to jadeite and quartz, and therefore that the presence of jadeite in high P/T rocks implies either pressures greater than albite breakdown or silica deficiency, even if a H_2O-rich fluid was present.

The possibility also exists that supercritical or near-critical H_2O-rich silicate melts may be of importance in high-temperature reactivation processes in the cratonal, or interior continent environment. Some workers dismiss this possibility on the grounds that the only feasible source of H_2O for melting is thought to be resident in the hydrous mafic minerals, biotite and amphibole (Stevens and Clemens, 1993). The maximum amount of H_2O available would not exceed one weight percent, even for very ferromagnesian granites. However, other authors cite reasons to believe that much larger amounts of H_2O are sometimes present. Wickham and Taylor (1985) and McLelland et al. (2002) consider that large amounts of water of surficial origin could be carried downward to sites of partial melting in continental interiors in thermally driven convection cells. Other sources of H_2O for deep melting could be exsolution from very hydrous basalts intruded into the deep crust (Webster et al., 1999; Litvinovsky and Podladchikov, 1993) and brines of various origins (Aranovich et al., 1987).

If such supercritical fluids can be generated in interior-continent settings, there may be application to several features commonly observed in granitic bodies and to conjectures regarding the segregation of granitic liquids from sites of melting. These include the apparent ease of segregation (extractability) of deep-crust-generated granitic liquids, the possibility that granitic liquids can be agents of pervasive metasomatism in the deep crust and upper mantle, and the conspicuous localization of granites and migmatites in the middle and upper crust.

Several authors have remarked on the paucity of large granite bodies in the deep crustal granulite facies terrains (e.g. Heier, 1973; Alberti and Comin-Chiaramonte, 1976) despite the classical interpretation of granites as the culmination of regional metamorphism (Brown and Fyfe, 1970). An often cited explanation is that granite liquids can be efficiently extracted in very small melt fractions in spite of the supposed high viscosity of even H_2O-rich liquids. Rock deformation and consequent non-hydrostatic stress have been invoked as a mechanism (Sawyer, 1993). Very fluid melts at deep-crustal pressures and temperatures provides an alternative explanation for effective extraction of granitic liquid, once generated. It is possible that granitic liquids, even those with restricted H_2O contents, are so fluid and buoyant at deep crustal pressures that they may be considered "ephemeral" in terms of residence time, analogous to carbonatites produced by partial melting in the mantle (Green and Wallace, 1988).

Several workers have discussed the possibility that H_2O-rich felsic liquids could be an important factor in metasomatic alteration of the deep crust (Alberti and Comin-Chiaramonti, 1976; Hasalova et al. , 2008) and the ultramafic upper mantle (Prouteau et al., 2001; Pilet et al., 2002). The last two papers point to the fact that felsic liquids would be able to perform certain kinds of metasomatism in the source regions of basaltic magmas, such as depletion in the high field-strength elements Ti and Ta, that would be impossible if the metasomatizing agent were an aqueous fluid. The fluid in question was inferred to be ultra-hydrous granitic liquid generated during subduction. Hill (1995) described a deep-crustal shear zone in the New Zealand Fiordland where granitic pegmatites are inferred to have been intruded at 680 °C and 1.2 GPa. Such magmas would be near-critical, especially in view of the possibility of high F and P contents. Sorensen (1983) recorded regional granitization in the deep-seated Nordre Stromfjord shear zone of West Greenland. Under these P – T conditions granitic H_2O-rich fluids would be very fluid, to

judge from quench textures in the present experiments, and capable of intimate penetration of country rocks. Hasalova et al. (2008) interpreted quartz-feldspar grain boundary assemblages in high-pressure gneisses from the Czech Republic to infer that massive metasomatism had occurred in these rocks under granulite facies conditions by percolating magmas. If this interpretation is correct, it would imply that the magmas had lower viscosity than currently supposed. Bureau and Keppler (1999) pointed out that rising supercritical silicate-H_2O mixtures must inevitably split into hydrothermal and silicate magma fractions at some level where the expanding solvus in hydrous granitic magmas overwhelms a near-critical fluid, resulting in sudden increase of viscosity of the silicate-rich fraction. This could possibly be used to explain the conspicuous localization of migmatite complexes in the middle crust (Olsen et al., 2004).

The possibility that supercritical hydrous silicate liquids may be important in interior-continent settings loses some of its appeal from the fact that many fluid inclusions in migmatites have substantial saline components, especially NaCl (Touret and Olsen, 1985). Cruz and Manning (2009) found that NaCl rapidly increases the critical temperature in the system SiO_2-H_2O, and our unpublished observations have shown marked inhibition of critical mixing in the $NaAlSi_3O_8$-H_2O system at high pressures in the presence of NaCl. From this standpoint it may appear doubtful that supercritical hydrous quartzofeldspathic liquids are commonly realized in the deep-cratonal setting.

Table 1.1

Glossary of terms

Ab	The $NaAlSi_3O_8$ *component*, as opposed to the crystalline phase of $NaAlSi_3O_8$ called albite
Critical end point	The intersection of the Ab-H_2O critical curve with the albite solubility curve
Critical curve	A line defined by the set of critical points in a binary system, here, Ab-H_2O. The curve separates a stable two-phase field an immiscible liquid and vapor with a one-phase field of supercritical fluid.
Critical point	The termination of liquid-vapor univariant curve in P-T space whereby an increase in P or T results in complete miscibility of the L + V phases giving rise to a supercritical fluid
Fluid	A liquid, vapor, or supercritical phase of unspecified composition
Vapor saturated solidus	The intersection of the liquidus at the solidus defined at a particular pressure
H_2O	The H_2O *component*, as opposed to the molecular phase of H_2O called water
Liquid	A subcritical fluid that is enriched in silicate matter and relatively dense compared to the vapor. The term is synonymous with that of melt
Liquidus	The temperature below which crystalline albite coexists with melt (aka liquid) and above which it is completely melted.
Polymerization	A polymer of silicate (Ab)-H_2O whereby polymerization occurs via oxygen bridging (Wasserberg, 1957)
Solidus	A temperature defined at a certain temperature in the binary system Ab-H_2O where the first melt appears and below which albite is crystalline.
Supercritical	The P-T-X conditions defining a supercritical state of the system (i.e. one in which the only stable phase is a supercritical fluid)
Supercritical fluid	A fluid of Ab and H_2O formed at P and T above a critical point along the critical curved
Vapor	A subcritical fluid containing dissolved albite. It is relatively more water-rich and less dense than the other subcritical fluid, the liquid. The term is synonymous with that of gas.

Table 1.2: Complete run table, excluding solubility measurements.
Note: L= liquid, V=vapor, SCF= supercritical fluid, QP= quench paragonite, xtl= Albite crystals, QH= quench hydromica

run number	P (GPa)	T (°C)	wt% H_2O	time (h)	classification
AB28	1.00	900	80.02	21	V
AB34	1.00	750	87.87	47	V
AB37	1.00	800	84.89	24	V
AB51	1.00	950	77.46	3	V
AB52	1.00	950	79.94	3	V
AB54	1.00	950	74.52	3	V
AB55	1.00	950	71.50	2	V
AB65	1.00	1020	60.16	4	V
AB76	1.00	900	78.00	22	V
AB33	1.00	850	83.22	23	V
AB03	1.00	800	13.35	24	L
AB04	1.00	800	11.40	24	L
AB06	1.00	750	12.56	19	L
AB18	1.00	750	20.00	88	L
AB26	1.00	800	22.94	68	L
AB31	1.00	750	21.72	51	L
AB32	1.00	750	20.00	51	L
AB39	1.00	850	23.95	26	L
AB40	1.00	850	25.72	26	L
AB78	1.00	950	6.49	67	L
AB235	1.00	900	7.95	42	L
AB237	1.00	850	8.73	27	L
AB64	1.00	1060	50.10	3	SCF
AB69	1.00	1060	60.02	7	SCF
AB70	1.00	1060	50.36	7	SCF
AB72	1.00	1060	39.84	26	SCF
AB19	1.00	700	46.92	75	L+V
AB20	1.00	750	23.07	68	L+V
AB21	1.00	750	35.02	68	L+V
AB22	1.00	750	75.07	72	L+V
AB27	1.00	800	26.13	68	L+V
AB29	1.00	850	27.99	23	L+V
AB30	1.00	850	30.24	23	L+V
AB35	1.00	900	74.08	21	L+V
AB38	1.00	850	79.94	23	L+V
AB41	1.00	800	81.96	44	L+V
AB42	1.00	900	78.21	50	L+V

AB43	1.00	950	68.21	72	L+V
AB44	1.00	750	86.09	74	L+V
AB45	1.00	900	29.69	19.5	L+V
AB46	1.00	900	26.05	19.5	L+V
AB47	1.00	950	71.33	22	L+V
AB48	1.00	950	73.86	22	L+V
AB49	1.00	950	32.58	22	L+V
AB50	1.00	950	33.41	3	L+V
AB53	1.00	950	31.08	2	L+V
AB56	1.00	950	50.45	3	L+V
AB57	1.00	950	27.60	2	L+V
AB58	1.00	950	67.65	1	L+V
AB59	1.00	990	39.91	2	L+V
AB60	1.00	970	40.24	2	L+V
AB61	1.00	1010	28.57	2	L+V
AB62	1.00	1000	50.27	2	L+V
AB63	1.00	1035	50.00	2	L+V
AB66	1.00	980	59.68	3	L+V
AB67	1.00	1040	40.17	7	L+V
AB71	1.00	1035	50.05	21	L+V
AB231	1.00	700	22.55	93	L+V
AB01	1.00	800	8.79	50	L+xtls
AB02	1.00	800	4.06	50	L+xtls
AB05	1.00	750	10.93	24	L+xtls
AB07	1.00	800	10.11	24	L+xtls
AB08	1.00	750	11.72	22	L+xtls
AB09	1.00	700	16.79	68	L+xtls
AB11	1.00	850	6.44	23	L+xtls
AB15	1.00	850	7.23	24	L+xtls
AB16	1.00	900	6.61	23	L+xtls
AB23	1.00	800	8.01	48	L+xtls
AB24	1.00	700	18.02	64	L+xtls
AB25	1.00	700	19.48	64	L+xtls
AB79	1.00	950	4.99	67	L+xtls
AB234	1.00	900	6.57	42	L+xtls
AB236	1.00	850	7.24	27	L+xtls
AB110	1.25	700	75.84	46	V
AB115	1.25	800	62.73	23	V
AB124	1.25	700	73.37	72	V
AB128	1.25	880	55.36	50	V
AB182	1.25	775	69.66	168	V
AB189	1.25	700	79.98	60	V
AB178	1.25	700	73.21	118	V

AB177	1.25	700	70.62	118	V
AB80	1.25	800	18.27	22.5	L
AB90	1.25	800	12.76	70	L
AB95	1.25	900	8.05	22	L
AB96	1.25	900	11.18	22	L
AB198	1.25	960	38.22	3	L
AB227	1.25	850	25.08	24	L
AB165	1.25	920	50.01	71	SCF
AB197	1.25	960	50.06	3	SCF
AB89	1.25	700	31.22	69	L+V
AB91	1.25	800	30.93	70	L+V
AB94	1.25	700	40.31	117	L+V
AB100	1.25	900	48.97	70	L+V
AB104	1.25	700	33.20	94	L+V
AB105	1.25	700	37.29	94	L+V
AB106	1.25	700	69.94	22	L+V
AB107	1.25	800	48.96	21	L+V
AB111	1.25	700	64.99	42	L+V
AB112	1.25	800	42.21	40	L+V
AB113	1.25	800	37.68	40	L+V
AB114	1.25	850	48.64	28	L+V
AB116	1.25	700	70.72	96	L+V
AB119	1.25	800	60.14	91	L+V
AB121	1.25	875	49.07	24	L+V
AB125	1.25	800	56.14	96	L+V
AB129	1.25	880	44.16	50	L+V
AB130	1.25	800	58.97	116	L+V
AB131	1.25	850	45.39	70	L+V
AB132	1.25	850	55.03	70	L+V
AB136	1.25	870	52.17	73	L+V
AB175	1.25	800	37.87	10	L+V
AB179	1.25	800	41.14	44	L+V
AB181	1.25	775	61.77	168	L+V
AB194	1.25	920	45.14	16	L+V
AB226	1.25	700	25.39	117	L+V
AB81	1.25	800	10.53	22.5	L+xtls
AB93	1.25	700	17.54	117	L+xtls
AB99	1.25	900	6.57	70	L+xtls
AB88	1.25	700	20.24	69	L+xtls
AB74	1.25	650	90.53	48	paragonite
AB142	1.40	700	60.97	99	V
AB190	1.40	750	64.09	24	V
AB193	1.40	800	54.35	176	V

AB196	1.40	700	70.08	199	V
AB157	1.40	750	57.00	96	V
AB122	1.60	700	58.06	77	V
AB147	1.40	800	13.51	45	L
AB232	1.40	800	32.22	24	L
AB233	1.40	700	29.63	23	L
AB149	1.40	900	9.12	25	L
AB133	1.40	830	50.19	98	SCF or V
AB218	1.40	860	45.22	42	SCF
AB195	1.40	750	41.80	206	L+V
AB224	1.40	800	41.02	24	L+V
AB164	1.40	815	49.62	66	L+V
AB126	1.40	750	48.99	72	L+V
AB127	1.40	800	49.37	69	L+V
AB144	1.40	700	43.67	92	L+V
AB150	1.40	700	57.83	65	L+V
AB156	1.40	750	53.35	96	L+V
AB191	1.40	750	46.02	24	L+V
AB228	1.40	700	32.12	24	L+V
AB192	1.40	800	45.05	176	L+V
AB174	1.40	665	64.84	112	V+xtls
AB137	1.40	660	69.90	70	V+xtls
AB145	1.40	660	73.02	96	V+xtls
AB143	1.40	700	19.52	92	L+xtls
AB146	1.40	800	11.44	45	L+xtls
AB148	1.40	900	7.26	25	L+xtls
AB135	1.40	700	22.59	118	L+xtls
AB151	1.60	900	9.03	18	L
AB153	1.60	800	14.1	23	L
AB160	1.60	700	25.22	81	L
AB229	1.60	670	39.06	68	L or SCF
AB185	1.60	665	65.09	46	V
AB199	1.60	665	70.16	99	V
AB200	1.60	665	65.18	99	V
AB208	1.60	665	59.41	29	V
AB155	1.60	900	7.34	24	L+xtls
AB158	1.60	800	11.88	20	L+xtls
AB159	1.60	700	21.89	81	L+xtls
AB230	1.60	670	30.62	29	L+xtls
AB161	1.60	660	49.99	93	V+xtls
AB187	1.60	650	54.53	77	V+xtls
AB188	1.60	650	59.37	77	V+xtls
AB212	1.60	665	50.72	22	V+xtls

AB213	1.60	665	56.06	22	V+xtls
AB122	1.60	700	58.06	77	SCF
AB139	1.60	690	51.47	49	SCF
AB173	1.60	710	49.98	115	SCF
AB140	1.60	690	49.9	68	SCF or L+V
AB166	1.60	680	50.01	191	SCF or L+V
AB168	1.70	900	8.95	74	SCF
AB171	1.70	800	13.50	75	SCF
AB172	1.70	665	50.01	141	SCF+QP
AB202	1.70	700	33.80	41	SCF
AB207	1.70	740	19.97	24	SCF
AB220	1.70	1050	6.40	44	SCF
AB222	1.70	665	64.96	94	SCF
AB204	1.70	650	80.12	41	SCF+QH
AB162	1.70	650	49.97	69	SCF+xtls+QP
AB163	1.70	650	35.31	69	SCF+xtls+QP
AB169	1.70	900	8.21	74	SCF+xtls
AB170	1.70	800	12.48	75	SCF+xtls
AB205	1.70	630	79.72	20	SCF+xtls
AB206	1.70	630	65.26	20	SCF+xtls+QP?
AB210	1.70	675	32.74	16	SCF+xtls
AB211	1.70	720	19.54	77	SCF+xtls+QP
AB214	1.70	650	49.88	99	SCF+xtls
AB215	1.70	650	63.78	99	SCF+xtls
AB221	1.70	1050	4.43	44	SCF+xtls

Table 1.3: Run table for albite solubility experiments. Type Ab_1 experiments were single crystal weight loss experiments, and Type Ab_2 were saturated or undersaturated experiments. Both used Amelia albite. Solubility is reported as $X_s = \Delta m_{Ab}/(\Delta m_{Ab} + m_{H2O})$ *100 where X_S is in weight percent.

Run	Type	T(°C)	P(GPa)	time (h)	m_{H2O}	error	$m_{Ab,i}$	error	$m_{Ab,f}$	error	Δm_{Ab}	error	Xs	error
AB36	Ab_1	680	1.00	72	24500	2.00	3882.3	2.00	1979.3	2.00	1903	2.00	7.208	0.001
AB82	Ab_1	680	1.00	66	30883.3	4.62	5231.04	0.17	2457.6	0.71	2773.44	1.00	8.240	0.000
AB186	Ab_1	690	1.00	91	30216.50	1.03	6552.77	0.21	2201.67	2.87	4351.10	2.87	12.587	0.001
AB102	Ab_1	670	1.25	49	33712.6	2.0	11162.8	2.0	1500.0	2.0	9662.8	2.0	22.277	0.001
AB183	Ab_1	680	1.25	315	24923.67	1.71	10950.40	0.36	3682.59	1.29	7267.81	1.33	22.577	0.000
AB174	Ab_2	665	1.40	112	6850	2	3714	2	ab	na	ab	na	35.16	-
AB180	Ab_1	665	1.40	137	37171.47	4.47	16008.40	1.26	536.87	1.60	15471.53	2.04	29.390	0.003
AB223	Ab_2	665	1.40	88	18514.20	0.82	7171.27	0.81	-	na	-	na	27.92	-
AB187	Ab_2	650	1.60	77	8084.2	0.6	6742.06	0.16	ab	na	ab	na	45.47	-
AB188	Ab_2	650	1.60	77	7456.0	1.06	5061.04	0.60	ab	na	ab	na	40.43	-
AB199	Ab_2	665	1.60	99	7532.73	0.59	3204.50	0.71	-	na	-	na	29.84	-
AB200	Ab_2	665	1.60	99	4439.66	0.99	2371.50	1.62	-	na	-	na	34.82	-
AB208	Ab_2	665	1.60	29	3962.87	1.06	2673.86	0.96	-	na	-	na	40.29	-
AB212	Ab_2	665	1.60	22	4169.6	1.3	3971.10	1.58	ab	na	ab	na	48.78	-
AB213	Ab_2	665	1.60	22	5162.60	0.53	4045.87	1.01	ab	na	ab	na	43.94	-

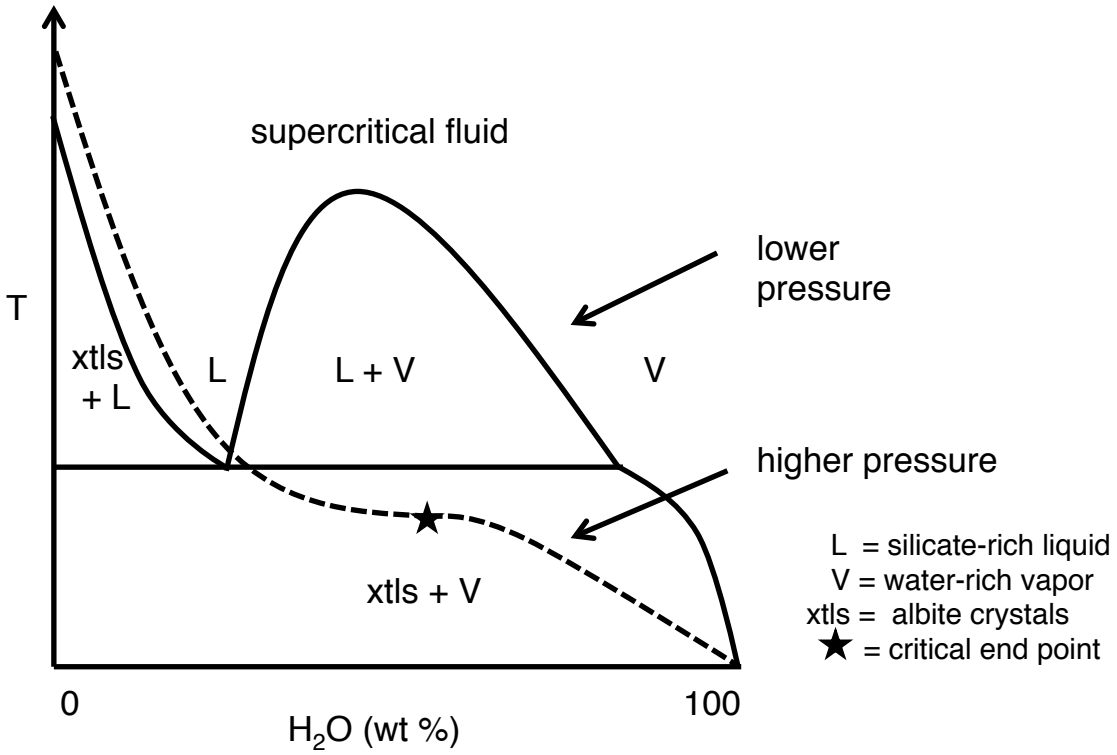

Figure 1.1: Schematic isobaric T-X_{H2O} binary in the system $NaAlSi_3O_8$-H_2O

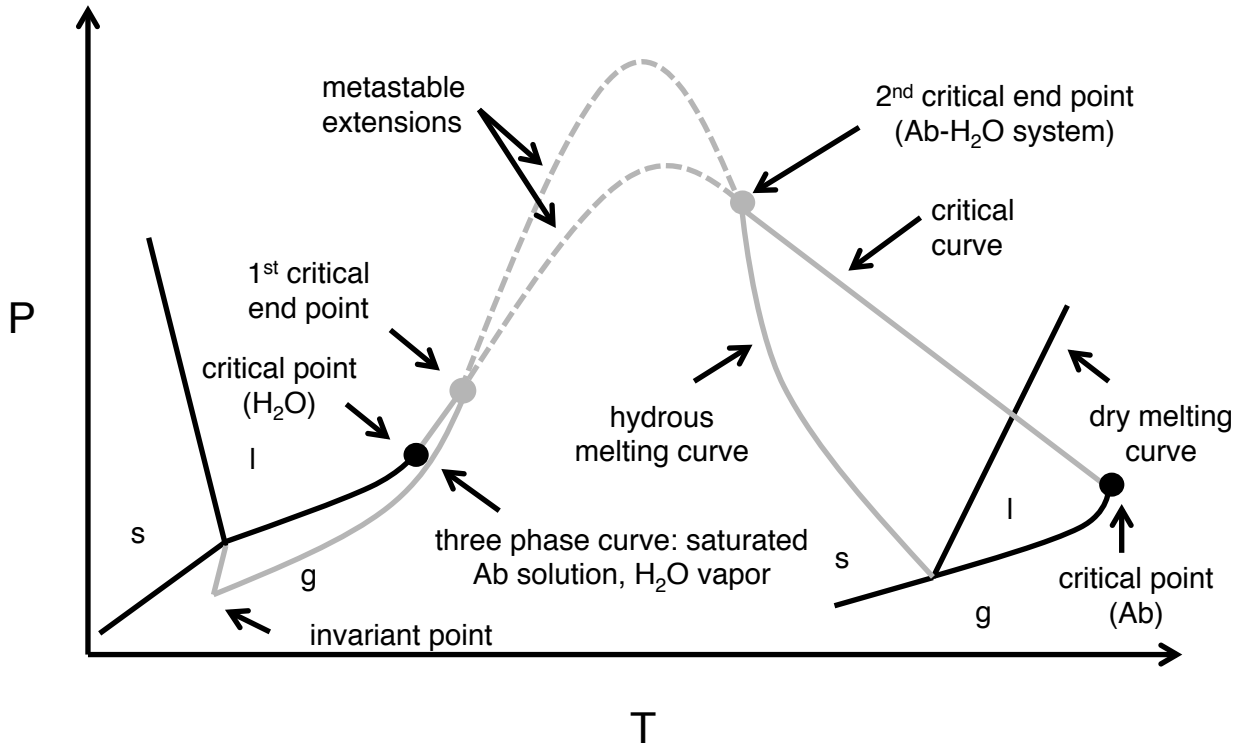

Figure 1.2: Qualitative P-T projection from composition space in the system $NaAlSi_3O_8$-H_2O. Black lines represent the pure components (left: pure water, right: pure albite), and gray lines are for the mixed system

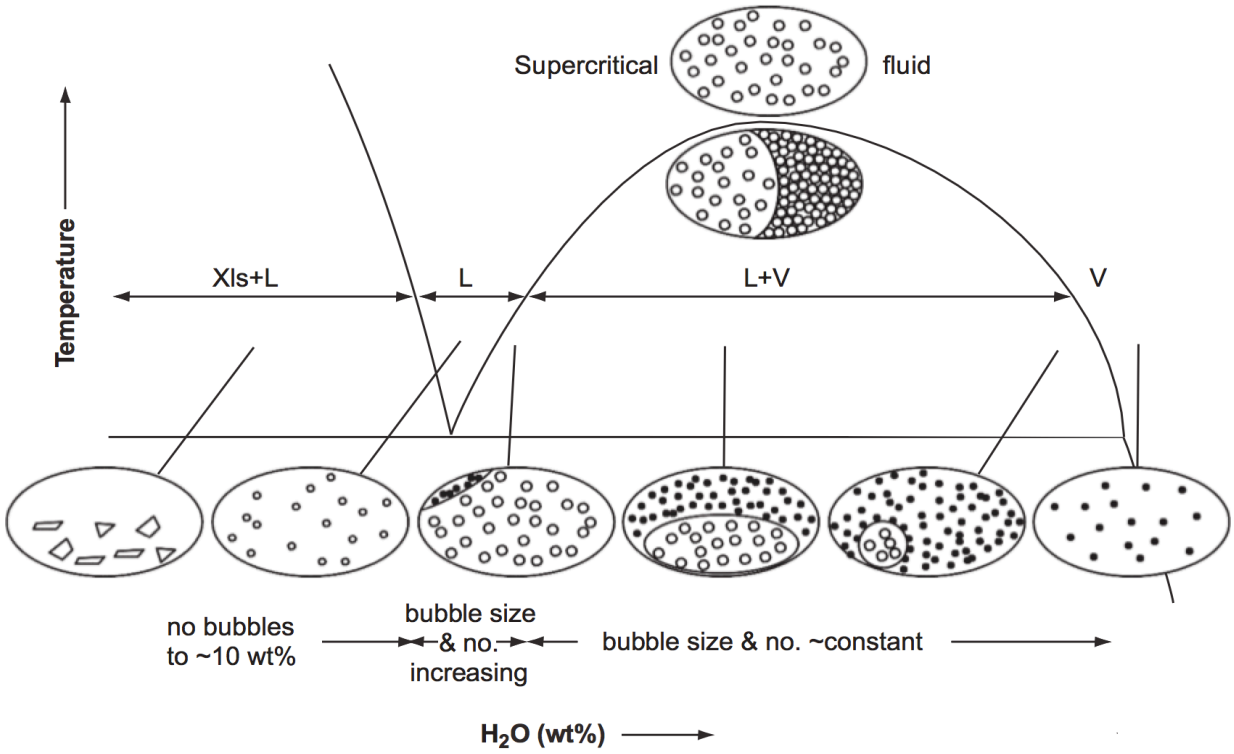

Figure 1.3: Schematic diagram depicting the textural evolution of quenched charges as increasingly more water is added the albite system. The criteria for assigning quenched charges as liquids, vapors, or supercritical fluids is discussed Section 1.2.4

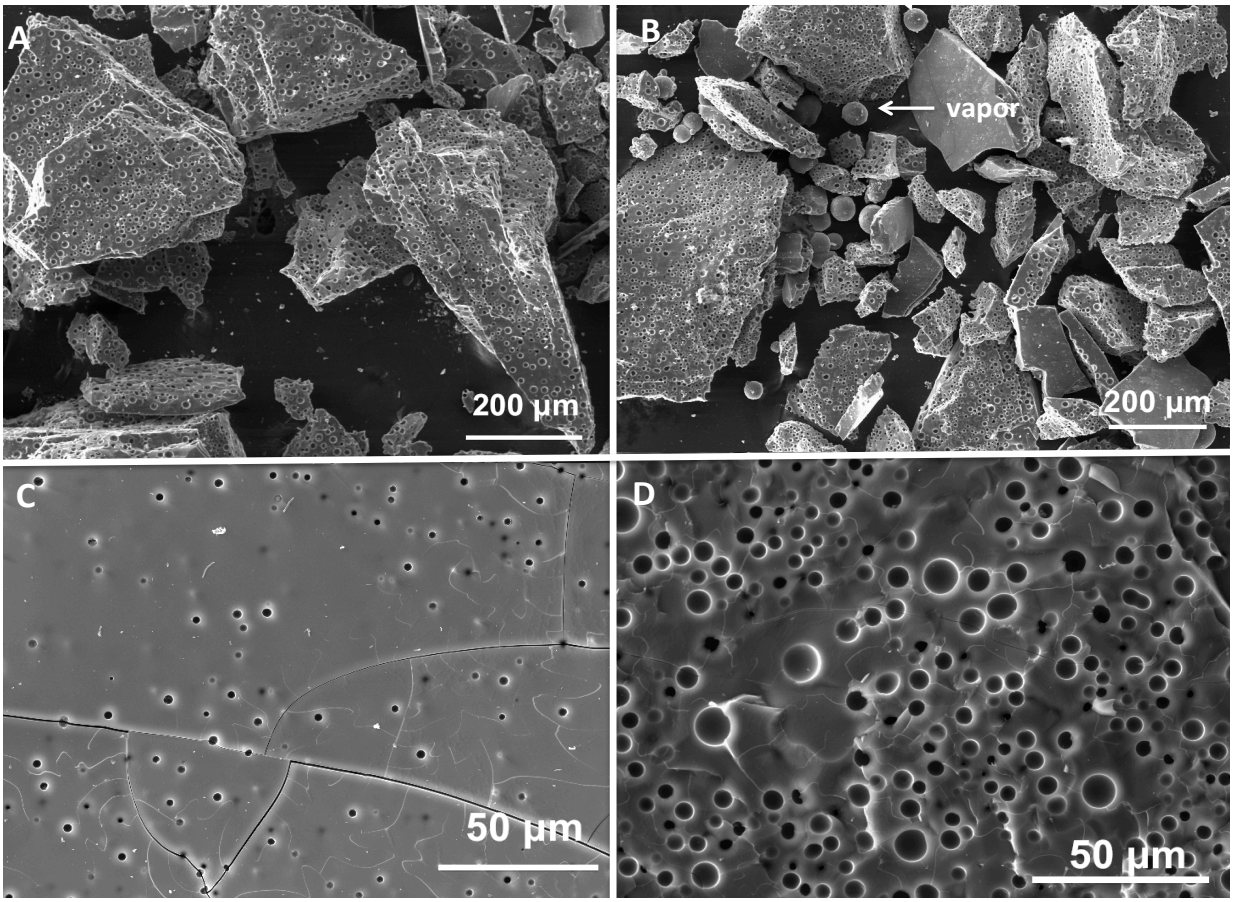

Figure 1.4: Secondary electron images of quenched charges depicting samples classified as L or L+V. **1.4A:** A liquid at high P and T quenches to a glass, with water exsolved during quenching as evidenced by bubbles trapped in the glass. Run conditions for this experiment, AB26, were 1.0 GPa, 800 °C, and 22.94 wt. % H_2O. **1.4B:** At higher water content, a fluid appears in equilibrium with the liquid phase. The fluid phase is seen here as clear glass balls that formed in a vapor space. Run conditions for this experiment, AB27, were P = 1.0 GPa, 800 °C, and 26.13 wt. % H_2O. **1.4C:** At fixed temperature and pressure, bubble size and density is markedly increased as shown by comparing Figure 1.4C to 1.4D. Run conditions for this experiment shown in 1.4C, AB03, were 1.0 GPa, 800 °C, and 13.35 wt. % H_2O. Bubble density is far lower in this experiment than for the experiment shown in Figure 1.4D **1.4D:** Run AB26, were 1.0 GPa, 800 °C, and 22.94 wt. % H_2O

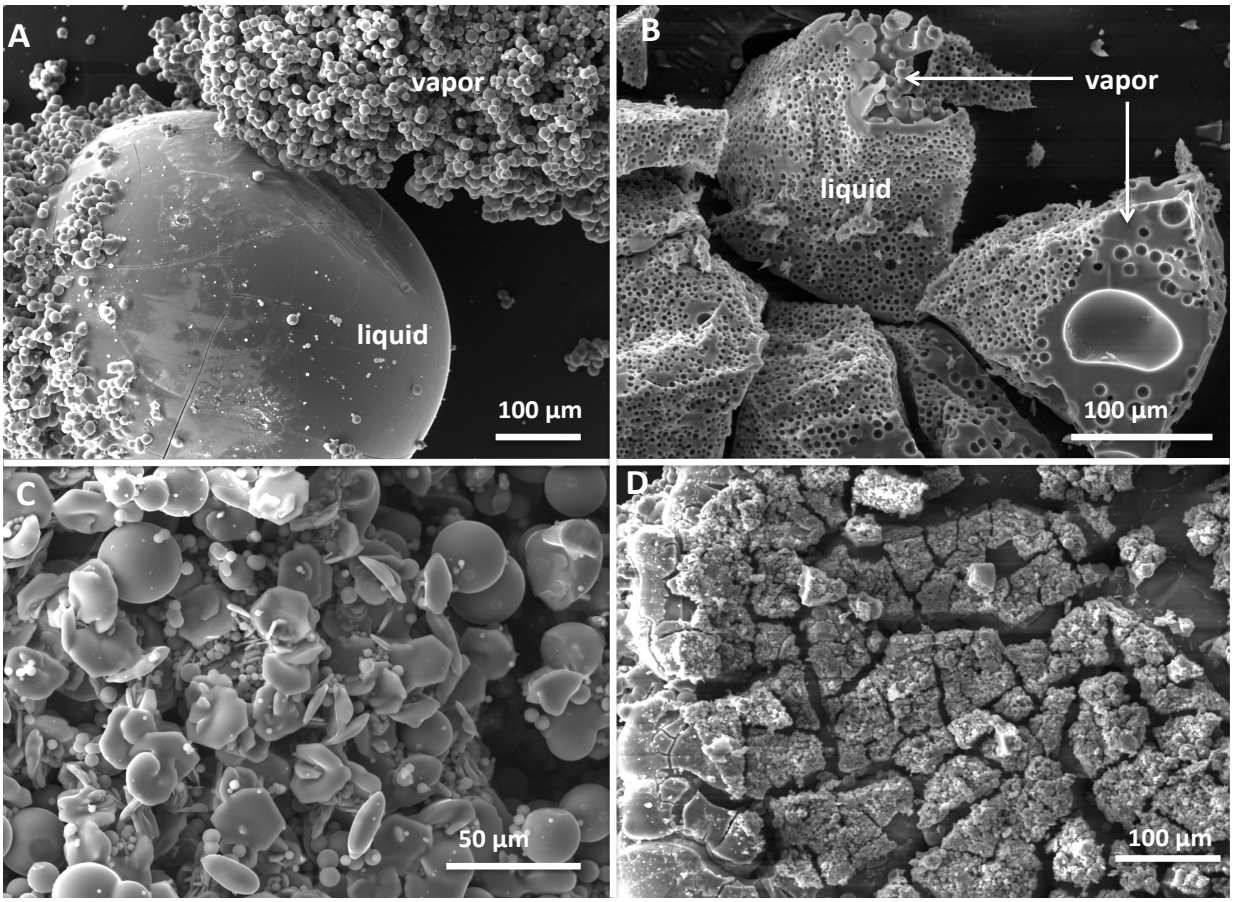

Figure 1.5: Secondary electron images of quenched charges depicting samples classified as L+V or V. **1.5A:** A porcelaneous patty or spheroid (the silicate-rich phase) is observed in charges quenched from the center of the miscibility gap, as well as at higher H_2O contents. The smaller clear balls are interpreted as quench from the coexisting water-rich phase. Run conditions for this experiment, AB35, were 1.0 GPa, 900 °C, 74.08 wt. % H_2O. **1.5B:** The quench texture criteria for a sample that was at a temperature slightly below the critical temperature can be seen here as evidenced by the interface between the two fluids. Two regions of distinctly different bubble size was observed. The two fluids seen here with distinctly different bubble characteristics show that the clear distinction between fluid and glass is diminishing and approaching a similar physical state (i.e a supercritical fluid). Run conditions for this experiment, AB164, were 1.4 GPa, 815 °C, and 49.62 wt. % H_2O. **1.5C:** A quenched vapor. Run AB37 (1.0 GPa, 800 °C, 84.89 wt. % H_2O) contains both quenched vapor and unstable quench product can be seen as tiny flakes of hexagonal crystals. This quench product is probable paragonite or hydromica. **1.5D:** Another example of a quenched fluid. The quenched fluid phase is a welded mass of balls. The crack pattern forms during the experiment after it has been quenched. Run AB28 (1.0 GPa, 900 °C, 80.02 wt. % H_2O)

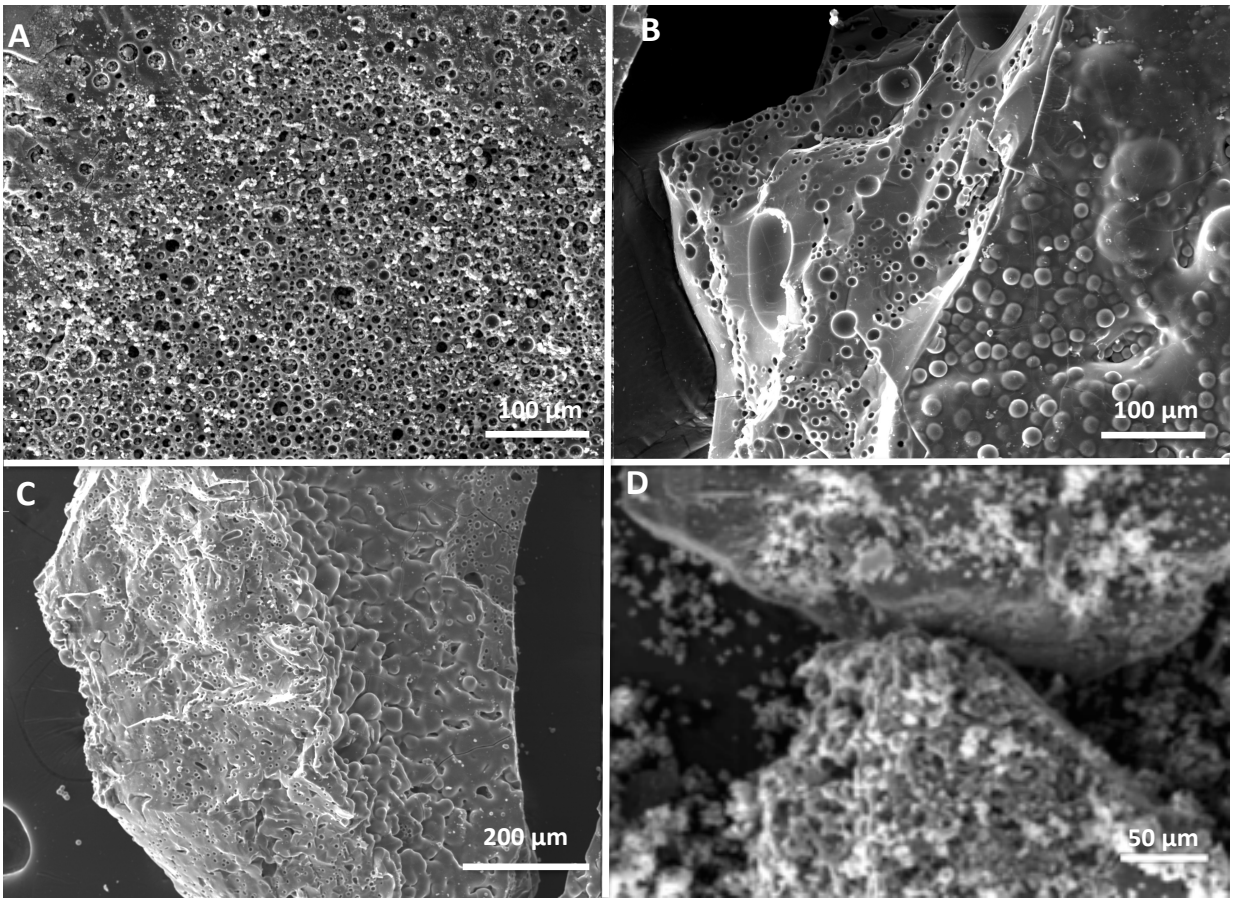

Figures 1.6: All images are of quenched supercritical fluids. They are shown in comparison to highlight the probable depolymerization of the supercritical fluid as pressure increases from 1.00 to 1.70 GPa. **1.6A:** Run AB70 (1.00 GPa, 1060 °C, 50.4 wt. % H_2O). **1.6B:** Run AB165 (1.25 GPa, 920 °C, 49.0 wt. % H_2O). **1.6C:** Run AB133 (1.40 GPa, 830 °C, 50.2 wt. % H_2O) **1.6D:** Run AB162, (1.70 GPa, 650 °C, 50.0 wt. % H_2O). The experiment conducted at 650 °C and 1.70 GPa, AB162, showed a few very large, limpid albite crystals. The albite in a similar experiment, AB163, was identified by X-ray diffraction and gave $\Delta(131)$ index of 1.06° 2θ, showing that, though completely recrystallized from the starting material, it is a maximally low-structured-state albite. The supercritical fluid is shown to be a potent fluxing agent for crystal growth of highly ordered albite.

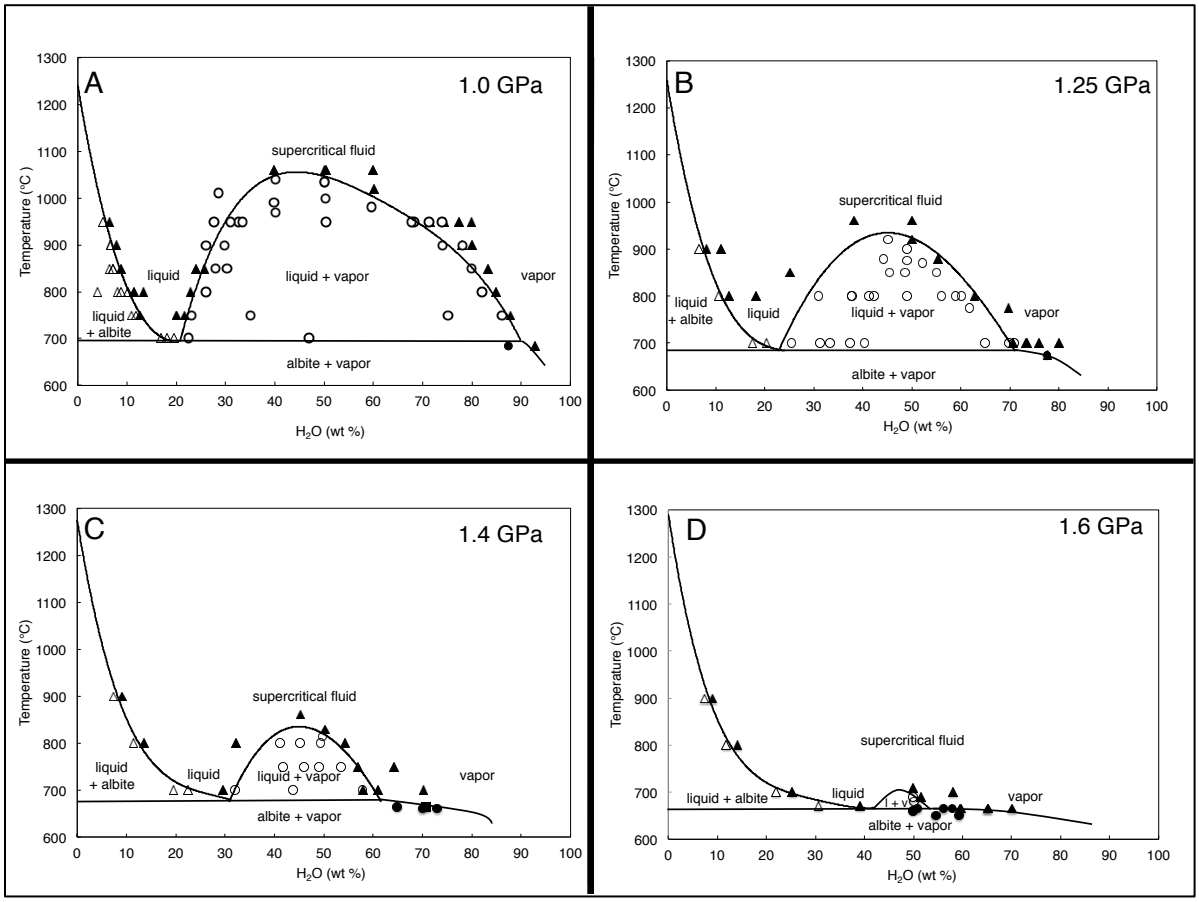

Figures 1.7 (A-D): T-X_{H2O} binary at 1.0, 1.25, 1.4 and 1.6 GPa in the system $NaAlSi_3O_8$-H_2O. The solvus curves for A-C were calculated using the model presented in section 1.4.5. The solvus in Figure 1.7D was drawn in. There is close agreement of the calculated curves with the brackets determined using the textural analysis methods presented here

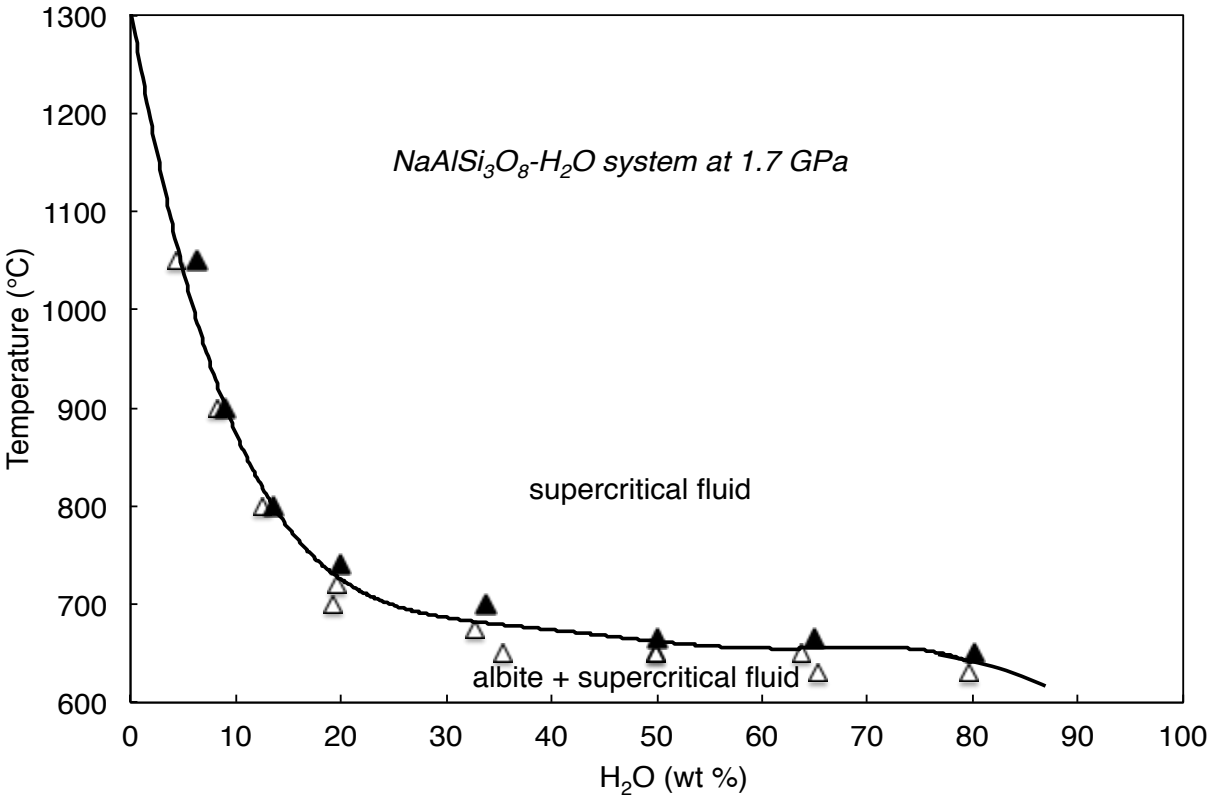

Figure 1.8: T-X_{H2O} binary at 1.7 GPa in the system $NaAlSi_3O_8$-H_2O. The results of this isobar show that albite is stable below 650 °C at 1.7 GPa. The intersection of the vapor-saturated solidus with the critical curve occurs between 1.6-1.7 GPa and at a temperature of 665±15 °C commencing with a stable critical end point in the system $NaAlSi_3O_8$-H_2O

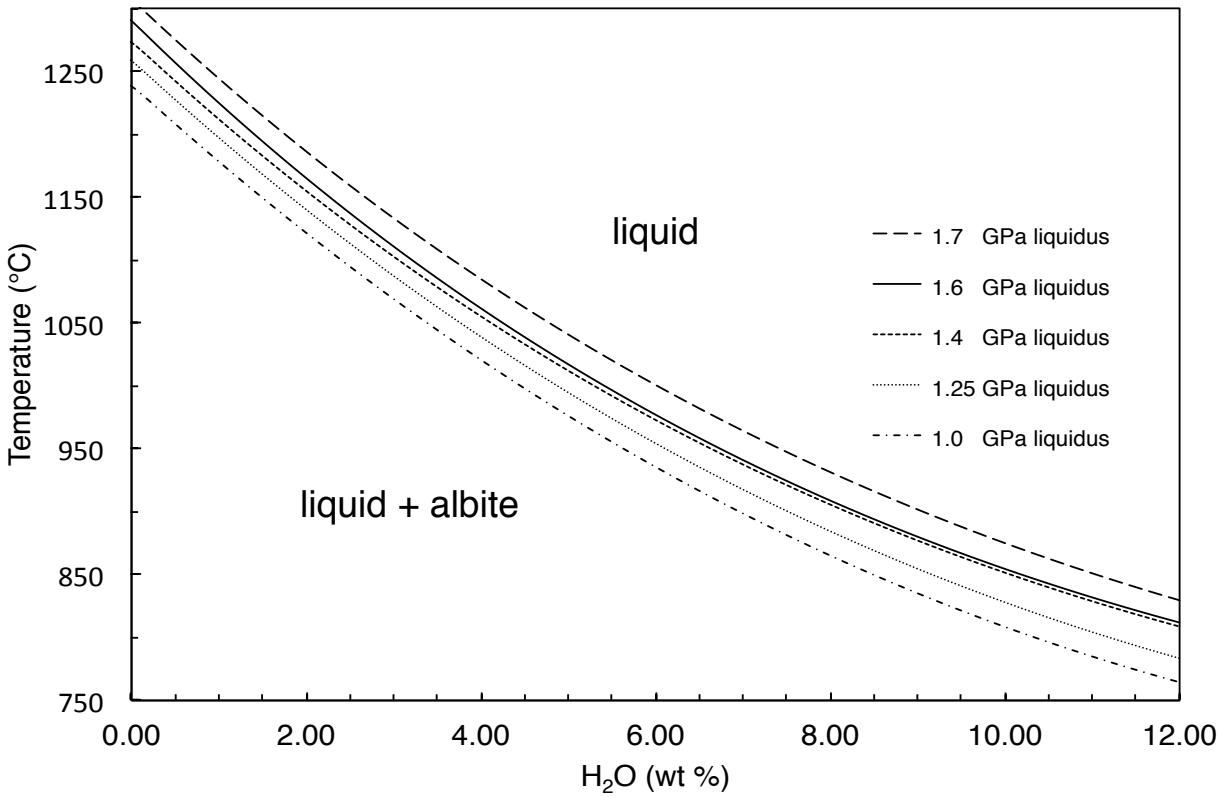

Figure 1.9: Collection of smoothed experimental liquidus H_2O curves. The H_2O-free intercept values are from Boyd and England (1963). Brackets constraining the liquidus curves are seen in Figure 1.7 and listed in Table 1.2

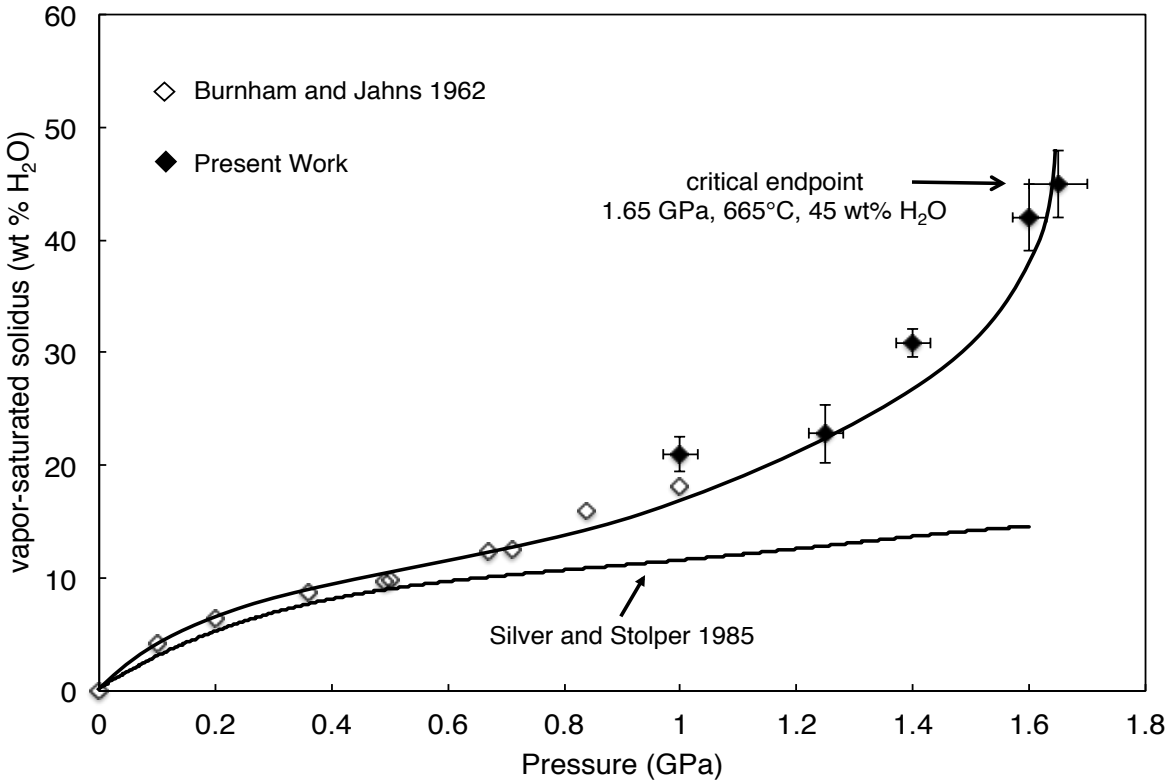

Figure 1.10: H_2O content at the solidus, that is, the H_2O content required for minimum melting at each pressure investigated. Burnham and Jahns (1962) results at lower pressure is an excellent match to the determined values at higher pressure from this study.

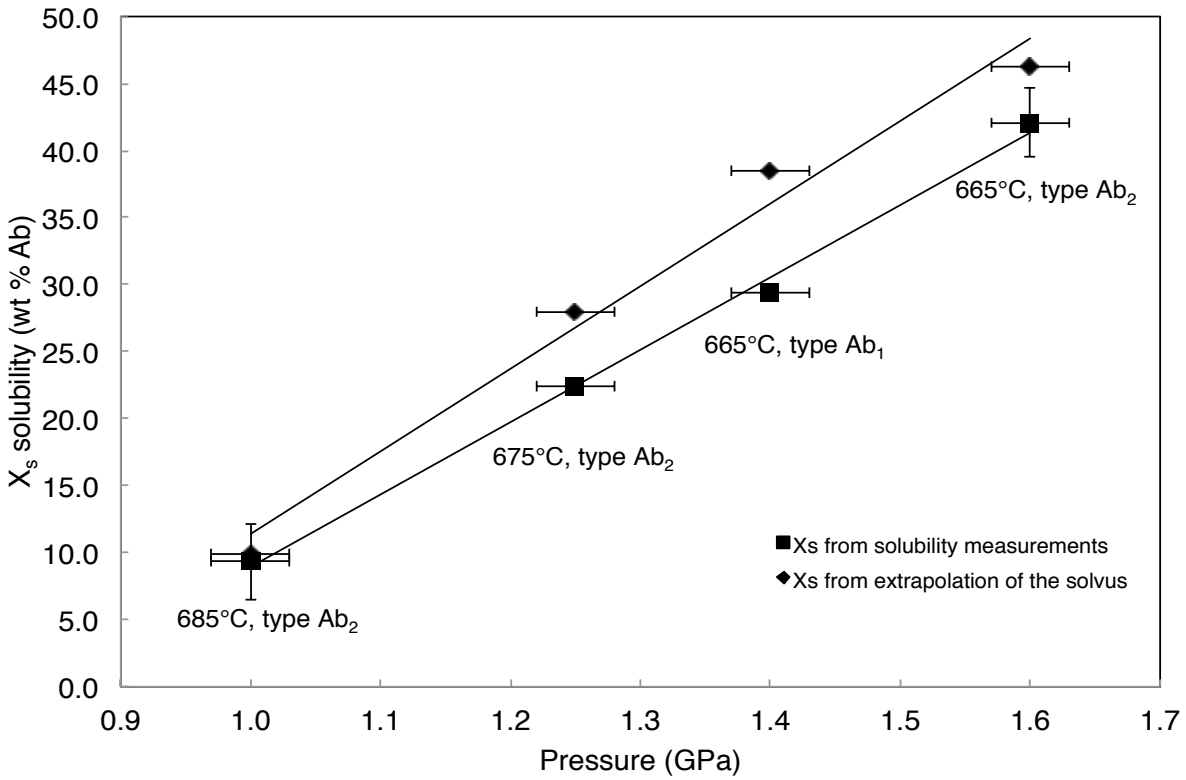

Figure 1.11: Solubility measurements of albite in H_2O, immediately below the solidus temperature based on two different methods, Ab_1 and Ab_2, compared to extrapolation to the solidus temperature of the trends of the H_2O-rich solvus limbs as inferred by quench-textures. Method Ab_1 is direct weight loss measurements on Amelia albite single crystals equilibrated with weighed amounts of H_2O. Method $Ab_2$is bracketing based on the presence or absence of albite crystals among quench products, as seen under the polarizing microscope. There is consistent discrepancy with the solvus extrapolation measurement 4-10 wt% Ab higher solubility

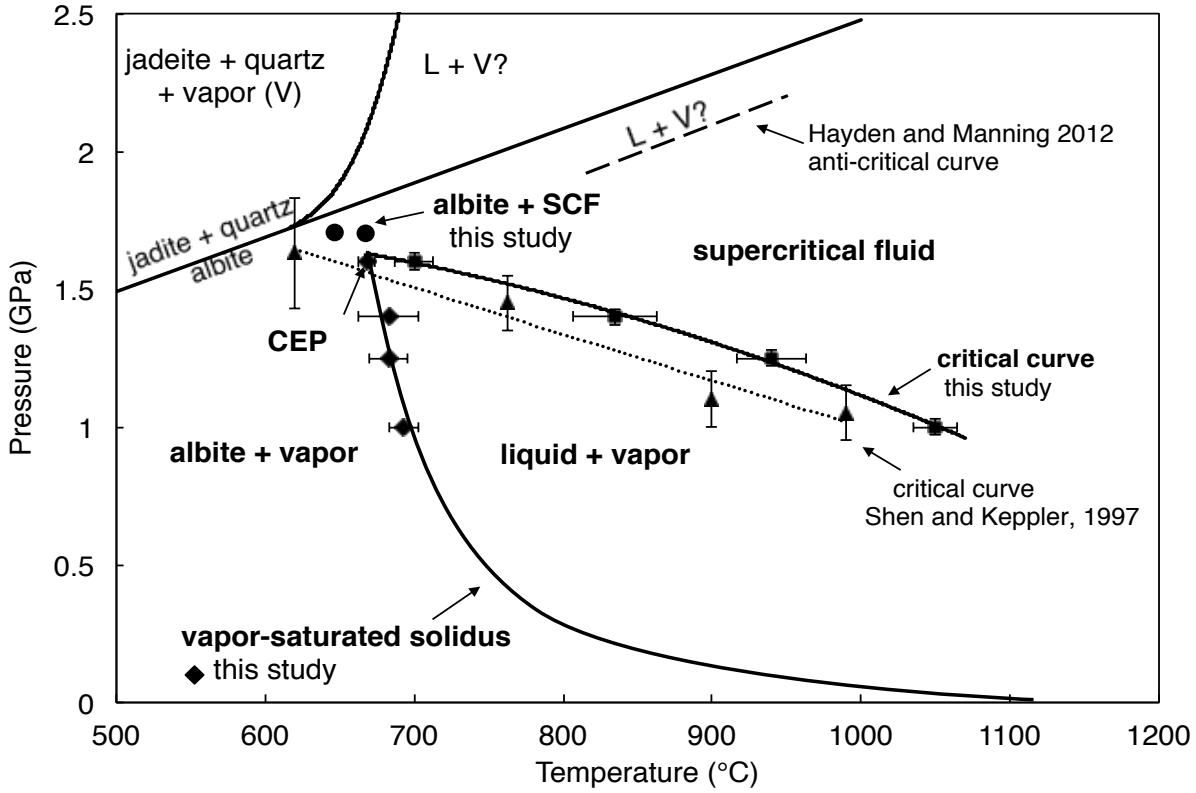

Figure 1.12: Comparison with previous experimental work. Revised P-T plot for albite-jadite-quartz and albite-water showing a stable critical end point in the system albite ($NaAlSi_3O_8$)-H_2O.
(CEP = critical end point, SCF= supercritical fluid)

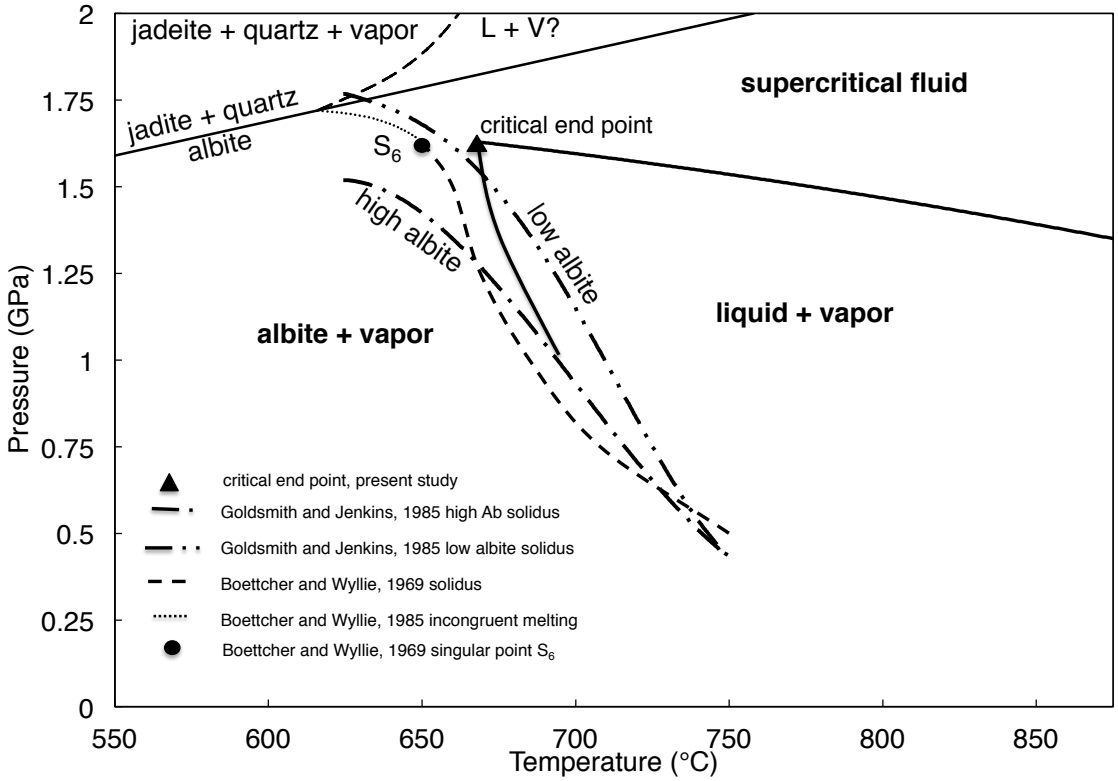

Figure 1.13: Comparison with previous experimental work. Present vapor saturated melting curve and critical curve shown as bold solid lines. The intersection coincides with the melting curve of low structural state albite according to Goldsmith and Jenkins (1985) and indicates the existence of an equilibrium critical end point. The singular point S_6 of Boettcher and Wyllie (1969) is reinterpreted as our critical end point, supporting the conjecture of Paillat et al. (1992). A two-fluid field adjacent to melting on the join $NaAlSi_3O_8$-H_2O reemerges at some higher pressure according to Hayden and Manning (2011). Melting relations near the albite→ jadite + quartz curve remain uncertain.

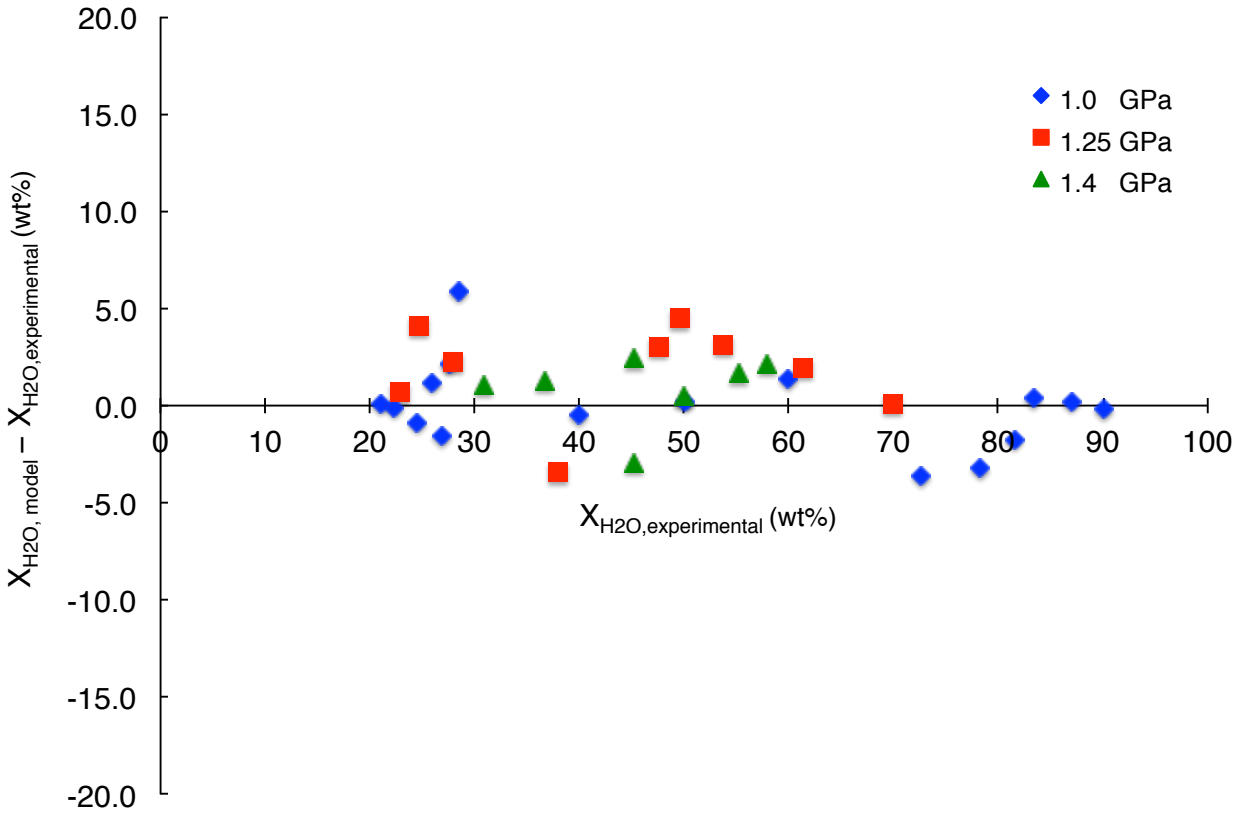

Figure 1.14: Deviations of midpoints of equilibrated brackets of the isobaric solvus curves from the model curves according to Equations 1.2-1.9 in the text. 78.1% of the data points to within ± 3 wt% H_2O and nearly randomly distributed, with the possible exception of the 1.25 GPa data, which may show that the model systematically overestimates the solvus width.

References

Alberti, A. A., and Comin-Chiaramonti, P. (1976). The metamorphic evolution of Tromöy (arendal area-South Norway). *Tschermaks mineralogische und petrographische Mitteilungen*, *23*(3), 205-220.

Anderson, G. M., and Burnham, C. W. (1967). Reactions of quartz and corundum with aqueous chloride and hydroxide solutions at high temperatures and pressures. *American Journal of Science*, ***265***(1), 12-27.

Anderson, G. M., and Burnham, C. W. (1983). Feldspar solubility and the transport of aluminum under metamorphic conditions. *American Journal of Science*, ***283***, 283-297.

Aranovich, L. Y., Shmupovich, K. I., and Fed'kin, V. V. (1987). The H_2O and CO_2 regime in regional metamorphism. *International Geology Review*, ***29***(12), 1379-1401.

Bebout, G. E., and Barton, M. D. (1993). Metasomatism during subduction: products and possible paths in the Catalina Schist, California. *Chemical Geology*, ***108***(1), 61-92.

Blencoe, J. G. (1992). A two-parameter Margules method for modeling the thermodynamic mixing properties of albite-water melts. *Transactions of the Royal Society of Edinburgh: Earth Sciences*, ***83***(1-2), 423-428.

Boettcher, A. L., and Wyllie, P. J. (1969). Phase relationships in the system $NaAlSiO_4$-SiO_2-H_2O to 35 kilobars pressure. *American Journal of Science*, ***267***, 875-909.

Bohlen, S. R., Boettcher, A. L., and Wall, V. J. (1982). The system albite-H_2O-CO_2: a model for melting and activities of water at high pressures. *American Mineralogist*, ***67***, 451-462.

Boyd, F. R., and England, J. L. (1963). Effect of pressure on the melting of diopside, $CaMgSi_2O_6$, and albite, $NaAlSi_3O_8$, in the range up to 50 kilobars. *Journal of Geophysical Research*, ***68***, 311-323.

Brown, G. C., and Fyfe, W. S. (1970). The production of granitic melts during ultrametamorphism. *Contributions to Mineralogy and Petrology*, ***28(***4), 310-318.

Bureau, H., and Keppler, H. (1999). Complete miscibility between silicate melts and hydrous fluids in the upper mantle: experimental evidence and geochemical implications. *Earth and Planetary Science Letters*, ***165***(2), 187-196.

Burnham, C. W. (1975). Water and magmas; a mixing model. *Geochimica et Cosmochimica Acta*, ***39***, 1077-1084.

Burnham, C. W. (1979). The importance of volatile constituents. In The evolution of the igneous rocks (pp. 439-482). Academic Press London.

Burnham, C. W., and Davis, N. F. (1974). The role of H 2 O in silicate melts; II, Thermodynamic and phase relations in the system $NaAlSi_3O_8$-H_2O to 10 kilobars, 700 degrees to 1100 degrees C. *American Journal of Science*, ***274***, 902-940.

Burnham, C. W., and Jahns, R. H. (1962). A method for determining the solubility of water in silicate melts. *American Journal of Science*, ***260***, 721-745.

Cruz, M. F., Manning, C. E., Newton, R. C., amd Hunt, J. D. (2009). The effect of NaCl on aqueous silica in mantle fluids: constraints from quartz solubility experiments in NaCl-H_2O at 1000 °C, 1.5 GPa. In *AGU Fall Meeting Abstracts* ***1*** (pp. 2226).

Currie, K. L. (1968). On the solubility of albite in supercritical water in the range of 400 to 600 °C and 750 to 3500 bars. *American Journal of Science*, *266*(5), 321-341.

Eggler, D. H., and Kadik, A. A. (1979). The system $NaAlSi_3O_8$-H_2O-CO_2 to 20 kbar pressure: I. Compositional and thermodynamic relations of liquids and vapors coexisting with albite. *American Mineralogist*, ***64***, 1036-1048.

Goldsmith, J. R., and Jenkins, D. M. (1985). The high-low albite relations revealed by reversal of degree of order at high pressures. *American Mineralogist*, ***70***(9-10), 911-923.

Goldsmith, J. R., and Jenkins, D. M. (1985). The hydrothermal melting of low and high albite. *American Mineralogist*, ***70***(9-10), 924-933.

Goranson, R. (1938). Silicate-water systems: phase equilibria in the $NaAlSi_3O_8$—H_2O and $KAlSi_3O_8$-H_2O systems at high temperatures and pressures. *American Journal of Science*, 71-91.

Green, D. H., and Wallace, M. E. (1988) Mantle metasomatism by ephemeral carbonatite melts. *Nature* **336**, 459-462.

Hack, A. C., Hermann, J., and Mavrogenes, J. A. (2007). Mineral solubility and hydrous melting relations in the deep earth: Analysis of some binary A–H_2O system pressure-temperature-composition topologies. *American Journal of Science*, ***307***, 833-855.

Hamilton, D. L., and Oxtoby, S. (1986). Solubility of water in albite-melt determined by the weight-loss method. *The Journal of Geology*, 626-630.

Hasalová, P., Janoušek, V., Schulmann, K., Štípská, P., and Erban, V. (2008). From orthogneiss to migmatite: geochemical assessment of the melt infiltration model in the Gföhl Unit (Moldanubian Zone, Bohemian Massif). *Lithos*, ***102***(3), 508-537.

Hayden, L. A., and Manning, C. E. (2011). Rutile solubility in supercritical $NaAlSi_3O_8$-H_2O fluids. *Chemical Geology*, ***284***, 74-81.

Heier, K. S. (1973). Geochemistry of granulite facies rocks and problems of their origin. *Philosophical Transactions of the Royal Society of London. Series A, Mathematical and Physical Sciences*, ***273***(1235), 429-442.

Hill, E. J. (1995). A deep crustal shear zone exposed in western Fiordland, New Zealand. *Tectonics*, ***14*****(**5), 1172-1181.

Hunt, J. D., and Manning, C. E. (2012). A thermodynamic model for the system SiO_2–H_2O near the upper critical end point based on quartz solubility experiments at 500–1100° C and 5–20 kbar. *Geochimica et Cosmochimica Acta*, ***86*****,** 196-213.

Holland, T. J. B., and Powell, R. (1998). An internally consistent thermodynamic data set for phases of petrological interest. *Journal of Metamorphic Geology*, ***16*****,** 309-343.

Jayananda, M., Martin, H., Peucat, J. J., and Mahabaleswar, B. (1995). Late Archaean crust-mantle interactions: geochemistry of LREE-enriched mantle derived magmas. Example of the Closepet batholith, southern India. *Contributions to Mineralogy and Petrology*, ***119***(2-3), 314-329.

Johannes, W., and Holtz, F. (1991). Formation and ascent of granitic magmas. *Geologische Rundschau*, ***80***(2), 225-231.

Kennedy, G. C., Wasserburg, G. J., Heard, H. C., and Newton, R. C. (1962). The upper three-phase region in the system SiO_2-H_2O. *American Journal of Science*, ***260***(7), 501-521.

Knapp, W. J., and Vorst, W. (1959). Activities and Structure of Some Melts in the System Na_2SiO_3-$Na_2Si_2O_5$. *Journal of the American Ceramic Society*, ***42***, 559-562.

Litvinovsky, B. A., and Podladchikov, Y. Yu. (1993). Crustal anatexis during the influx of mantle volatiles: *Lithos*, ***30***, 93-107.

Luth, W. C. (1976). Granitic rocks. In The evolution of the crystalline rocks (pp. 335-419). Academic Press London.

Manning, C. E. (1994) The solubility of quartz in H_2O in the lower crust and upper mantle. *Geochimica et Cosmochimica Acta*, ***58***, 4831-4839.

Manning, C. E. (2004). The chemistry of subduction-zone fluids. *Earth and Planetary Science Letters*, ***223***, 1-16.

Manning, C. E., and Boettcher, S. L. (1994). Rapid-quench hydrothermal experiments at mantle pressures and temperatures. *American Mineralogist*, ***79***(11), 1153-1158.

McLelland, J., Morrison, J., Selleck, B., Cunningham, B., Olson, C., and Schmidt, K. (2002). Hydrothermal alteration of late‐to post‐tectonic Lyon Mountain Granitic Gneiss, Adirondack Mountains, New York: Origin of quartz–sillimanite segregations, quartz–albite lithologies, and associated Kiruna‐type low‐Ti Fe‐oxide deposits. *Journal of Metamorphic Geology*, ***20***(1), 175-190.

McMillan, P. F., & Holloway, J. R. (1987). Water solubility in aluminosilicate melts. *Conributions to Mineralogy and Petrology*, ***97***(3), 320-332.

Newton, R. C., and Smith, J. V. (1967) Investigations concerning the breakdown of albite at depth in the earth. *The Journal of Geology*, ***75***, 268-286.

Newton, R. C., and Manning, C. E. (2008). Thermodynamics of SiO_2–H_2O fluid near the upper critical end point from quartz solubility measurements at 10 kbar. *Earth and Planetary Science Letters*, ***274***(1), 241-249.

Olsen, S. N., Marsh, B. D., and Baumgartner, L. P. (2004). Modelling mid-crustal migmatite terrains as feeder zones for granite plutons: the competing dynamics of melt transfer by bulk versus porous flow. *Transactions of the Royal Society of Edinburgh: Earth Sciences*, ***95***(1-2), 49-58.

Paillat, O., Elphick, S. C., and Brown, W. L. (1992). The solubility of water in NaAlSi3O8 melts: a re-examination of Ab− H2O phase relationships and critical behaviour at high pressures. *Contributions to Mineralogy and Petrology*, ***112***(4), 490-500.

Pilet, S., Hernandez, J., and Villemant, B. (2002). Evidence for high silicic melt circulation and metasomatic events in the mantle beneath alkaline provinces: the Na–Fe-augitic green-core pyroxenes in the Tertiary alkali basalts of the Cantal massif (French Massif Central). *Mineralogy and Petrology*, ***76***(1-2), 39-62.

Prouteau, G., Scaillet, B., Pichavant, M., and Maury, R. (2001). Evidence for mantle metasomatism by hydrous silicic melts derived from subducted oceanic crust. *Nature*, ***410***(6825), 197-200.

Ribbe, P. H., and Smith, J. V. (1966). X-ray-emission microanalysis of rock-forming minerals IV. Plagioclase feldspars. *The Journal of Geology*, ***74***, 217-233.

Sawyer, E. W. (1994). Melt segregation in the continental crust. *Geology*, ***22***(11), 1019-1022.

Shen, A. H., and Keppler, H. (1997). Direct observation of complete miscibility in the albite–H2O system. *Nature*, ***385***, 710-712.

Silver, L., and Stolper, E. (1985). A thermodynamic model for hydrous silicate melts. *The Journal of Geology*, ***93***(2), 161-177.

Spear, F. S. (1995). *Metamorphic phase equilibria and pressure-temperature-time paths* (p. 799). Washington: Mineralogical Society of America.

Stadler, R., Ulmer, P., Thompson, A. B., and Gunther, D. (2000). Experimental approach to constrain second critical end points in fluid/silicate systems: near-solidus fluids and melts in the system albite-H_2O. *American Mineralogist*, ***85***, 68-77.

Stevens, G., and Clemens, J. D. (1993). Fluid-absent melting and the roles of fluids in the lithosphere: a slanted summary?. *Chemical Geology*, ***108***(1), 1-17.

Sørensen, K. (1983). Growth and dynamics of the Nordre Strømfjord shear zone. *Journal of Geophysical Research: Solid Earth (1978–2012)*, ***88***(B4), 3419-3437.

Thompson Jr, J. B. (1967). Thermodynamic properties of simple solutions. *Researches in geochemistry*, ***2***, 340-361.

Touret, J., and Olsen, S. N. (1985). Fluid inclusions in migmatites. In *Migmatites* (pp. 265-288). Springer US.

Webster, J. D., Kinzler, R. J., and Mathez, E. A. (1999). Chloride and water solubility in basalt and andesite melts and implications for magmatic degassing. *Geochimica et Cosmochimica Acta*, ***63***(5), 729-738.

Wickham, S. M., and Taylor Jr, H. P. (1987). Stable isotope constraints on the origin and depth of penetration of hydrothermal fluids associated with Hercynian regional metamorphism and crustal anatexis in the Pyrenees. *Contributions to mineralogy and petrology*, ***95***(3), 255-268.

Wohlers, A., Manning, C. E., and Thompson, A. B. (2011). Experimental investigation of the solubility of albite and jadeite in H_2O, with paragonite + quartz at 500 and 600 ^oC, and 1–2.25 GPa. *Geochimica et Cosmochimica Acta*, ***75***(10), 2924-2939.

CHAPTER 2

Experimental determination of liquidus H_2O contents of simple granites at deep crustal conditions: 1.0 GPa and 625-1050 °C

Abstract

The liquidus water content of a granitic melt at high pressure (P) and temperature (T) is important because it constrains the volume of granite that could be produced by dehydration melting of the deep crust and it strongly influences physical properties that control the ability of granitic liquids to accumulate and ascend. Experimental determinations of the liquidus H_2O content at deep crustal P and T (625-1050˚C, 0.6-1.5 GPa) have not been previously made. Estimates have required extrapolation based on melting experiments at low P (≤ 0.5 GPa) and show substantial scatter. To improve the high-P constraints on water concentration at the granite liquidus, we performed experiments in a piston-cylinder apparatus at 1.0 GPa using a range of granite compositions. In each experiment, granite glass + H_2O was homogenized well above the liquidus T, then T was lowered until quartz and alkali feldspar crystalized from the liquid. To establish the reversed equilibrium, we crystallized the homogenized melt at the lower T, and then raised the T in stages until we found that the crystalline phases were entirely resorbed into the liquid. Four different bulk compositions were studied (Ab-Or-Qz, in wt%): 40-40-20, 37.5-37.5-25, 36.25-36.25-27.5, 35-35-30 (Note: Ab, Or and Qz refer to molecular formulas of components and not to mineral phases). Quenched charges were analyzed by petrographic microscope, scanning electron microscope (SEM), X-ray diffraction (XRD) and electron microprobe (EMP). Microprobe analysis of all-glass charges reproduced our intended starting compositions.

The first crystallization products produced from homogenized glass in several hour runs were skeletal β-quartz and spectacular large alkali feldspars with highly anomalous compositions, some having nearly the composition of the starting granitic liquid with up to 75 wt% SiO_2. After several tens to a few hundred hours at the same P-T conditions, the optically homogeneous feldspars exsolved to fine-grained granophyric intergrowths resembling some that have been described from volcanic and impactite surge deposits. Upon raising the temperature at constant pressure, these metastable undercooled feldspars were resorbed by the liquid, giving way to a new generation of alkali feldspars of normal composition (SiO_2 ~ 66 wt%) and larger quartz crystals. In a fourth heating step, all crystals were resorbed into the liquid. The temperatures of the third and fourth steps were taken as bracketing the liquidus temperature at that H_2O content.

The minimum temperature of the 1.0 GPa liquidus at a given water content occurs near 27.5 wt% Qz, regardless of H_2O content. The reversed liquidus temperatures at 2.97, 4.15, 5.82, 7.92, and 12.00 wt% water are, respectively, 935-985, 875-900, 800-825, 750-775, and 650-675 ˚C. Our results plot on the high end of the extrapolated water contents at the liquidus when compared to all other previous determinations, and, as a result, give significantly higher water contents than used by most dehydration melting models. A cubic fit to the reversed liquidus brackets for haplogranite composition $Ab_{36.25}Or_{36.25}Qz_{27.50}$ at 1.0 GPa yielded

2.1. $$T(x_{H_2O}) = -0.0784x_{H_2O}^3 + 4.2886\, x_{H_2O}^2 - 81.851\, x_{H_2O} + 1167\ ^\circ C$$

where x_{H_2O} is H_2O concentration in wt%.

The high liquidus H_2O content presents a challenge for producing voluminous amounts of metaluminous granites from lower crustal biotite-amphibole gneisses by dehydration melting. A deep-crustal tonalitic gneiss with 0.6-0.8 wt% H_2O undergoing melting at 1.0 GPa and 900 ^oC

would yield less than 20 volume percent granitic liquid for complete dehydration and perfect extractability, neither of which are likely to be realized in deep crustal melting.

2.1 Introduction

2.1.1 Importance of H_2O

A new era of understanding of how granites are formed arrived with the demonstration by Goranson (1938) that H_2O at elevated pressures dramatically lowers the melting point of albite. It was immediately clear that large-scale melting to form granitic magmas can result if ordinary feldspar-rich rocks undergoing high-grade metamorphism in the middle or deep crust are exposed to an aqueous pore-space fluid. Tuttle and Bowen (1958) carried this concept forward with their hydrous melting experiments in the simple granite system $NaAlSi_3O_8$ (Ab)-$KAlSi_3O_8$ (Or)-SiO_2 (Qz). The "Granite Memoir" gave rise to the concept of "ultrametamorphism" (Brown and Fyfe, 1970), wherein granite batholiths are regarded as the high-grade culmination of regional metamorphism.

Experimental determination of melting in simple granite systems was initially concerned with defining the minimum or eutectic as a function of pressure in the H_2O-saturated system (Burnham and Jahns, 1962; Luth et al., 1964; Seck, 1971). The pioneering Luth et al. (1964) study showed that the H_2O-saturated melting minimum in the Ab-Or-Qz system could be traced to pressures of at least 1.0 GPa. They demonstrated that over this pressure increase there is a dramatic decrease in melting temperature from >950 °C at one bar to 635 °C at 1.0 GPa, and that the H_2O concentration in the minimum or eutectic melt contains increases from 0 to >15 wt%. Boettcher and Wyllie (1968) found that a H_2O-saturated granite continues to have a eutectic melting curve to pressures of 3.0 GPa, where the high pressure minerals jadeite ($NaAlSi_2O_6$ and

coesite (SiO_2) are stable at the solidus. The advent of these dense phases causes a dramatic change from negative to positive of the dP/dT slope of the melting curve at about 1.7 GPa.

Recognition of the importance of H_2O in the generation of granitic magmas has led to much discussion of possible genetic processes. Much of it is centered around how H_2O is supplied to the site of melting in the deep crust or upper mantle, whether source rocks likely to make up most of the lower continental crust, namely the intermediate tonalitic or dioritic gneisses, can yield granitic melts in large amounts by partial melting, and how the rising granitic magmas can retain sufficient H_2O to remain liquid during ascent. Voluminous literature discussion of these and other issues has led to much further experimental and theoretical work. Some of the outstanding problems of granite petrogenesis are briefly summarized below.

2.1.2 Problem of minimum melt compositions

Tuttle and Bowen (1958) showed that the H_2O-saturated simple granite system Ab-Or-Qz has a well-defined melting minimum temperature (eutectic above about 0.2 GPa) and that the minimum melt compositions at these low pressures are typical for many granites (molar K/Na ~ 1; Qz about 30 wt%). Subsequent investigations (Luth et al., 1964; Luth, 1976) showed, however, that the minimum melt compositions become quite sodic at higher pressures, so that the synthetic magmas correspond more to a trondhjemite than a true granite. Also, the Qz contents decrease continuously, falling to about 22 wt% at deep-crustal pressures near 1.0 GPa.

The trend of H_2O-saturated simple granite melt compositions toward trondhjemitic-syenitic compositions with pressure trend is arrested if the H_2O activity decreases, either by absence of a free aqueous phase or by dilution of the fluid with another component that has small solubility in granitic melts. Ebadi and Johannes (1991) found that increasing the CO_2 content of an aqueous phase tends to maintain K_2O and SiO_2 in granite minimum melts at elevated levels,

consistent with generation of a normal granite by partial melting of quartzofeldspathic source rocks at deep-crustal levels. Similar effects are seen when H_2O activity is reduced by addition of alkali chloride (Aranovich et al 2013). Melting experiments at 1.0 GPa on compositions emulating natural rocks containing hydrous minerals in the absence of a fluid phase ("dehydration melting") have shown that the first-melting products are granitic in character for both amphibole-biotite-bearing source rocks of broadly tonalitic composition (Rutter and Wyllie, 1988) and metasedimentary compositions (Vielzeuf and Holloway, 1988). The latter source materials yield granitic liquids that are characteristically rich in Al ("peraluminous"), capable of crystallizing granites with two micas at lower temperatures.

2.1.3 Problem of sufficiency of H_2O

Conceptual difficulties in the delivery of large amounts of CO_2 or other volatiles (including H_2O) to sites of partial melting in the deeper parts of the continental crust have caused most researchers to lean toward fluid-absent or dehydration melting to explain large-scale generation of granitic magmas (Stevens and Clemens, 1993; Inger and Harris, 1993 Nabelek and Bartlett, 1998). Since the only source of H_2O in this hypothesis is that resident in hydrous minerals, which, for intermediate quartzofeldspathic gneisses, are normally present in amounts no greater than 20 modal percent, the amount of H_2O necessary to yield a given quantity of partial melt by dehydration melting is a key issue. Liquidus H_2O contents of granitic magmas in the undersaturated region at elevated pressures have not been heretofore accurately defined; estimates based on model extrapolation of fragmentary experimental data at lower pressures vary widely (Johannes, 1985; Johannes and Holtz, 1991; Holtz et al., 2001).

The most favorable case for dehydration melting in the generation of granites of batholithic dimensions invokes the smallest possible liquidus H_2O contents at probable deep-

crustal melting temperatures. Johannes and Holtz (1991) pointed out that large masses of granitic liquid undersaturated in H_2O can rise a certain distance through the crust without extensive freezing, but the ascent would necessarily be nearly isothermal. Since most estimates of emplacement temperatures of two-feldspar granites are less than 900 °C (for instance, melt inclusion thermometry gives about 875 °C for the Transbaikalia granites: Litvinovskii et al., 1994) the amount of H_2O available in tonalitic rocks (0.6-0.8 wt%) would be only marginally adequate for large-scale melting (say, about 20 percent) at the liquidus H_2O content of 2.3 wt% at 900 °C and 1.0 GPa shown by Johannes and Holtz (1991). If the liquidus H_2O content at these conditions is as high as that given by the revised estimate of Holtz et al. (2001), it is difficult to explain the great swarms of intra-continental, or A-type granites such as Transbaikalia, where accumulations are as great as half a crustal thickness over areas of subcontinental dimensions, as emphasized by Litvinovskii et al. (1994) and more recently by Weinberg and Hasalova (2015). If, on the other hand, the liquidus H_2O estimate of Johannes and Holtz (1991) is an over-estimate, the problem of large-scale granite production by dehydration melting is less severe.

2.1.4 Problems of experimental measurement of liquidus H_2O

Most melting experiments have used natural or synthetic minerals oxide mixes or gels as starting materials. Equilibrium at low H_2O contents is very hard to achieve, even in long runs, as shown by Holtz et al. (2001). These authors showed that, for bulk compositions of a simple granite with 1 wt% H_2O or less, previous estimates have underestimated the liquidus temperature at 0.5 GPa by as much as 75 °C. A consequence of their revised temperature scale is that liquidus H_2O contents at any pressure and temperature must be substantially greater than previous estimates. The Holtz et al. (2001) extrapolated H_2O content at 900 °C and 1.0 GPa is 3.6 wt%, 60% higher than the frequently cited scale of Johannes and Holtz (1991). Possible yields of

granitic liquid by dehydration melting of intermediate rocks are accordingly so small that there appears to be a quantitative mismatch with observed volumes of granite batholiths (Aranovich et al., 2014; Weinberg and Hasalova, 2015).

An alternative experimental procedure, used by Webster (1997), is to melt starting materials, including measured amounts of H_2O, at temperatures high enough to homogenize them into liquid, and then lower the temperature by stages at constant pressure, searching for the first crystallization products (feldspar and/or quartz). Though this method bypasses the problem of slow heterogeneous melting, it introduces the problem of undercooling, well known in natural, as well as experimental silicate systems (Nabelek et al., 2010). The first crystals may appear only at temperatures well below those of the equilibrium liquidus, and crystals may show metastable compositions.

2.1.5 Scope of the present work

It is clear from previous experimental work on granite melting/crystallization that extraordinary steps must be taken to demonstrate equilibrium liquidus temperatures and H_2O contents. The latter quantity is subject to considerable error in conventional melting experiments starting from crystalline materials because the H_2O must be determined by spectroscopy or microprobe totals of quenched glasses, and these methods are subject to considerable errors of calibration, lack of homogeneity, possibility of microvesiculation, etc. Ideally, chemical equilibrium should be defined by some sort of reversal process of approach to a final state from both the crystal-undersaturated and over-saturated directions, with approach of assemblages and compositions to common values. These are criteria that can be very hard to realize in charges of low H_2O content in quartz-feldspar systems, even for experiments at high temperature and for long duration (Holtz et al., 2001).

The present work attempts to achieve such reversed convergence of quenched products in the H_2O-undersaturated portion of the haplogranite system by temperature cycling of charges at constant pressure. If a temperature of complete melting of crystals, and a temperature of crystal precipitation in a charge known to have been previously completely melted, have been determined, the liquidus temperature for a liquid of known H_2O content is bracketed. Some demonstration that the liquidus temperature corresponds to a minimum on the liquidus surface at a given pressure must be performed by varying the composition of the anhydrous components. Such experiments are necessarily multi-stage: the temperature is changed in a single experiment up to 4 times with long equilibration times at each stage. The tedious nature of this type of experiment mandated that only a single isobaric suite of experiments, at 1.0 GPa, could be performed on a feasible time-scale. The present study involved 100 reversed experiments and over one year, with as many as four high pressure, high temperature apparatus running simultaneously.

2.2 Experimental Methods

2.2.1 Starting materials

Four different bulk compositions of dry starting materials were studied (Ab-Or-Qz, in wt%): 40.0-40.0-20.0, 37.5-37.5-25.0, 36.25-36.25-27.50, 35.0-35.0-30.0 where Ab = $NaAlSi_3O_8$, Or = $KAlSi_3O_8$ and Qz = SiO_2. An Or:Ab weight ratio of 1:1 was chosen based on typical bulk compositions of natural haplogranites (Luth et al. 1964) and the feldspar K:Na ratio of the dry simple granite solidus temperature minimum at 1.0 GPa (Luth, 1976). The effect of Qz on the minimum melting temperature was investigated by varying the concentration of this component from 20 wt% to 30 wt% of the dry starting materials. The depression of the melting

temperature with the addition of varying amounts of water was investigated at five different water contents: 2.97, 4.15, 5.82, 7.92 and 12.00 wt% water. These composition ranges give sufficient coverage of melt compositions from the dry melting temperature to near the fluid saturated solidus.

A few preliminary experiments showed that liquidus compositions could not be rigorously defined using crystalline starting materials, because of sluggish melting among heterogeneous reactants. For that reason we chose homogenized glass starting materials. Granitic glasses were prepared from synthetic $NaAlSi_3O_8$ (albite) glass, synthetic $KAlSi_3O_8$ (sanidine) glass, and Puratronic SiO_2 glass. The $NaAlSi_3O_8$ glass was prepared by methods described in Hayden and Manning (2010). D. B. Stewart prepared the $KAlSi_3O_8$ glass (# 95 GQ A1). Each of the four starting compositions was prepared by mixing weighed finely ground portions of the three glasses with prolonged stirring under acetone in an agate mortar. The ground glasses were baked out at 600 °C to remove any organic residue. The glass mixes were packed into platinum capsules and fused together in a tube furnace at 1400 °C and 1 atm for approximately three hours, then fine-ground again under acetone in an agate mortar and again baked out at 600 °C.

Platinum tube segments of either 2.0 or 3.5 mm diameter were welded at one end in an oxy-acetylene flame and then the whole capsule annealed with this flame. A dry charge was weighed into the capsule and ultra-pure 18 MΩ-cm water was added with a microliter syringe in slight excess. The amount of water added ranged from 2.97 to 12.00 wt% of the total charge. Amounts of total charge ranged between 10-40 mg. The water was allowed to evaporate on the balance until the desired weight was reached, then the capsule was pinched and sealed by arc-welding. Weight loss on sealing was usually less than 50 μg, all of which is attributable to platinum evaporation. Capsules were weighed before and after all runs. No detectable weight

loss occurred during an experiment. The weight measurements were made with a Mettler Toledo UMX2 ultra-microbalance with a stated precision of 2×10^{-4} mg.

2.2.2 Piston-cylinder methods

All experiments were carried out in a piston-cylinder apparatus of 2.54 or 1.91 cm diameter with graphite heater sleeves and NaCl pressure medium. For runs at T > 900 ^{o}C, pressed BN spacers 0.35 cm thick were placed above and below the capsule to prevent melting of the pressure medium. This assembly requires a -0.6 GPa pressure correction based on quartz solubility calibrations (Newton and Manning 2000). No pressure correction was necessary for the all-NaCl cell. Pressures were monitored on a Heise bourdon tube gauge and are believed accurate to ± 0.3 GPa (Johannes et al. 1971). Temperatures were controlled and monitored digitally using an S-Type thermocouple (uncertainty ±3 °C). The 3 mm-thick capsules were loaded transversely to the heater cylinder in order to minimize the temperature gradient across the sample. An assembly was cold pressed to 0.7 GPa and then heated. As pressure rose upon heating, the pressure was bled to maintain the desired pressure of 1.0 GPa. For multi-temperature step experiments where the temperature was lowered, the pressure was increased during the run to maintain the desired pressure of 1.0 GPa. Runs were terminated by quenching to < ~100 °C in ~20 seconds by turning off the heating power.

2.2.3 Analytical methods

In most experiments, the charge could be removed nearly intact from the sealed platinum capsule after the run by making an incision along the side and welded bottom of the capsule, then removing the glassy slug with a pair of tweezers. Opposite sides of the glassy slug were ground and polished with successively finer silicon carbide sandpaper, starting with 600, then 800 and 1200 grit paper to make a thick section. This allowed for unhindered observation of the charge

under cross-polarized light. Some charges were lightly ground in a mortar and pestle and the fragments observed under immersion oils with the polarizing microscope. Selected samples were mounted in epoxy resin, polished with water based diamond paste, and studied with a Tescan Vega-3 XMU scanning electron microscope (SEM) using the back-scattered electrons.

Compositions of selected charges were determined using a JEOL 8500 electron microprobe in the Department of Earth, Planetary and Space Sciences at UCLA. Operating conditions were 15 keV, 10 nA and a 15μm beam spot size. Particular attention was paid to characterization of subtle textures of crystallization (and sometimes resorption) that were identified with the optical and SEM methods. Analyses of selected crystal-free experimental charges demonstrated, when corrected for the initial H_2O contents, the homogeneity and integrity of the glass starting materials, within the analytical uncertainties (Table 2.1).

Selected samples were ground and analyzed using the PANalytical Powder X-ray diffractometer (XRD) with Cu Kα (λ=1.5408 Å) radiation in the Chemistry Department at UCLA. Scans were collected in the range of $20° \leq 2\theta \leq 60°$ with CuKα radiation at a rate of 0.0170° 2θ steps per 60.6900 seconds. An annealed CaF_2 internal standard was used to calibrate and index the diffraction peaks. The peak positions were converted to unit cell lengths and volumes of crystalline products using the UnitCell OSX program of Holland and Refern (1997).

2.2.4 Reversal strategy

A complex run procedure was necessary, because of severe problems of undercooling, metastable crystallization and sluggish resorption of crystals, in order to prove reversibility of liquidus crystallization. In principle, a minimum of four experiments was required to obtain one bracket along the liquidus; however in practice as many as 8 or 10 multi-step experiments were required to bracket the liquidus to at most ±25 °C. The temperature was varied in the reversal

experiments while the composition and pressure remained fixed. Descriptions of the four reversal steps are outlined below. Figure 2.1 is a cartoon depicting the temperature versus time path in a reversal cycle. In brief, the procedure was to homogenize the bulk composition at a temperature well above the liquidus, following Webster (1997), then crystalize the charge by decreasing the temperature in increments, and, finally, reverse the crystallization by raising the temperature in increments of ~25 °C until all of the crystals were resorbed into the liquid.

Step 1 Experiment: The aim of the first step was to insure that the water added to the dry starting materials was homogenized into the melt at a sufficiently high T above the liquidus. This step also served to resorb small particles of SiO_2 glass that did not fully dissolve when the starting material was made. The duration of Step 1 experiments was approximately 24 hours.

Step 2 Experiment: The goal of this step was to find the maximum temperature required to crystalize feldspar and quartz directly from a homogenized melt containing a specified amount of water. This experiment followed Step 1 by lowering of the temperature to T_2 for ~ 72 hours until quartz and alkali feldspar crystalized from the melt. From this crystallization reaction, a preliminary lower bound on the liquidus was determined. Further experiments of this type were usually required to refine the lower temperature bracket.

Step 3 Experiment: The aim of this experiment was to reverse the crystallization step by monitoring the progressive resorption of the crystalline phase(s) into the melt with increasing temperature above T_2. In a typical Step 3 experiment, feldspars formed at a lower temperature were partially resorbed, quartz increased in crystal size, and a new generation of re-equilibrated feldspars formed. The highest temperature, T_3, where the new generation of feldspar and quartz formed represents the true lower bound of the liquidus for a specific bulk composition. These runs typically were held at temperature T_3 for 3-5 days.

Step 4 Experiment: Step 4 experiments are essentially the same as Step 3 experiments, but the final temperature, T_4, is slightly higher than T_3. At T_4, the last remnants of crystals are resorbed into the liquid. T_4 represents the upper bound on the liquidus. Together with T_3, this defines a bracket on the liquids, as determined by reversed experiments. These runs also typically were held at temperature T_3 for 3-5 days before raising to temperature T_4.

2.3 Results of Experiments

2.3.1 Crystallization sequence and time requirements

In order to establish the required run duration required for crystallization, timed experiments were made on samples containing 3.9 to 4.1 wt% water, with a dry bulk composition of $Ab_{36.25}Or_{36.25}Qz_{27.50}$. All samples were homogenized at a temperature of 1050 °C, a temperature well above the liquidus at 4.0 wt% water, for a minimum of 13 hours, then were lowered to a final temperature of 800 °C for various times, ranging from 6 to 72 hours. The results of these experiments, as determined by polarized light microscopy, are given in Table 2.2. They show that β-quartz is the first phase to crystallize from the melt, for this particular bulk composition, requiring between 6 and 24 hours at 800 °C and 1.0 GPa to nucleate and grow. A weakly birefringent sanidine solid solution begins to form after 24 to 35 hours, and improves in crystallinity but without much further change in appearance for up to 72 hours. This time was taken to be the minimum run duration necessary to produce definitive crystallization reactions.

2.3.2 Characterization of run products

Quenched run products consisted of glass, representing former liquid, quartz and feldspars of variable composition. The starting materials, multi-step temperature-time histories, and resulting phases are given in Table 2.3.

Many experimental charges were easily characterized with only a petrographic microscope; however, detailed analysis of the textures and compositions of the crystalline phases required the aid of backscattered electron SEM images. Pertinent features of the quenched phases are briefly listed below.

Glass: The former liquid phase was easily recognized as isotropic, apparently homogeneous and bubble-free (Fig. 2.2), except in experiments with 12 wt% H_2O, which contain numerous small spherical bubbles interpreted to have formed in the quenching process.

β-quartz: The SiO_2 phase that crystallized in most experiments had the morphology of β-quartz (R. Esposito, personal communication) in agreement with its known stability field. The skeletal quartz crystals were mostly < 10 μm in size and dispersed throughout the charge. Figs. 2.2A and 2.2B show a typical charges that crystallized skeletal quartz, followed by overprinting of feldspar. This interpretation agrees with the crystallization sequence observed in the kinetic experiments discussed above.

Feldspars: Three forms of feldspars initially crystallized from the melts in Step 2 experiments. Rosettes of large radiating crystals (Figures 2.2A, B), large sector-zoned alkali feldspars with granophyric quartz intergrowths (Figure 2.2C), and spectacular composite hopper crystals (Figure 2.2D), formed depending on the run time, SiO_2 content and H_2O content during these experiments. While the rosettes were generally much more common in Step 2 experiments, the granophyric texture and the hopper crystals appeared in the low-silica $Ab_{40}Or_{40}Qz_{20}$ run products. We call the feldspars "primary" that crystallize initially during Step 2 experiments, whereas "secondary" feldspars are those that recrystallize on the exterior portions of the primary feldspars during reversal experiments (Step 3 experiments). Secondary feldspars differ from the

primary feldspars in crystal habit, structure, and composition. The primary feldspars are seen in figures 2.2A-D, and examples of secondary feldspars are shown in figures 2.3A-D.

Quartz-feldspar micro-intergrowths: Figures 2.2C and 2.2D show quartz formed as intergrowths in feldspars, both in rosettes and in composite crystals. Figure 2.2C shows a portion of sample G63, Table 2.3, that exhibits sector-zoned micro-intergrowths of quartz in a large rosette feldspar. The interiors of the hopper crystals are partially occupied by granophyric intergrowths.

2.3.3 Compositions of phases

The results of the microprobe analyses are tabulated in Tables 2.4A and 2.4B. For hydrous samples that contained glass without water exsolution vesicles, the electron microprobe totals overestimate the amount of water contained in the glass by a regular amount for samples containing between 0 and ~ 8 wt% H_2O (Figure 2.4). The relationship between H_2O determined by probe totals and the expected amounts is $x_{H_2O\ measured} = 1.347\ x_{H_2O\ added}$ with a correlation of $R^2 = 0.999$.

Primary feldspars: The large rosettes of feldspars had highly anomalous compositions. Some of the analyses were, in fact, quite close to the granite starting compositions. Apparently, highly metastable feldspars nucleated and grew from a homogeneous melt that was suddenly undercooled. Many optically homogeneous feldspars were silica-rich compared to normal alkali feldspar, with as much as 75 wt% SiO_2 and also had high, but extremely variable K/Na, up to 2.8, although most were in the range of 1.2-1.6. Extreme K-enrichment was accompanied by an anomalous Si/Al ratio in most of these samples of about 4.4:1 instead of the normal 3:1.

Because some primary feldspars had microscopically visible granophyre-like quartz intergrowths (Figure 2.2C), it may be suspected that the apparently homogeneous primary feldspars are submicroscopic intergrowths of a more normal feldspar and quartz, rather than

metastable solid solutions. That there is probably some excess SiO_2 in solid solution is shown by the unit cell constant determination of the primary feldspar of Run #G45, Table 2.3. This sample was crystallized from a homogenized glass with 25 wt% Qz and 3.02 wt% H_2O. A list of the peaks used for the unit cell determination of the feldspar is given in Table 2.5, and a full list of peaks is given in Table 6 in the Appendix. A -0.05^o 2θ correction to the 2θ peak positions was required when comparing the measured peaks of an annealed reagent fluorite internal standard to those listed in McMurdie et al (1985). The feldspar peaks were identified according to the indexing of sanidine used by Wright and Stewart (1968). The unit cell parameters for the feldspar in this sample were calculated in UnitCell (Holland and Redfern, 1997) and are: a = 8.397 ± 0.003Å, b = 12.991 ± 0.002Å, c = 7.160 ± 0.002Å, β = 116.07 ± 0.02, unit cell volume = 701.625 ± 0.248$Å^3$. These values are reported to the 95% confidence level. The unit cell volume is compared to the trend of well-crystallized high structural state synthetic alkali feldspars (Orville, 1967) in Figure 2.5. This figure shows that some of the excess SiO_2 typical of analyses of rosette feldspar crystallized from the high SiO_2 bulk compositions is indeed present as a solid solution component.

The coarser Step 2 feldspar-quartz intergrowths were characteristic of the lower-SiO_2 bulk compositions (20 and 25 wt% Qz). Some of these textures were strikingly similar to those reported by Baker and Freda (2001) in their experiments at 0.5 GPa on K-feldspar-quartz intergrowths crystallized from supercooled hydrous melts.

Secondary feldspars: Secondary feldspars (feldspars that crystallized during reversal experiments at a reaction boundary between a primary feldspar and the surrounding liquid) have normal feldspar compositions and are thus shown to be re-equilibrated, more stable phases. The average SiO_2 content of secondary feldspars was 66.2 wt%, and the Si/Al and K/Na ratios

were 3.0:1.0 and ~1.6:1, respectively, typical hypersolvus sanidines (Parsons, 1978). Not surprisingly, enrichment in the potassium content of the feldspars led to depletion of the potassium content of adjacent glass, which has molar K/Na of 0.68 to 0.74.

2.3.4 Summary of reversal experiments

The results from the reversal experiments are shown in bold face in Table 2.3. Figure 2.6 indicates that liquidus temperatures are almost independent of SiO_2 concentration, and display a minimum near ~27.5±0.5 wt%. Figure 2.7 is a projection from wt% Qz space onto the $T - x_{H_2O}$ plane (i.e. all reversal experiments are plotted on the same plane, irrespective of the wt% Qz content of the sample) for runs that define the 1.0 GPa liquidus. The value we used at the fluid saturated solidus was taken from the Johannes and Holtz (1991) study, and the dry melting temperature was taken from the work of Holtz et al. (2001).

Figure 2.8 shows T and H_2O content of our reversed liquidus brackets together with the data of Johannes (1985), Johannes and Holtz (1991) and Holtz et al. (2001), all of which are their extrapolations from lower pressure measurements. Our results agree with Holtz et al. (2001) at low H_2O content, and with Johannes (1985) at high H_2O contents. The reversed brackets plot on the high end of the extrapolated water contents at the liquidus of all other previous determinations. For the reversed liquidus curve of the haplogranite composition $Ab_{36.25}Or_{36.25}Qz_{27.50}$ at 1.0 GPa, our experiments yield the following equation

2.1. $$T\left(X_{H_2O}\right) = -0.0784x_{H_2O}^3 + 4.2886\, x_{H_2O}^2 - 81.851\, x_{H_2O} + 1167\ ^\circ C$$

where x_{H_2O} is H_2O concentration in wt%.

2.4 Discussion and Interpretations

2.4.1 Evidence for equilibrium brackets

The SEM analysis revealed that quartz was present in every quenched charge that also contained feldspar. We found no evidence that quartz crystallization was inhibited or occurred metastabily at run times longer than about six hours. A few charges with 30 wt% Qz yielded quartz as the only crystalline phase immediately below the temperature of complete fusion (T_4), indicating that crystallization of the highest-SiO_2 composition is slightly divariant for a given H_2O content.

Partial resorption of the primary feldspar upon raising the run temperature was initially thought to signal the onset of complete melting, thus defining the liquidus temperature for a hydrous granitic liquid of a certain composition. However, upon further investigation the interior of a typical primary feldspar was found to be persilicious and nonstoichiometric, indicating probable metastable crystallization. It follows that runs crystallizing the undercooled feldspar provide only a lower bound on the liquidus: at a somewhat higher temperature there is the possibility of crystallization of a more stable feldspar. This is indeed what detailed microprobe analysis of the partially resorbed rims of primary feldspars revealed. Feldspars of normal composition (i.e. molar Si/Al = 3.0) formed in reversal runs. These secondary feldspars were euhedral to subhedral, forming at the reaction boundary between the margins of the primary feldspars and the liquid. The resorption rim penetrates radially inward as the feldspar reacts with the surrounding liquid until only a ghostly outline of the original metastable feldspar remains, outlined by more stable secondary feldspars (Figs. 2.3A and 2.3D). In most runs it was apparent that quartz was still present, and had actually increased in grain size, even though ~90 percent of the original feldspar had disappeared. For these reasons it was necessary to show that, in a

reversal cycle, not only did both primary and secondary feldspars form along with quartz, but also that these phases completely disappeared upon raising temperature still higher. If any quartz or feldspar, primary or secondary, remain in a quenched charge, one cannot be sure that the liquidus temperature has been exceeded. These stringent conditions for the definition of the liquidus at a given H_2O and SiO_2 content necessarily resulted in somewhat broad temperature brackets. Our modal bracket interval is about ±12.5°C. There is a suggestion of a minimum at ~27.5±0.5 wt% SiO_2 (Figure 2.7), though the data are insufficient to prove this at all the investigated water contents.

2.4.2 Metastable feldspars and granophyres

The unit cell volume of the well-analyzed product feldspar of Run #G45 is significantly smaller than that of a normal high structural state alkali feldspar of the same K/Na ratio (Figure 5), indicating that not all of the excess SiO_2 is present as submicroscopic quartz intergrowths, but that some of it is present in solid solution with $(K,Na)AlSi_3O_8$. Excess SiO_2 in synthetic and natural feldspars has been reported by several authors (Grundy and Ito, 1970; Carman and Tuttle, 1967; Perry, 1968; Sturt, 1970).

Megaw (1970) noted that sanidine and the coesite polymorph of SiO_2 are topologically identical. This suggests that the persiliceous component of our metastable feldspars may exist in the structural arrangement of coesite. Some rocks from very high pressure terranes contain coesite or quartz pseudomorphs after coesite intergrown with K-feldspar (Yang et al., 1998); this may indicate that such a solid solution may exist in nature. Based on a coesite unit cell volume of 551 $Å^3$ (Levien and Prewitt, 1981), the extent of SiO_2 solid solution in the feldspar of Run #G45 is about 5 mol percent on a 4-Si basis.

It appears possible from our work that natural conditions of fast quenching of hydrous silica-rich liquid might initially produce metastable persiliceous alkali feldspar solid solutions which subsequently unmix to sanidine-quartz intergrowths. The swiftly-cooled debris from the Ries Kessel (Germany) impact event (Osinski, 2004) and the Fish Canyon Tuff (Colorado) ignimbrite deposit (Lipman et al., 1997) contain granophyre clasts having textures remarkably similar to some of those produced in the present study. It may be that H_2O content of granitic liquids, as well as undercooling, is essential to the formation of granophyre and possibly a persiliceous feldspar precursor.

2.4.3 Implications for dehydration melting in granite genesis

Johannes and Holtz (1991) pointed out the restrictive nature of dehydration melting to produce voluminous amounts of granitic liquid by melting of the deep crust, if, as is generally believed, the majority rock type is an intermediate gneiss with typical amounts of biotite and calcic amphibole, the main H_2O carriers; such a source rock would have no more than about 0.6-0.8 wt% resident H_2O. For many or most granites, the melting temperature at the source was probably no higher than 900 °C, based on subsolvus feldspars, common presence of both biotite and amphibole in the crystallization products, and measured homogenization temperatures of melt inclusions (Litvinovskii et al., 1994).

At 900 °C and a deep-crust pressure of 1.0 GPa, Johannes and Holtz (1991) show 2.3 wt% H_2O at the liquidus of a simple granite. This means that, even in the case of complete dehydration and perfect extraction of liquid, the yield of granitic liquid could be no higher than about 25 volume percent. This hardly seems compatible with the observed volumes of granite in some terranes like Transbaikalia, where granite crops out over 60 percent of the surface and constitutes as much as a half-crustal thickness (Litvinovskii et al., 1994). For these reasons

several workers have suggested that there must commonly have been some additional input of H_2O into the regions of partial melting in the deep crust (Litvinovsky and Podladchikov, 1993; McLelland et al., 2002; Martin, 2006; Aranovich et al., 2013; Aranovich et al., 2014; Weinberg and Hasalova, 2015).

The present work exacerbates the difficulty of dehydration melting to produce large amounts of deep-crustal melting. Our determinations of the liquidus H_2O contents of granite fall on the high side of all previous estimates. At 1.0 GPa and 900 °C the H_2O required would be 3.7 wt%, nearly double the estimate of Johannes and Holtz (1991) and perhaps somewhat higher than the revised estimate of Holtz et al. (2001), implying substantially reduced maximum yields of granitic liquid if the only source of H_2O is that resident in deep-crustal gneisses.

Possible mechanisms that might transport H_2O into lower crustal melting zones are deep recirculation of surficial fluids in thermal convection cells (Wickham and Taylor, 1985; McLelland et al., 2002), intrusion of very hydrous basalts into the deep crust (Litvinovsky and Podladchikov, 1993), and outgassing of the subcontinental upper mantle (Collerson and Fryer, 1978). These mechanisms are so poorly defined at present, compared to dehydration melting, that proponents of the latter mechanism may be justified in insisting on the possibility of very high initial temperatures of partial melting, followed, if necessary, by lower temperature concentration of the H_2O and re-equilibration of the final granite bodies.

2.5 Conclusions

- The first experimental determination of the haplogranite liquidus H_2O content at deep crustal P and T (625-1050˚C, 1.0 GPa) has been made. The minimum temperature of the 1.0 GPa liquidus at a given water content occurs at ~27.5 ± 0.5 wt% Qz, regardless of H_2O content. Equation 2.1 describes the liquidus as a function of weight percent water for a haplogranite of this composition: $Ab_{36.25}Or_{36.25}Qz_{27.50}$
- Due to the severity of undercooling problems, in particular metastable undercooled feldspars, a reversal procedure was developed to obtain equilibrated, stoichiometric feldspars and to bracket the liquidus. Undercooling by as much as 50 °C was observed.
- Equation 2.1 describing the liquidus can be used to make fertility calculations of the volume of magma generated by hydrous melting of granite of similar composition. The high liquidus H_2O content presents a challenge for producing voluminous amounts of metaluminous granites from lower crustal biotite-amphibole gneisses by dehydration melting.
- The metastable, undercooled, nonstoichiometric feldspars exsolved to fine-grained granophyric intergrowths resembling some that have been described from volcanic and impactite surge deposits.
- The metastable feldspar produced in these experiments have an excess of silica. The excess SiO_2 may be present in the configuration of the coesite crystal structure and form a solid solution with the monoclinic feldspar structure, incorporating ~ 5 mol % SiO_2 into the feldspar. This metastable feldspar has the potential to be recognized as a new mineral.

Table 2.1: Electron microprobe totals for representative glass samples. The analysis shows that the intended compositions were obtained. 95% confidence intervals are reported

sample:	**G56**			**G74**			**G75**		
wt. % dry mix (Ab,Or,Qz)	**(35, 35,30)**			**(37.5, 37.5, 25)**			**(37.5, 37.5, 25)**		
wt. % H_2O added	**3.04**			**4.12**			**5.85**		
number of analyses	**n=10**			**n=10**			**n=10**		
(wt. % basis)	**normailzed**	**2σ**	**expected**	**normailzed**	**2σ**	**expected**	**normailzed**	**2σ**	**expected**
SiO_2	74.28	0.40	74.42	72.63	0.32	72.78	71.36	0.38	71.45
Al_2O_3	12.93	0.23	12.82	13.30	0.25	13.13	13.01	0.12	12.89
Na_2O	4.13	0.11	4.01	4.19	0.10	4.11	4.01	0.13	4.03
CaO	0.01	0.01	-	0.02	0.02	-	0.03	0.02	-
K_2O	5.58	0.23	5.74	5.69	0.16	5.85	5.62	0.15	5.78
raw totals:	95.91			94.61			92.11		
wt. % H_2O by difference:	4.09			5.39			7.89		
values normalized to:	98.95			98.73			97.97		

Table 2.2: Results from kinetic experiments showing the time required to crystallize quartz and feldspar

run	wt. % Qz	wt. % H_2O	T profile (°C)	P (GPa)	time (h)	result
GK-1	27.5	4.118	1050, 800	1.0	23, 6	L
GK-2	27.5	4.108	1050, 800	1.0	16, 24	L+qz
GK-3	27.5	4.056	1050, 800	1.0	21, 72	L+fls+qz
GK-4	27.5	4.065	1050, 800	1.0	21,48	L+fls+qz
GK-5	27.5	3.911	1050, 800	1.0	13, 35	L+fls+qz

Table 2.3: Run table organized and separated by weight percent water in the charge. Reversed equilibrium experiments are highlighted in bold font. L=liquid, fls=feldspar, qz=quartz

run	wt. % Qz	wt. % H_2O	T (°C)	time (hrs)	result
G99	**25**	**2.849**	**1050, 900, 1000**	**6, 70, 102**	**L**
G87	**25**	**2.914**	**1050, 900, 950**	**16, 74, 74**	**L+fls+qz**
G50	25	2.939	1050, 950	17, 75	L
G41	25	3.016	1050, 850	17, 144	L+fls+qz
G40	25	3.021	1050, 900	20, 70	L+fls+qz
G45	25	3.032	1050, 800	17, 51	L+fls+qz
G46	**25**	**3.063**	**1050, 800, 875**	**19, 72, 54**	**L+fls+qz**
G72	**27.5**	**3.015**	**1050, 900, 935**	**18, 72, 150**	**L+fls+qz**
G79	**27.5**	**3.033**	**1050, 900, 985**	**17, 75, 72**	**L**
G55	27.5	3.052	1050, 900	19, 98	L+fls+qz
G65	27.5	3.054	1000, 900	4, 89	L+fls+qz
G58	27.5	3.054	1050, 935	18, 48	L
G39	30	2.972	1050, 850	21, 71	L+fls+qz
G49	**30**	**2.994**	**1050, 850, 900**	**18, 75, 52**	**L+fls+qz**
G85	**30**	**3.005**	**1050, 950, 1000**	**15, 72, 74**	**L**
G44	**30**	**3.018**	**1050, 850, 900**	**20, 73, 89**	**L+fls+qz**
G89	**30**	**3.026**	**1050, 850, 950**	**16, 88, 104**	**L+fls+qz**
G36	30	3.039	1050, 900	19, 48	L+qz
G52	30	3.039	1050, 950	23, 24	L+qz
G56	30	3.040	1050, 1000	20, 48	L
G48	20	4.124	1000, 800	15, 48	L+fls+qz
G5	20	4.129	950	69	L
G8	20	4.153	950, 850	23, 120	L+fls+qz
G6	20	4.170	950, 850	24,70	L+fls+qz
G96	**25**	**4.057**	**1050, 800, 950**	**21, 47, 73**	**L**
G97	**25**	**4.152**	**1050, 800, 900**	**17, 72, 103**	**L**
G10	25	4.164	950, 900	69, 47	L
G14	**25**	**4.164**	**950, 800, 850**	**69,96,72**	**L+fls+qz**
G12	25	4.229	950, 800	66, 99	L+fls+qz
G100	**27.5**	**3.840**	**1050, 800, 900**	**20, 73, 93**	**L**
G69	27.5	4.075	900, 850	67, 74	L+fls+qz
G82	**27.5**	**4.096**	**1050, 800, 915**	**46, 71, 27**	**L**
G62	27.5	4.102	1050, 875	17, 77	L
G54	27.5	4.114	1050, 850	20, 98	L+fls+qz
G63	27.5	4.115	1050, 825	14, 221	L+fls+qz
G74	27.5	4.120	1050, 900	25, 93	L
G59	27.5	4.177	1050, 825	17, 81	L+fls+qz
G93	**27.5**	**4.178**	**1050, 800, 875**	**20, 71, 148**	**L+fls+qz**

G83	**30**	**3.768**	**1050, 900, 950**	**24, 80, 86**	**L**
G1	30	4.054	950	52	L
G35	**30**	**4.103**	**950, 800, 850**	**43, 74, 165**	**L+fls+qz**
G11	30	4.116	950, 800	66, 99	L+fls+qz
G13	**30**	**4.147**	**950, 800, 850**	**69,96,72**	**L+fls+qz**
G3	30	4.167	950, 900	71,70	L+fls+qz
G7	30	4.200	950, 850	65,70	L+qz
G28	**25**	**5.797**	**900, 750, 800**	**45, 74, 95**	**L+fls+qz**
G47	25	5.846	900, 700	19, 52	L+fls+qz
G30	25	5.850	900, 800	48, 77	L
G51	**25**	**5.862**	**900, 700, 750**	**14, 75, 52**	**L+fls+qz**
G29	25	5.884	900, 750	67, 95	L+fls+qz
G80	**25**	**5.891**	**900, 775, 850**	**68, 70, 126**	**L**
G76	**27.5**	**5.817**	**900, 775, 825**	**72, 75, 99**	**L**
G75	27.5	5.853	900, 825	92, 98	L
G68	27.5	5.857	900, 775	24, 47	L+fls+qz
G66	27.5	5.864	900, 775	71, 27	L+fls?
G71	27.5	5.868	900, 800	70, 119	L+fls+qz
G73	27.5	5.873	900, 750	69, 100	L+fls+qz
G26	30	5.819	900, 800	46, 71	L+qz
G25	30	5.822	900, 750	41, 71	L+fls+qz
G33	30	5.822	900, 775	44, 119	L+fls+qz
G27	**30**	**5.823**	**900, 750, 800**	**45, 74, 95**	**L+fls+qz**
G2	30	5.841	850	65	L
G34	30	5.859	900, 775	44, 119	L+fls+qz
G81	**30**	**5.894**	**900, 800, 850**	**66, 70, 120**	**L**
G92	**25**	**7.919**	**900, 700, 800**	**68, 69, 98**	**L**
G53	25	7.946	900, 650	23, 103	L+fls+qz
G57	25	7.961	900, 675	70, 192	L+fls+qz
G88	**25**	**8.038**	**900, 700, 750**	**67, 69, 113**	**L+fls+qz**
G23	25	8.101	850, 700	25, 70	L+fls+qz
G20	25	8.102	850, 750	44, 70	L
G19	25	8.147	850, 750	90, 74	L
G17	25	8.277	850, 700	94, 96	L+fls+qz
G67	**27.5**	**7.878**	**900, 700, 725**	**21, 69, 65**	**L+fls+qz**
G64	27.5	7.902	900, 700	18, 70	L+fls+qz
G95	**27.5**	**7.928**	**900, 700, 775**	**73, 89, 168**	**L**
G77	**27.5**	**7.971**	**900, 700, 750**	**69, 75, 96**	**L+fls+qz**
G60	27.5	8.065	900, 725	98, 93	L
G18	30	7.275	850, 750	90, 74	L+fls+qz
G16	30	7.832	850, 700	94, 96	L+fls+qz
G21	30	7.874	850, 750	44, 70	L

G84	**30**	**7.888**	**900, 725, 775**	**45, 60, 77**	**L+qz**
G22	30	7.902	850, 700	25, 70	L+fls+qz
G24	**30**	**7.904**	**850, 700, 750**	**45, 48, 121**	**L+fls+qz**
G90	**30**	**7.962**	**900, 725, 800**	**74, 70, 120**	**L**
G61	30	8.006	900, 725	98, 93	L+qz
G31	25	11.992	900, 675	50, 123	L
G94	**27.5**	**12.003**	**900, 625, 650**	**20, 74, 167**	**L+fls+qz**
G43	30	11.481	900, 650	69, 98	L
G42	30	11.990	900, 650	69, 98	L+qz
G37	30	12.004	900, 625	40, 123	L+fls?+qz
G38	30	12.048	900, 625	40, 123	L+fls+qz
G32	30	12.130	900, 675	50, 123	L

Table 2.4A: Electron microprobe analyses of oxides for selected samples. Glass, primary, and secondary feldspars are reported here to 95 % confidence interval

sample:	description	(Ab , Or, Qz)	wt. % H_2O	n	SiO_2 average	2σ	Al_2O_3 average	2σ	Na_2O average	2σ	CaO average	2σ	K_2O average	2σ	totals
G45	primary feldspar	(37.5, 37.5, 25)	3.02	15	74.18	0.470	14.177	0.170	4.066	0.146	0.018	0.015	7.114	0.224	99.554
G48	light primary feldsapr	(40, 40, 20)	4.12	6	65.680	1.996	18.531	0.347	4.582	0.755	0.009	0.016	10.435	1.012	99.237
G48	melt inclusion	(40, 40, 20)	4.12	4	68.424	1.565	13.124	1.659	4.481	0.652	0.022	0.020	4.599	0.471	90.649
G48	darker primary feldspar	(40, 40, 20)	4.12	2	73.847	0.158	14.157	0.058	3.503	0.980	0.018	-	8.130	0.854	99.675
G51	primary feldspar	(37.5, 37.5, 25)	5.86	3	73.778	0.325	14.088	0.068	2.871	0.121	0.002	-	8.948	0.315	99.685
G51	secondary feldspar	(37.5, 37.5, 25)	5.86	7	66.221	0.487	18.588	0.270	4.342	0.525	0.025	0.015	10.880	0.742	100.052
G51	glass	(37.5, 37.5, 25)	5.86	1	68.049	n/a	12.744	n/a	4.11	n/a	0.046	n/a	4.406	0.000	89.355
G56	glass only	(35, 35, 30)	3.04	9	73.496	0.395	12.797	0.229	4.091	0.106	0.008	0.006	5.521	0.228	95.911
G73	primary feldspar	(37.5, 37.5, 25)	5.87	7	74.198	0.398	13.577	0.245	2.216	0.177	0.012	0.010	9.432	0.291	99.430
G73	glass	(37.5, 37.5, 25)	5.87	11	68.988	0.422	12.512	0.187	4.121	0.171	0.016	0.019	4.661	0.133	90.298
G74	glass only	(37.5, 37.5, 25)	4.12	10	71.708	0.320	13.127	0.248	4.135	0.102	0.022	0.016	5.620	0.160	94.612
G75	glass only	(37.5, 37.5, 25)	5.85	10	69.904	0.381	12.744	0.116	3.929	0.126	0.026	0.018	5.510	0.148	92.112
G76	glass only	(37.5, 37.5, 25)	5.82	10	69.929	0.228	12.746	0.122	3.884	0.134	0.018	0.010	5.495	0.198	92.072
G77	glass only	(37.5, 37.5, 25)	7.97	9	68.101	0.334	12.322	0.100	3.577	0.152	0.024	0.014	5.232	0.154	89.257

Table 2.4B: Electron microprobe analyses for the same samples reported in table 2.4A. Cation counts are reported on an 8-oxygen basis

sample	description	Si	Al	Na	Ca	K	total	K/Na	Si/Al
G45	primary feldspar	3.262	0.741	0.340	0.001	0.413	4.751	1.215	4.402
G48	light primary feldsapr	2.998	0.997	0.406	0.000	0.608	5.010	1.498	3.007
G48	melt inclusion	3.271	0.739	0.415	0.001	0.280	4.707	0.675	4.426
G48	darker primary feldspar	3.257	0.738	0.300	0.001	0.476	4.750	1.587	4.413
G51	primary feldspar	3.270	0.730	0.291	0.001	0.431	4.724	1.481	4.479
G51	secondary feldspar	3.002	0.993	0.382	0.001	0.629	5.001	1.647	3.023
G51	glass	3.290	0.726	0.385	0.002	0.272	4.676	0.706	4.532
G56	glass only	3.319	0.682	0.359	0.000	0.318	4.678	0.886	4.867
G73	primary feldspar	3.287	0.709	0.190	0.001	0.533	4.720	2.805	4.636
G73	glass	3.303	0.706	0.383	0.001	0.285	4.677	0.744	4.678
G74	glass only	3.292	0.710	0.368	0.001	0.329	4.701	0.894	4.637
G75	glass only	3.295	0.709	0.359	0.001	0.331	4.696	0.922	4.647
G76	glass only	3.297	0.708	0.355	0.001	0.330	4.691	0.930	4.657
G77	glass only	3.306	0.704	0.337	0.001	0.324	4.673	0.961	4.696

Table 2.5: X-ray diffraction peaks for run # G45 using CuKα radiation. d-spacings reported here are not calibrated. A correction to the 2θ peak positions of -0.05° was requrired based on the CaF_2 peak positions reported by McMurdie (1985). (Note: qz= quartz, fls=feldspar)

(h,k,l)	Position (2θ)	Height (cts)	FWHM (2θ)	d-spacing (Å)	Rel. Int. (%)	phase
1 0 0	20.8656	1539.45	0.0976	4.2574	32.62	qz
2 0 -1	21.4990	971.36	0.1115	4.1334	20.58	fls
1 1 1	22.8491	892.82	0.0976	3.8921	18.92	fls
1 3 0	23.7153	2355.68	0.1533	3.7519	49.92	fls
1 1 -2	25.8457	1134.47	0.0976	3.4472	24.04	fls
1 0 1	26.6554	4061.21	0.1533	3.3443	86.06	qz
2 0 -2	27.4618	4507.59	0.1394	3.2479	95.52	fls
0 0 2	27.7740	4559.54	0.1255	3.2121	96.62	fls
1 1 1	28.3305	4311.39	0.1394	3.1503	91.36	fluorite
1 3 1	30.1053	1157.71	0.1533	2.9685	24.53	fls
0 4 1	30.8746	770.00	0.2230	2.8963	16.32	fls
2 4 -1	35.1221	874.51	0.0836	2.5551	18.53	fls
1 1 2	35.5342	260.94	0.1673	2.5264	5.53	fls
2 4 0	36.5219	718.45	0.0976	2.4603	15.22	fls
1 5 -1	37.2927	288.15	0.1394	2.4112	6.11	fls
0 6 0	41.7406	941.17	0.1673	2.1640	19.94	fls
2 2 0	47.0557	4718.93	0.1360	1.9296	100.00	fluorite
1 1 2	50.1381	398.69	0.2040	1.8180	8.45	qz
3 1 1	55.7959	1338.59	0.1020	1.6463	28.37	fluorite

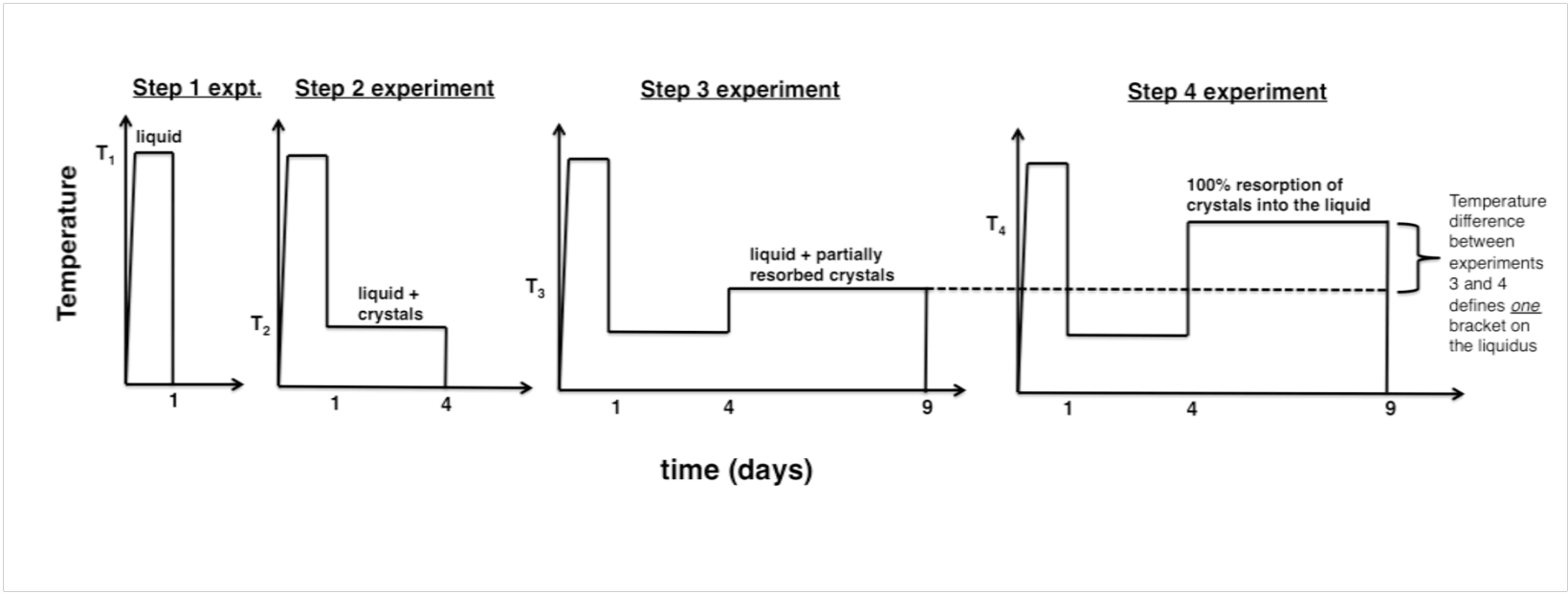

Figure 2.1: A cartoon showing the temperature vs. time profile for the four experiments (Step 1-4 experiments) required to obtain a single bracket along the liquidus at a specific haplogranite composition, water content, and pressure.

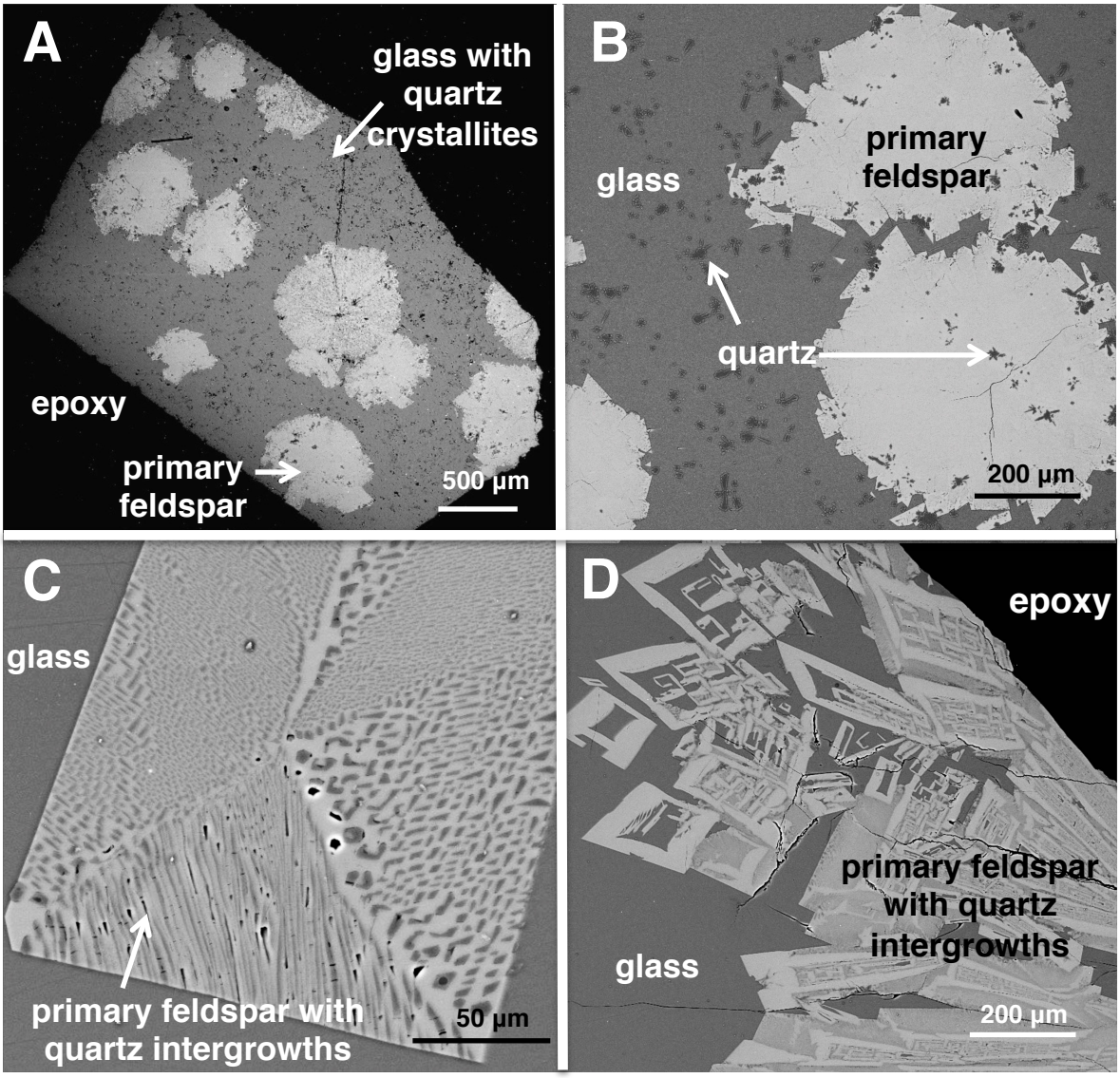

Figure 2.2: Backscatter electron images of quenched charges showing primary (Step 2) feldspars. **2.2A:** Glassy wafer retrieved from quenched run #G11, Table 2.3. Radiating large (up to 0.5 mm) alkali feldspars ("rosette" texture) set in matrix of glass and quartz crystallites (dark specks). **2.2B:** Magnification of a portion of 2.2A. Star-shaped β-quartz skeletal crystals are uniformly distributed in glass matrix and included in euhedral primary feldspars, showing that quartz was the first-nucleating phase from homogeneous melt. **2.2C:** Large euhedral sanidine crystal showing sector zoning of quartz intergrowths (darker stringers and blebs). Run #G63, Table 2.3. **2.2D:** Skeletal "hopper" crystals grown in Step 2 experiment (Run #G48, Table 2.3). Box-like crystals cored by glass (dark), feldspar-quartz intergrowths (mottled gray) and optically homogeneous persiliceous feldspars (uniform gray).

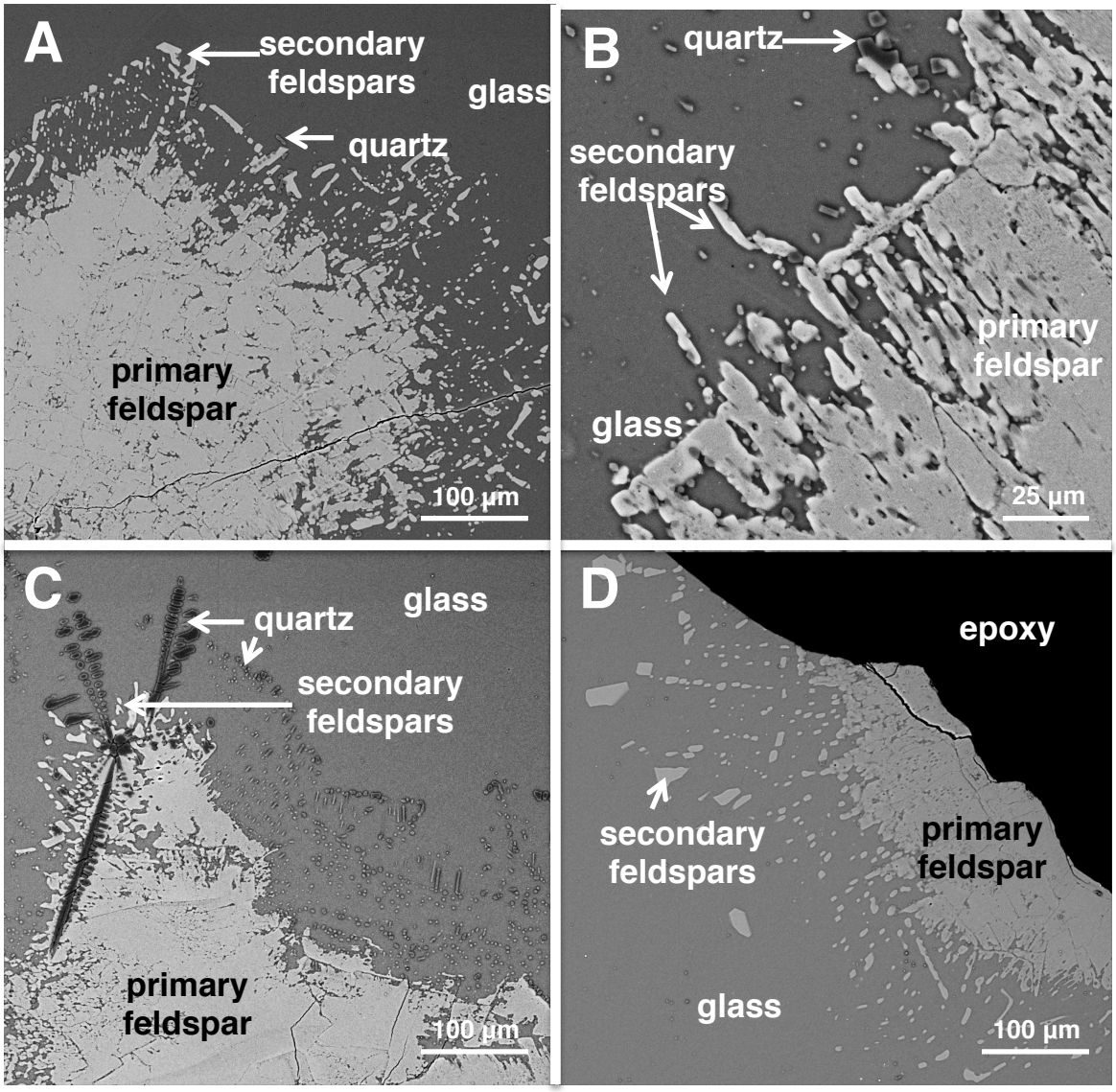

Figure 2.3: Backscatter electron images of secondary, or re-equilibrated (Step 3) feldspars. **2.3A:** Partially resorbed primary feldspar rosette. Original extent of rosette is outlined by new generation of small euhedral feldspars of normal composition (Si/Al = 3.0). Quartz is present among new feldspars. Run #G51, Table 2.3. **2.3B:** Secondary feldspars in resorbed rim of Step 2 rosette. Quartz has recrystallized to small (~10µm) equant grins. Residual primary feldspar is distinguished by composition. Run #G93, Table 2.3. **2.3C:** Secondary feldspars in partially resorbed margin of primary feldspar. Quartz (darker phase) has recrystallized to relatively large equant crystals and one very large propeller-shaped crystal where resorption has occurred. **2.3D:** Vestigial primary feldspar whose original outline is marked by a field of small secondary feldspars. Quartz is not visible but identified by X-ray diffraction. Run #G46, Table 2. 3.

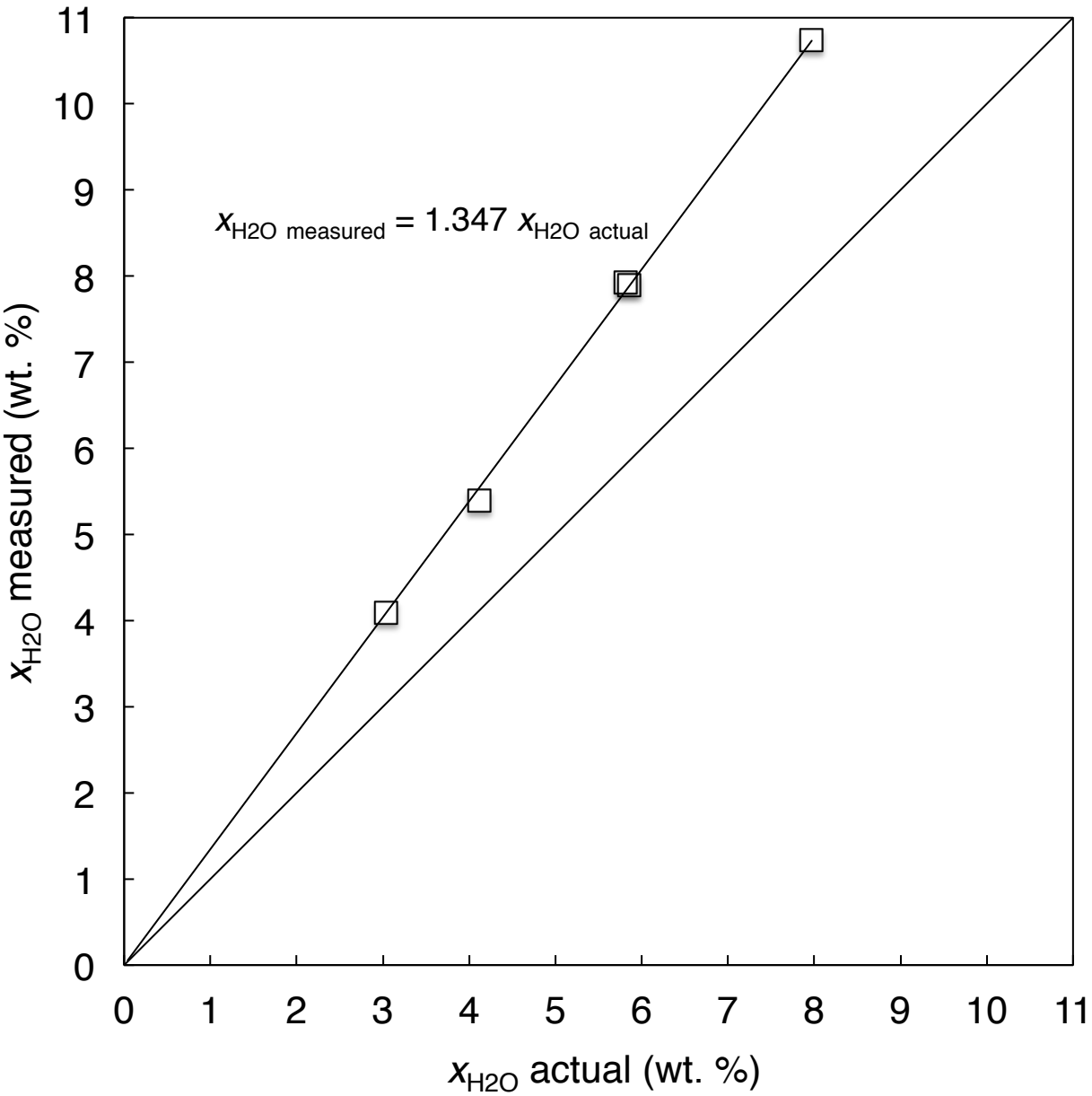

Figure 2.4: Electron microprobe totals plotted vs. H_2O content in the glass. All samples were entirely glass and were not vesiculated. The probe totals overestimate the amount of water contained in the glass by a regular amout according to the equation $x_{H2O\ measured} = 1.347\ x_{H2O}$.

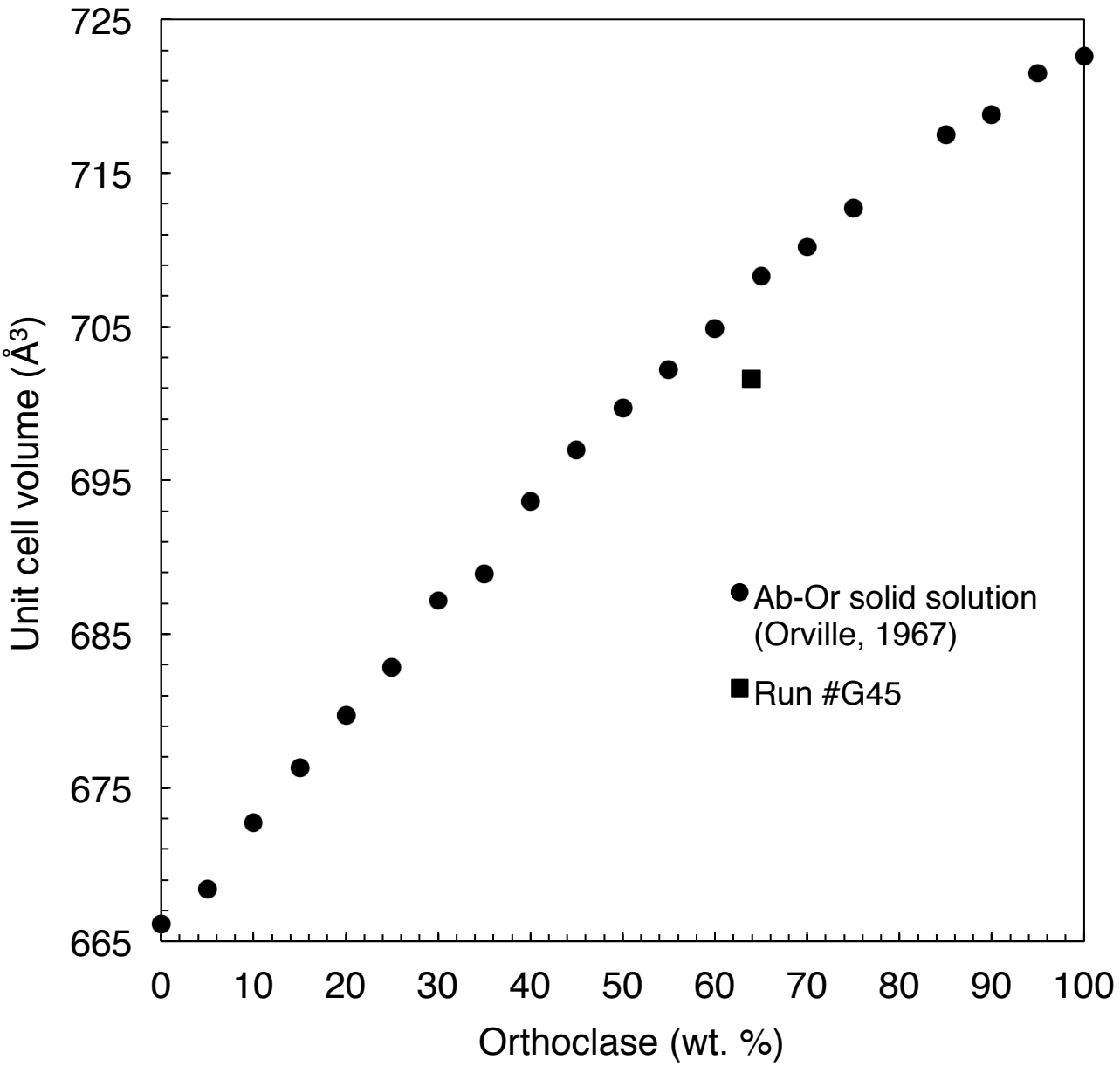

Figure 2.5: Unit cell volume of the feldspar crystallized in Run #G45 plotted on Orville's (1967) trend for the unit cell volumes of high albite-sanidine solid solutions. The unit cell contraction observed in this sample indicates that the primary feldspar crystallized here is a persiliceous, metastable solid solution of monoclinic feldspar with coesite. The error bars are smaller than the symbol size.

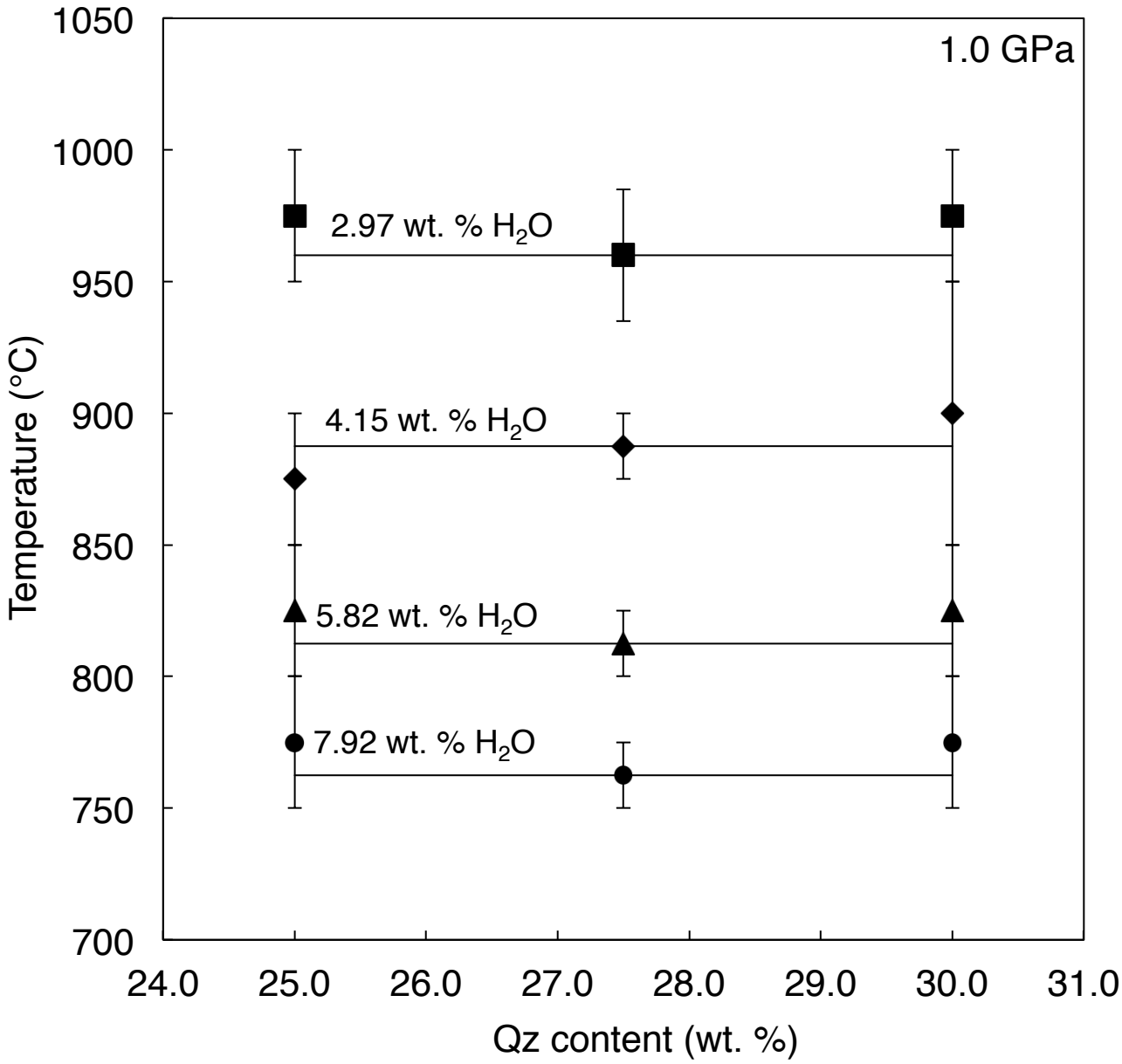

Figure 2.6: Haplogranite T-X_{Qz} binary at 1.0 GPa with H_2O isopleths plotted from determination made from the reversed equilibrium brackets. (Runs G14 and G88 may contain only feldspar as the crystalline phase, however quartz may be present. Further electron microprobe analysis would be required to make this determination.)

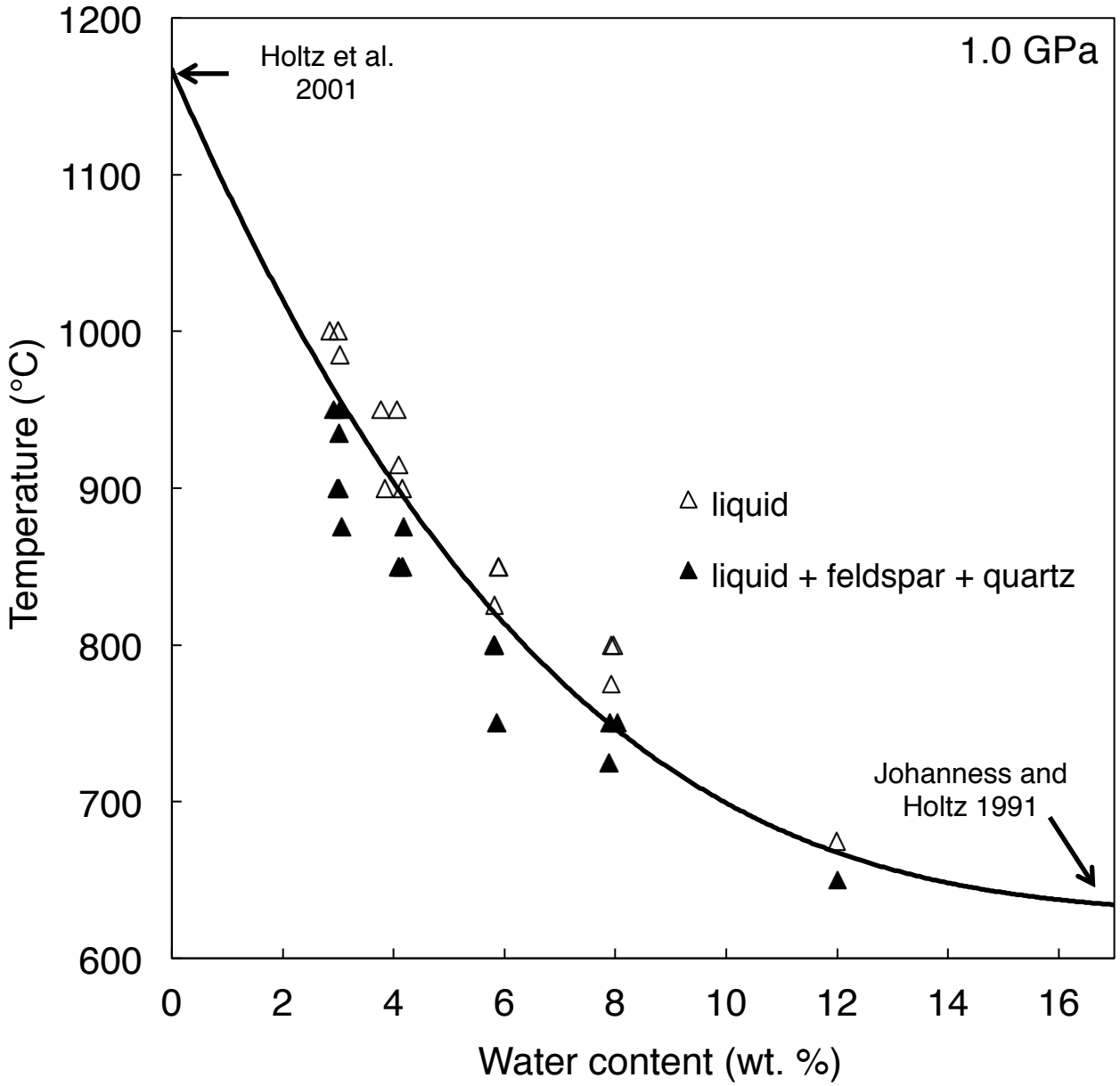

Figure 2.7: Haplogranite T-x_{H2O} binary at 1.0 GPa projected from x_{Qz} space showing the reversed equilibrium experiments that define the liquidus. The equation of the liquidus is for the dry bulk composition $Ab_{36.25}Or_{-36.25}Qz_{27.50}$. Note: Run G31 at 12 weight percent water plotting in the liquid field was not a reversal run.

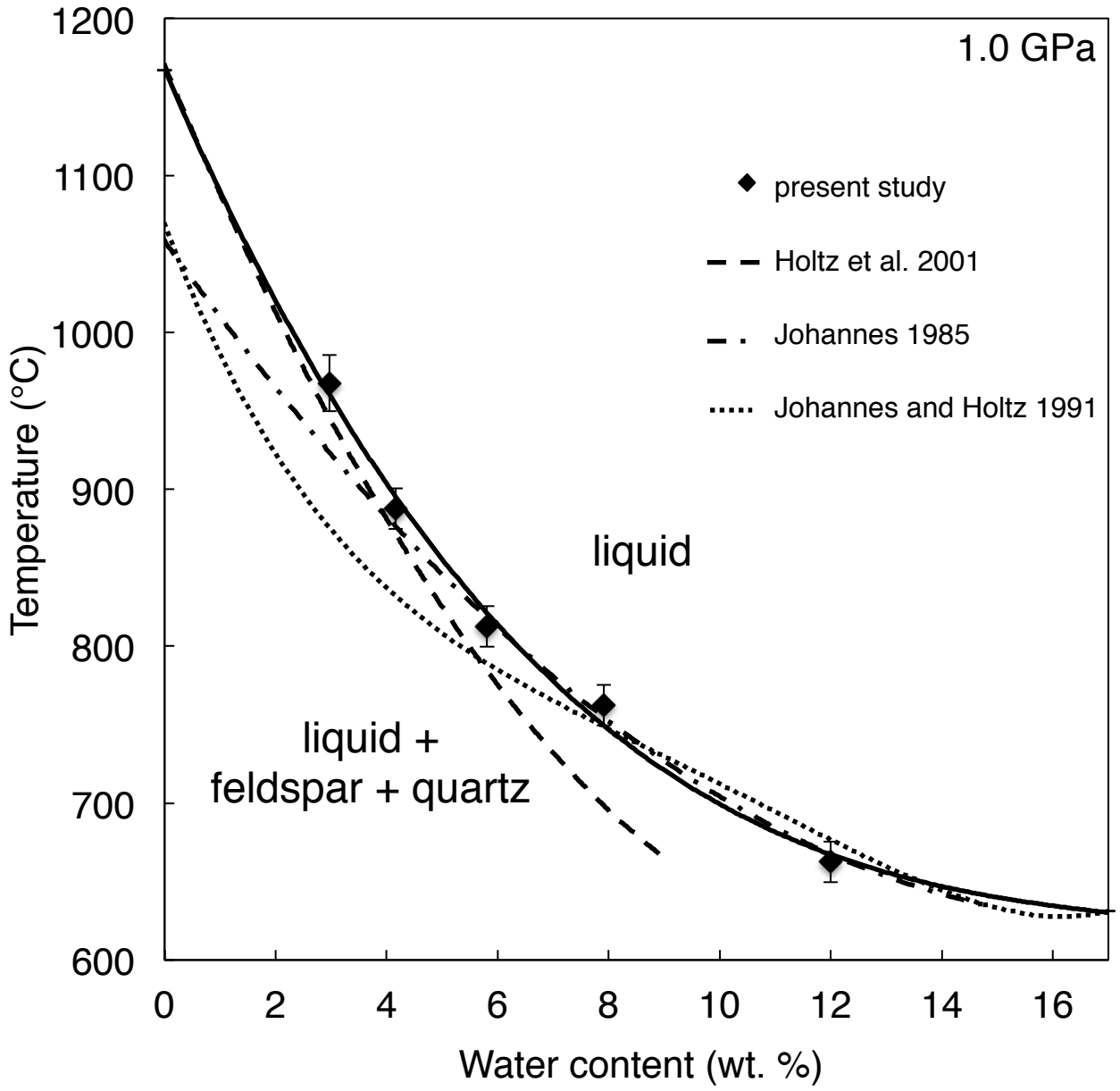

Figure 2.8: Haplogranite T-x_{H2O} binary at 1.0 GPa projected from x_{Qz} showing the liquidus determination from the present study plotted against previous estimates of other researchers. Our results plot on the high end of all the previous low pressure extrapolations.

Appendix: Full list of peaks from XRD conducted on sample #G45

(h,k,l)	Position (2θ)	Heigh (cts)	FWHM (2θ)	d-spacing (Å)	Rel. Int. (%)	phase
1 0 0	20.8656	1539.45	0.0976	4.25739	32.62	qz
2 0 -1	**21.4990**	**971.36**	**0.1115**	**4.13337**	**20.58**	**fls**
	22.1728	57.07	0.1673	4.00926	1.21	
1 1 1	**22.8491**	**892.82**	**0.0976**	**3.8921**	**18.92**	**fls**
1 3 0	**23.7153**	**2355.68**	**0.1533**	**3.75187**	**49.92**	**fls**
	24.7031	363.8	0.0836	3.60403	7.71	
1 1 -2	**25.8457**	**1134.47**	**0.0976**	**3.44724**	**24.04**	
1 0 1	26.6554	4061.21	0.1533	3.34434	86.06	qz
2 0 -2	**27.4618**	**4507.59**	**0.1394**	**3.24794**	**95.52**	**fls**
0 0 2	**27.7740**	**4559.54**	**0.1255**	**3.21214**	**96.62**	**fls**
1 1 1	28.3305	4311.39	0.1394	3.15029	91.36	fluorite
	29.0429	57.68	0.0836	3.07461	1.22	
1 3 1	**30.1053**	**1157.71**	**0.1533**	**2.96849**	**24.53**	**fls**
0 4 1	**30.8746**	**770**	**0.223**	**2.89626**	**16.32**	**fls**
	31.1070	366.69	0.1115	2.87515	7.77	
	32.4676	399.45	0.1394	2.7577	8.46	
2 4 -1	**35.1221**	**874.51**	**0.0836**	**2.55512**	**18.53**	**fls**
1 1 2	**35.5342**	**260.94**	**0.1673**	**2.52643**	**5.53**	**fls**
2 4 0	**36.5219**	**718.45**	**0.0976**	**2.46034**	**15.22**	**fls**
1 5 -1	**37.2927**	**288.15**	**0.1394**	**2.41124**	**6.11**	**fls**
	37.8546	35.51	0.0836	2.37674	0.75	
	38.3520	173.76	0.1255	2.34705	3.68	
	38.9608	111.94	0.1115	2.31176	2.37	
	39.5149	226.53	0.1673	2.28061	4.8	
	40.2791	190.32	0.1115	2.23909	4.03	
	41.2034	53.96	0.1673	2.19097	1.14	
0 6 0	**41.7406**	**941.17**	**0.1673**	**2.16401**	**19.94**	**fls**
	42.4274	327.69	0.223	2.13056	6.94	
	42.9408	131.14	0.17	2.10453	2.78	
	43.1576	59.04	0.204	2.09965	1.25	
	43.7973	50.23	0.102	2.06533	1.06	
	44.3413	118.36	0.102	2.04125	2.51	
	44.8674	50.18	0.136	2.01853	1.06	
	45.7977	182.12	0.17	1.97967	3.86	
	46.6369	304.37	0.102	1.94598	6.45	
2 2 0	47.0557	4718.93	0.136	1.92963	100	fluorite
	47.7244	57.54	0.204	1.90414	1.22	
	48.2592	171.52	0.136	1.88428	3.63	
	48.4832	160.74	0.136	1.8761	3.41	
	49.6061	201.08	0.306	1.83623	4.26	qz

1 1 2	50.1381	398.69	0.204	1.81799	8.45	
	51.0169	739.62	0.17	1.78871	15.67	
	51.9123	40.24	0.136	1.75995	0.85	
	52.4025	104.06	0.238	1.74463	2.21	
	52.9469	68.43	0.102	1.72797	1.45	
	53.2101	68.95	0.102	1.72004	1.46	
	53.5501	35.45	0.136	1.70992	0.75	
	54.8886	87.83	0.136	1.67134	1.86	
3 1 1	55.7959	1338.59	0.102	1.6463	28.37	fluorite
	56.6541	62.23	0.102	1.62338	1.32	
	57.2661	61.57	0.136	1.60748	1.3	
	58.0063	20.87	0.102	1.58871	0.44	
	58.5691	33.95	0.204	1.57478	0.72	
	59.2390	84.2	0.17	1.55856	1.78	

References

Aranovich, L. Y., Makhluf, A. R., Manning, C. E., and Newton, R. C. (2014). Dehydration melting and the relationship between granites and granulites. *Precambrian Research*, ***253***, 26-37.

Aranovich, L. Y., Newton, R. C., and Manning, C. E. (2013). Brine-assisted anatexis: experimental melting in the system haplogranite–H_2O–NaCl–KCl at deep-crustal conditions. *Earth and Planetary Science Letters*, ***374***, 111-120.

Baker, D. R., and Freda, C. (2001). Eutectic crystallization in the undercooled Orthoclase-Quartz-H_2O system experiments and simulations. *European Journal of Mineralogy*, ***13***(3), 453-466.

Boettcher, A. L., and Wyllie, P. J. (1968). Melting of granite with excess water to 30 kilobars pressure. *The Journal of Geology*, ***76***(2) *235*-244.

Brown, G. C., and Fyfe, W. S. (1970). The production of granitic melts during ultrametamorphism. *Contributions to Mineralogy and Petrology*, ***28***(4), 310-318.

Burnham, C. W., and Jahns, R. H. (1962). A method for determining the solubility of water in silicate melts. *American Journal of Science*, ***260***(10), 721-745.

Carman, J. H., and Tuttle, O. F. (1967). Experimental verification of solid solution of excess silica in sanidine from rhyolites. *Geological Society of America Special Paper* ***115,*** 33.

Collerson, K. B. and Fryer, B. J. (1978) The role of fluids in the formation and subsequent development of the continental crust. *Contributions to Mineralogy and Petrology* (**67**), 151-167.

Ebadi, A., and Johannes, W. (1991). Beginning of melting and composition of first melts in the system Qz-Ab-Or-H_2O-CO_2. *Contributions to Mineralogy and Petrology*, ***106***(3), 286-295.

Goranson, R. W. (1938). Silicate-water systems: phase equilibria in the $NaAlSi_3O_8$—H_2O and $KAlSi_3O_8$—H_20 systems at high temperatures and pressures. *American Journal of Science*, ***35***, 71-9l.

Grundy, H. D., and Ito, J. (1974). The refinement of the crystal structure of a synthetic non-stoichiometric Sr feldspar. *American Mineralogist,* ***59,*** 1319-1326.

Hayden, L. A., and Manning, C. E. (2011). Rutile solubility in $NaAlSi_3O_8$—H_2O fluids. *Chemical Geology*, ***284***(1), 74-81.

Holland, T. J. B., and Redfern, S. A. T. (1997). UNITCELL: a nonlinear least-squares program for cell-parameter refinement and implementing regression and deletion diagnostics. *Journal of Applied Crystallography*, ***30***(1), 84-84.

Holtz, F., Johannes, W., Tamic, N., and Behrens, H. (2001). Maximum and minimum water contents of granitic melts generated in the crust: a reevaluation and implications. *Lithos*, ***56***(1), 1-14.

Inger, S., and Harris, N. (1993). Geochemical constraints on leucogranite magmatism in the Langtang Valley, Nepal Himalaya. *Journal of Petrology*, ***34***(2), 345-368.

Jahns, R. H., and Burnham, C. W. (1969). Experimental studies of pegmatite genesis; l, A model for the derivation and crystallization of granitic pegmatites. *Economic Geology*, ***64***(8), 843-864.

Johannes, W. (1985). The significance of experimental studies for the formation of migmatites. In Ashworth, J. R. Ed.,Migmatites. New York: Springer, 36-85.

Johannes, W., and Holtz, F. (1991). Formation and ascent of granitic magmas. *Geologische Rundschau*, ***80***(2), 225-231.

Levien, L., and Prewitt, C. T. (1981). High-pressure crystal structure and compressibility of coesite. *American Mineralogist*, ***66***(3-4), 324-333.

Lipman, P., Dungan, M., & Bachmann, O. (1997). Comagmatic granophyric granite in the Fish Canyon Tuff, Colorado: implications for magma-chamber processes during a large ash-flow eruption. *Geology*, ***25***(10), 915-918.

Litvinovskii, B.A., Zanvilevich, A. N., and Wickham, S. M. (1994). Angara–Vitim batholith, Transbaikalia: structure, petrology, and petrogenesis. *Russian Geology and Geophysics*, ***35***(7-8), 190-203.

Litvinovsky, B.A., Podladchikov, Y.Y., 1993. Crustal anatexis during the influx of mantle volatiles. *Lithos* ***30***, 93–107.

Luth, W. C. (1976). Granitic rocks. In The evolution of the crystalline rocks (pp. 335-417). Academic Press London.

Luth, W. C., Jahns, R. H., and Tuttle, O. F. (1964). The granite system at pressures of 4 to 10 kilobars. *Journal of Geophysical Research*, ***69***(4), 759-773.

Martin, R. F. (2006) A-type granites of crustal origin ultimately result from open-system fennitization reactions in an extensional environment. *Lithos,* **91**, 125-136.

McLelland, J., Morrison, J., Selleck, B., Cunningham, B., Olson, C., and Schmidt, K. (2002). Hydrothermal alteration of late‐to post tectonic Lyon Mountain Granitic Gneiss, Adirondack Mountains, New York: Origin of quartz–sillimanite segregations, quartz–albite lithologies, and associated Kiruna‐type low‐Ti Fe‐oxide deposits. *Journal of Metamorphic Geology*, ***20***(1), 175-190.

McMurdie, H. F., Morris, M. C., Evans, E. H., Paretzkin, B., de Groot, J. H., Hubbard, C. R., and Carmel, S. J. (1985). Standard X-ray diffraction powder patterns. *U.S. Bureau of Standards Monograph **25-12**,* 1-96.

Megaw, H. D. (1970). Structural relationship between coesite and feldspar. *Acta Crystallographica Section B: Structural Crystallography and Crystal Chemistry*, ***26***(3), 261-265.

Nabelek, P. I., and Bartlett, C. D. (1998). Petrologic and geochemical links between the post-collisional Proterozoic Harney Peak leucogranite, South Dakota, USA, and its source rocks. *Lithos*, ***45*****(**1), 71-85.

Nabelek, P. I., Whittington, A. G., and Sirbescu, M. L. C. (2010). The role of H_2O in rapid emplacement and crystallization of granite pegmatites: resolving the paradox of large crystals in highly undercooled melts. *Contributions to Mineralogy and Petrology*, ***160***(3), 313-325.

Orville, P. M. (1967). Unit-cell paramets of microcline-low albite and sanidine-high albite solid solution series. *American Mineralogist*, ***52*****(**1-2), 55.

Osinski, G. R. (2004). Impact melt rocks from the Ries structure, Germany: an origin as impact melt flows?. *Earth and Planetary Science Letters*, ***226***(3), 529-543.

Perry, K. Jr. (1968) Representation of mineral chemical analyses in 11 dimensional space. Part I. Feldspars. *Lithos, **1***, 201-218.

Parsons, I. (1978). Alkali-feldspars: which solvus?. *Physics and Chemistry of Minerals*, ***2***(3), 199-213.

Rutter, M. J., and Wyllie, P. J. (1988). Melting of vapour-absent tonalite at 10 kbar to simulate dehydration–melting in the deep crust. *Nature*, ***331***(6152), 159-160.

Seck, H. A. (1971). Effect of pressure on composition of coexisting alkali feldspars and plagioclases in system $NaAlSi_3O_8$— $KAlSi_3O_8$— $CaAl_2Si_2O_8$ — H_2O. *Contributions to Mineralogy and Petrology*, ***31***(1), 67.

Stevens, G., and Clemens, J. D. (1993). Fluid-absent melting and the roles of fluids in the lithosphere: a slanted summary?. *Chemical Geology*, ***108*****(**1), 1-17.

Sturt, B. A. (1970) Exsolution phenomena in metamorphic minerals developed during aging with particular reference to feldspar solid solutions. *Mineralogical Magazine, **37,*** 815-832.

Tuttle, O. F., and Bowen, N. L. (1958). Origin of granite in the light of experimental studies in the system $NaAlSi_3O_8$–$KAlSi_3O_8$–SiO_2–H_2O. *Geological Society of America Memoirs*, ***74***, 1-146.

Vielzeuf, D., and Holloway, J. R. (1988). Experimental determination of the fluid-absent melting relations in the pelitic system. *Contributions to Mineralogy and Petrology*, ***98***(3), 257-276.

Wickham, S. M., and Taylor Jr, H. P. (1987). Stable isotope constraints on the origin and depth of penetration of hydrothermal fluids associated with Hercynian regional metamorphism and crustal anatexis in the Pyrenees. *Contributions to Mineralogy and Petrology*, ***95***(3), 255-268.

Weinberg, R. F., and Hasalová, P. (2015). Water-fluxed melting of the continental crust: A review. *Lithos*, ***212***, 158-188.

Webster, J. D. (1997). Exsolution of magmatic volatile phases from Cl-enriched mineralizing granitic magmas and implications for ore metal transport. *Geochimica et Cosmochimica Acta*, ***61***(5), 1017-1029.

Wright, T. L., and Stewart, D. B. (1968). X-ray and optical study of alkali feldspar. I. Determination of composition and structural state from refined unit-cell parameters and 2V. *American Mineralogist*, ***53***(1-2), 38.

Yang, J., Godard, G., and Smith, D. C. (1998). K-feldspar-bearing coesite pseudomorphs in an eclogite from Lanshantou (Eastern China). *European Journal of Mineralogy*, ***10***(5) 969-986.